The Influence of Ocean-Surface-Velocity-Dependent Wind Stress on the Dynamics of the Southern Ocean: The Near-Inertial and the Sub-Inertial Response

Dissertation zur Erlangung des Doktorgrades der
Mathematisch-Naturwissenschaftlichen Fakultät der
Christian-Albrechts-Universität zu Kiel

Vorgelegt von
Willi Rath

1. Gutachter: Prof. Dr. Richard J. Greatbatch
2. Gutachter: Prof. Dr. Peter Brandt

Datum der mündlichen Prüfung: 11. Dezember 2013

Kiel, 11. Dezember 2013

Contents

Abstract

This thesis examines the consequences of the ocean-surface-velocity dependence of the wind stress (SVD) for the dynamics of the Southern Ocean. It does so by comparing the output from eddying ocean-model experiments that only differ in the way the wind stress is parameterized. The thesis consists of three separate research papers.

The first paper assesses the influence of SVD on the near-inertial variability. It is shown that SVD leads to a substantial reduction of horizontally averaged near-inertial energy (NIE) and of horizontally averaged wind power input (WPI) into the near-inertial frequency band. The observed reduction of NIE and near-inertial WPI is explained by the fact that SVD, to leading order, adds a linear damping term to the momentum equation governing near-inertial oscillations in the mixed-layer. This damping term is inversely proportional to the mixed-layer depth and hence the effect of SVD on near-inertial oscillations is found to be largest if the mixed-layer is shallow.

The second paper assesses the influence of SVD on sub-inertial time scales. It is found that SVD also substantially reduces sub-inertial WPI and mesoscale eddy kinetic energy (EKE). The largest effect of SVD on sub-inertial WPI and EKE is found along the path of the Antarctic Circumpolar Current (ACC). SVD is found to generally damp the amplitude of monthly to inter-annual variability in the model, without affecting the time-dependence of the wind stress, of WPI, and of the strength of the ACC. SVD is, however, found to have only a minor impact on the path and strength of the ACC.

The third paper connects to the first one by focussing on the spatial and temporal distribution of NIE and near-inertial WPI in the Southern Ocean. The modelled near-inertial WPI is found to be mainly governed by the variability of the wind-stress at the local inertial frequency (IWSV). This relationship is used to indirectly examine the temporal evolution of near-inertial WPI on time scales much longer than those which can be directly examined with the model. It is found that from 1979 to 2011 IWSV over the Southern Ocean has increased substantially. Furthermore, the inter-annual variability of IWSV in the Southern Ocean is shown to be largely governed by the Southern Annular Mode.

Zusammenfassung

Die vorliegende Arbeit untersucht die Auswirkung einer Windstress-Parameterisierung, die von der Oberflächengeschwindigkeit des Ozeans abhängt (SVD), auf die Dynamik des Südlichen Ozeans. Dazu wird die Ausgabe von Ozeanmodellexperimenten verglichen, die sich nur in der Art der Windstress-Parameterisierung unterscheiden. Die Arbeit besteht aus drei separaten Forschungsartikeln.

Der erste Artikel untersucht den Einfluss der SVD auf die zeitliche Veränderlichkeit bei Frequenzen nahe der Coriolis-Frequenz. Es wird gezeigt, dass die SVD zu einer deutlichen Verringerung der horizontal gemittelten kinetischen Energie von Inertialschwingungen (NIE) und der horizontalen Windarbeit (WPI) in das entsprechende Frequenzband führt. Diese Verringerung wird dadurch erklärt, dass die SVD in führender Ordnung einen linearen Dämpfungsterm zur Impulsgleichung der Inertialschwingungen hinzufügt. Dieser Dämpfungsterm ist umgekehrt proportional zur Tiefe der Deckschicht. Daher sind die Auswirkungen der SVD dort besonders groß, wo die Deckschicht flach ist.

Der zweite Artikel befasst sich mit dem Einfluss der SVD auf Zeitskalen länger als die durch die Coriolis-Frequenz Bestimmten. Es wird gezeigt, dass die SVD auch auf diesen Zeitskalen die WPI und die kinetische Wirbelenergie (EKE) verringert. Der größte Effekt der SVD findet sich entlang des Pfades des Antarktischen Zirkumpolarstromes (ACC). SVD dämpft die Amplitude der zeitlichen Veränderlichkeit im Modell auf monatlichen und auf zwischenjährlichen Zeitskalen ohne jedoch die normierte Zeitabhängigkeit des Windstress, der WPI und der Stärke des ACC zu beeinflussen. Desweiteren ist der Einfluss der SVD auf den Pfad und die Stärke des ACC nur sehr gering.

Der dritte Artikel schließt sich thematisch an den Ersten an und konzentriert sich auf die räumliche und zeitliche Verteilung der NIE und der nah-inertialen WPI im Südlichen Ozean. Die nah-inertiale WPI im Modell ist vorrangig durch die Veränderlichkeit des Windstress nahe der Coriolis-Frequenz (IWSV) bestimmt. Diese Beziehung wird ausgenutzt, um indirekt auch die zeitliche Entwicklung der nah-inertialen WPI auf Zeitskalen zu untersuchen, die viel länger sind, als die mit dem Ozeanmodell behandelbaren Zeiträume. Es wird gezeigt, dass sich die IWSV im Südlichen Ozean von 1979 bis 2011 deutlich erhöht hat. Desweiteren wird gezeigt, dass die zwischenjährlichen Schwankungen der IWSV zum großen Teil durch die Southern Annular Mode bestimmt sind.

Chapter 1

Introduction

1.1 Motivation

As the typical wind velocity is bigger than the typical ocean-surface velocity by one or two orders of magnitude, the contribution of the latter to the wind stress is often neglected, and the wind stress is calculated from the 10-m-wind vector, $\vec{U}_{wind}$, alone:

$$\vec{\tau}_{ctrl} = \rho_a c_d(|\vec{U}_{wind}|) \cdot |\vec{U}_{wind}| \cdot \vec{U}_{wind} \tag{1.1}$$

Here, ρ_a denotes the density of air close to the sea-surface and $c_d(U)$ denotes the drag coefficient. Alternatively, the wind stress can be parameterized in an ocean-surface-velocity-dependent (SVD) way, by substituting the difference between the wind and the ocean-surface velocity, $\vec{u}_{ocean}$, for the wind vector:

$$\vec{\tau}_{svd} = \rho_a c_d(|\vec{U}_{wind} - \vec{u}_{ocean}|) \cdot |\vec{U}_{wind} - \vec{u}_{ocean}| \cdot (\vec{U}_{wind} - \vec{u}_{ocean}) \tag{1.2}$$

It is known that SVD generally damps the ocean currents in models (*Dewar and Flierl*, 1987), improves the representation of the tropical sea-surface temperature (SST) modelled by regional ocean models (*Pacanowski*, 1987) and by coupled climate models (*Luo et al.*, 2005), reduces estimates of wind-power input (WPI) into the general circulation of the ocean (*Duhaut and Straub*, 2006; *Hughes and Wilson*, 2008; *Xu and Scott*, 2008; *Scott and Xu*,

2009), and acts to damp the mesoscale eddy-kinetic energy (EKE) in a realistic ocean model of the North Atlantic (*Zhai and Greatbatch*, 2007). The Southern-Ocean response to SVD is, however, largely unstudied.

In addition to the direct examination of the consequences of SVD, this work highlights near-inertial oscillations. Near-inertial oscillations are ubiquitous in the ocean (*van Meurs*, 1998). They are usually accelerated by changes of the wind-stress vector on time scales similar to the local Coriolis parameter (*Pollard and Millard*, 1970; *Gill*, 1982). Besides being a potential source for the mixing that drives the meridional overturning circulation (*Munk and Wunsch*, 1998), near-inertial oscillations have been shown to play a role in setting the surface-mixed-layer depth (*Pollard et al.*, 1972) and to influence the tropical sea-surface temperature, which in turn influences the global climate by teleconnections (*Jochum et al.*, 2013). Locally, there are observational studies contributing to the understanding of near-inertial oscillations (*Pollard and Millard*, 1970; *D'Asaro*, 1985; *Plueddemann and Farrar*, 2006). On a global scale, however, there are only loose observational constraints to near-inertial WPI and near-inertial energy (NIE), which are based on surface-drifter data (*Elipot and Lumpkin*, 2008; *Chaigneau et al.*, 2008). Hence, to a large part, the current understanding of the large-scale distribution of near-inertial WPI and NIE is based on modelling studies (*Watanabe and Hibiya*, 2002; *Alford*, 2003).

The primary objective of this thesis is to understand the response of the Southern Ocean to SVD. It highlights the SVD-response of the Southern-Ocean wind stress and WPI, of NIE and EKE, and of the strength and the path of the ACC. Furthermore, this thesis seeks to extend the understanding of near-inertial oscillations in the Southern Ocean.

1.2 Structure of the thesis

This thesis consists of three separate manuscripts. The first two manuscripts (presented in Chapters 2 and 3) directly address the oceanic response to SVD. The third manuscript (presented in Chapter 4) highlights the spatial and temporal distribution of near-inertial energy (NIE) and near-inertial WPI.

Reduction of Near-Inertial Energy Through the Dependence of Wind Stress on the Ocean-Surface Velocity: The first manuscript, which constitutes Chapter 2 of this thesis, studies the influence of SVD on the oceanic variability at near-inertial frequencies. It is found that SVD substantially reduces near-inertial WPI and NIE as modelled by a regional primitive-equation model. The reduction is large where the mixed layer is shallow. A mechanism for the reduction of near-inertial WPI and NIE is proposed and tested using an idealized model and the primitive-equation model.

Sub-Inertial Response to Ocean-Surface-Velocity Dependence of the Wind Stress in a Model of the Southern Ocean: The second manuscript, which constitutes Chapter 3 of this thesis, examines the sub-inertial response to SVD. SVD substantially reduces sub-inertial WPI and mesoscale EKE, while leaving the eastward transport associated with the Antarctic Circumpolar Current (ACC) largely unaffected. Furthermore, while SVD damps the amplitudes of the modelled annual-mean wind-stress, WPI, EKE, and transport through Drake Passage, it does not affect the time-dependence of the wind-stress, WPI and transport through Drake Passage.

On the Spatial and Temporal Distribution of Near-Inertial Energy in the Southern Ocean: The third manuscript, which constitutes Chapter 4 of this thesis, uses the model experiments detailed in Chapter 2 to assess the spatial and temporal distribution of NIE and near-inertial WPI in the Southern Ocean. The modelled near-inertial WPI is found to be largely determined by the inertial wind-stress variance (IWSV). This close relationship between near-inertial WPI and IWSV is exploited to indirectly assess inter-annual and decadal variability of near-inertial WPI. IWSV is following an upward trend from 1979 to 2011. The inter-annual variability of IWSV in the South Pacific is shown to be closely related to the Southern Annular Mode (SAM).

Chapter 2

Reduction of Near-Inertial Energy Through the Dependence of Wind Stress on the Ocean-Surface Velocity

Willi Rath, Richard J. Greatbatch, Xiaoming Zhai[1]

Abstract: A realistic primitive-equation model of the Southern Ocean at eddying spatial resolution is used to examine the effect of ocean-surface-velocity dependence of the wind stress on the strength of near-inertial oscillations. Accounting for the ocean-surface-velocity dependence of the wind stress leads to a large reduction of wind-induced near-inertial energy of approximately 40 percent and of wind power input into the near-inertial frequency band of approximately 20 percent. A large part of this reduction can be explained by the leading-order modification to the wind stress if the ocean-surface velocity is included. The strength of the reduction is shown to be modulated by the inverse of the ocean-surface-mixed-layer depth. We

[1]This chapter has been published: Rath, W., R. J. Greatbatch, and X. Zhai (2013a), Reduction of Near-Inertial Energy Through the Dependence of Wind Stress on the Ocean-Surface Velocity, *Journal of Geophysical Research - Oceans*, *118*(6), 2761–2773, doi: 10.1002/jgrc.20198

conclude that the effect of surface-velocity dependence of the wind stress should be taken into account when estimating the wind-power input into the near-inertial frequency band and when estimating near-inertial energy levels in the ocean due to wind forcing.

2.1 Introduction

Near-inertial oscillations (NIO) dominate the internal-wave spectrum of the ocean (see *Kunze* (1985)). They are thought to be a source for the energy that drives the meridional-overturning circulation (see *Munk and Wunsch* (1998)) and play a role in setting the surface-mixed-layer depth (see *Pollard et al.* (1972)) and thereby influence the sea-surface temperature (SST) with potentially important implications for climate (*Jochum et al.* (2013)). In the surface-mixed layer, NIOs are quasi-free horizontal motions that are typically generated by fast changes of the wind stress vector (*Pollard and Millard* (1970); *Gill* (1982)). Once excited, NIOs are subject to deflection by the Coriolis force, dissipation (including the loss of kinetic energy to potential energy through entrainment of water into the mixed layer), stresses at the base of the mixed layer due the ambient flow field and propagation of near-inertial waves (NIW) out of the mixed layer (see, for example, *Gill* (1982), *Gill* (1984), *Plueddemann and Farrar* (2006), *Furuichi et al.* (2008), and *Zhai et al.* (2009)).

Our knowledge of wind power input (WPI) into the near-inertial frequency band, and also near-inertial energy (NIE) levels in the ocean, is only loosely constrained by observations. There are observational studies which have contributed to our understanding of the physics of NIOs by analyzing local observational data mainly from moorings (see *Pollard and Millard* (1970), *D'Asaro* (1985) and *Plueddemann and Farrar* (2006)), but it is only recently that the first direct estimates of global scale NIE have been obtained based on surface-drifter data (see *Elipot and Lumpkin* (2008) and *Chaigneau et al.* (2008)). In the meantime, the simple slab-ocean model proposed by *Pollard and Millard* (1970), described in detail in Section 2.2.3, has been used to assess NIE and near-inertial WPI on a global scale (see *Watanabe and*

Hibiya (2002), *Alford* (2003)). Moreover, it can be expected that numerical models will continue to be widely used in the future for assessing NIE and near-inertial WPI.

This study aims at understanding how including the ocean-surface velocity into the parameterization of the wind stress (called surface-velocity dependence, or SVD, hereafter) influences the levels of NIE in the surface-mixed layer and the near-inertial WPI. SVD is known to lead to a general damping of the ocean currents (see *Dewar and Flierl* (1987)) which can improve the modelled SST in climate models (see *Pacanowski* (1987) and *Luo et al.* (2005)). SVD has been shown to reduce WPI into geostrophic motions by up to 30% (see *Duhaut and Straub* (2006) and *Hughes and Wilson* (2008)) and mesoscale eddy kinetic energy (EKE) in a regional ocean model by about 10% (see *Zhai and Greatbatch* (2007)). The large effect of SVD on WPI into the large-scale circulation of the ocean suggests that SVD can also have a significant effect on NIE and WPI into the inertial frequency band.

As the main model to assess the relevance of SVD for NIOs, we use a realistic primitive-equation model at eddying resolution (SPFLAME). We find that SVD reduces temporally and horizontally averaged near-inertial WPI by as much as 34.5 % and temporally and horizontally averaged NIE by as much as 43.1 % in summer. Averaged over a whole year, horizontally averaged near-inertial WPI is reduced by 22.1 %, and horizontally averaged NIE is reduced by 39.9 % (see Table 2.1). We argue that a large part of the reduction can be explained by the leading-order correction to WPI induced by SVD. To illustrate the mechanism, we use the linear slab-ocean model of *Pollard and Millard* (1970) (hereafter PM70). In PM70, SVD corresponds, to leading order, to adding a linear damping term to the momentum equation. The magnitude of the extra damping term is found to be set by the wind speed and the inverse of the mixed-layer depth.

In Section 2.2, we discuss the wind-stress parameterizations, and the models and experiments used in this study. In Section 2.3, we briefly describe the spatial and temporal distribution of NIE and near-inertial WPI in the primitive-equation model. Section 2.4 covers the main results of this study. First, we describe the large reduction of NIE and near-inertial WPI found

	Jan. 2001	whole 2001
NIE, CONTROL-GCM	$119.9\,\mathrm{Jm}^{-2}$	$135.8\,\mathrm{Jm}^{-2}$
NIE, SVD-GCM	$68.2\,\mathrm{Jm}^{-2}$	$82.9\,\mathrm{Jm}^{-2}$
R_{NIE}	$-43.1\,\%$	$-39.9\,\%$
WPI, CONTROL-GCM	$0.055\,\mathrm{TW}$	$0.068\,\mathrm{TW}$
WPI, SVD-GCM	$0.036\,\mathrm{TW}$	$0.053\,\mathrm{TW}$
R_{WPI}	$-34.5\,\%$	$-22.1\,\%$

Table 2.1: *Temporally and horizontally averaged mixed-layer NIE and temporally averaged and horizontally integrated near-inertial WPI for the whole model domain together with the relative differences for the experiments CONTROL-GCM and SVD-GCM.*

in the primitive-equation-model experiments when including SVD. We then propose a simple mechanism that explains the observed reduction and show results from the slab-ocean model to confirm that a large reduction of NIE can be explained by the direct effect of the changed wind-stress parameterization. Finally, we show that the reduction of NIE and near-inertial WPI closely follow the annual cycle of the mixed-layer depth. Section 2.5 concludes with a summary. In the appendices, we briefly discuss the definition used for the mixed-layer depth, the time-filtering used to extract the near-inertial signal from the model output and the tuning of the slab-ocean model.

2.2 Methods, Models and Experiments

2.2.1 The Wind-Stress Parameterization

Conventionally, the wind stress is parameterized in terms of 10-m-wind speed, $\vec{U}_{10}$, alone. In terms of density of air close to the sea surface, ρ_a, and the drag coefficient, c_d, the wind stress is then defined as

$$\vec{\tau}_{CTL} \equiv \rho_a c_d(|\vec{U}_{10}|)|\vec{U}_{10}|\vec{U}_{10} \tag{2.1}$$

We chose to parameterize the drag coefficient according to *Large and Pond* (1981) with a leveling off for high wind speeds according to *Donelan et al.* (2004). With the above parameterization of the wind stress, wind power

input WPI is proportional to the projection of the wind-stress vector onto the ocean-surface-velocity vector $\vec{u}_o$

$$WPI_{CTL} \equiv \tau_{CTL} \cdot \vec{u}_o = \rho_a c_d(|\vec{U}_{10}|)|\vec{U}_{10}|\vec{U}_{10} \cdot \vec{u}_o \tag{2.2}$$

Alternatively, the wind stress can be parameterized in terms of the relative velocity of the wind and the ocean $\vec{U}_{10} - \vec{u}_o$

$$\vec{\tau}_{SVD} \equiv \rho_a c_d(|\vec{U}_{10} - \vec{u}_o|)|\vec{U}_{10} - \vec{u}_o|(\vec{U}_{10} - \vec{u}_o) \tag{2.3}$$

Duhaut and Straub (2006) show that the leading-order effect of changing the wind stress to $\vec{\tau}_{SVD}$ is

$$\Delta WPI \equiv WPI_{SVD} - WPI_{CTL} \approx -\rho_a c_d|\vec{U}_{10}|[|\vec{u}_o|^2 + (\vec{u}_o \cdot \hat{\vec{U}}_{10})^2] \tag{2.4}$$

where $\hat{\vec{U}}_{10}$ is the unit vector pointing in the direction of the 10-m-wind vector $\vec{U}_{10}$. Since both $|\vec{u}_o|^2$ and $(\vec{u}_o \cdot \hat{\vec{U}}_{10})^2$ are positive definite, the effect of SVD is a general reduction of WPI. This negative definite ΔWPI has been shown to provide a sink term for mesoscale EKE by *Zhai and Greatbatch* (2007).

2.2.2 A Realistic Primitive-Equation Model – SPFLAME

We use an eddying $(1/10)^\circ$ primitive-equation ocean model with realistic topography, as described by *Eden* (2006). It covers the Southern Ocean between $78^\circ S$ and $30^\circ S$. In the vertical, the domain is separated into 42 levels with increasing thickness ranging from $10\,m$ at the surface to $250\,m$ at $5500\,m$ depth. The model is driven by six-hourly $10\,m$-winds from the ERA40 reanalysis (*Uppala et al.* (2005)) and by climatological surface-heat fluxes (see *Barnier et al.* (1995)). Surface salinity is restored to climatological values taken from *Levitus et al.* (1994) with a time scale of $15\,days$ for the upper level of thickness $10\,m$. The surface-momentum flux is derived from 10m-winds using the two different wind-stress parameterizations given by (2.1) and (2.3) above. Vertical mixing is parameterized using the TKE-

mixing scheme as described by *Gaspar et al.* (1990) and *Blanke and Delecluse* (1993), and horizontal mixing is parameterized in both the momentum and tracer equation as a biharmonic diffusivity. At $30°S$, an open boundary is used where barotropic in- and outflow are prescribed and where potential temperature and salinity are restored to climatological values.

The model has realistic levels of mesoscale EKE (see *Eden* (2006) for a comparison with an observational estimate of the EKE based on satellite altimetry). The modelled depth-integrated transport through Drake Passage of about 120 Sv is within the error bar of the estimate (134 ± 27) Sv given by *Cunningham et al.* (2003).

The model is spun up from rest (SPINUP-GCM) using the climatology of *Levitus et al.* (1994) (for salinity) and *Levitus and Boyer* (1994) (for potential temperature) as the initial condition and using the conventional parameterization of the wind stress (see equation (2.1)) for 31 years. The years 1 to 10 of the spin-up phase are forced by climatological wind stress, and the years 11 to 31 are forced by conventional wind stress, given by (2.1), for the years 1980 to 2000 of 6-hourly 10-m-wind fields from the ERA40 reanalysis. Then, the experiment is forked into two runs, one of which continues to be forced by conventional wind stress (equation (2.1)), and one of which is forced by surface-velocity-dependent wind stress (equation (2.3)). We name these two runs CONTROL-GCM and SVD-GCM respectively. Note that we start the analysis of the two model runs immediately after the forking and that, consequently, the adjustment of the run SVD-GCM to the new wind-stress parameterization is contained in the data we analyze. The mesoscale-eddy field is important in modulating the small-scale structure of the spatial distribution of NIE by locally changing the effective Coriolis parameter (see *Zhai et al.* (2005), *Zhai et al.* (2007)). Adjustment of the run SVD-GCM to the new wind stress parameterization involves the model switching into a different realization of the (chaotic) mesoscale-eddy field. To be sure to capture the direct effect of the changed wind stress parameterization rather than a secondary effect due to a changed mesoscale, we decided to accept the disadvantage of a run that is subject to adjustment. We discuss the implications of the adjustment process for our results in Section 2.4, where we

also note that NIE itself goes through an adjustment process to the change in the wind-stress parameterization.

The first 36.5 days of the output from the runs CONTROL-GCM and SVD-GCM are available at a high spatial resolution ($1/10^\circ \times 1/10^\circ$) and at a high temporal resolution (3 hours). For the rest of the runs CONTROL-GCM and SVD-GCM, covering the year 2001, we reduced the spatial resolution of the model output to $1^\circ \times 1^\circ$ without changing the temporal resolution. By comparing the full-resolution output for the first 36.5 days to the reduced-resolution output over the same period, we found that NIE at the reduced-resolution contains all the information that is relevant for this study, and hence decided to use the $1^\circ \times 1^\circ$ resolution output throughout.

To calculate NIE, we filtered the velocity field to near-inertial frequencies by using a fifth-order Butterworth filter as described in Appendix 2.B. Throughout the manuscript, the subscript I indicates near-inertially filtered quantities.

2.2.3 A Linear Slab-Ocean Model – PM70

Pollard and Millard (1970) proposed a local linear slab-ocean model for near-inertial oscillations (PM70) which has since been widely used to assess the input of near-inertial energy into the surface-mixed layer of the ocean (*Alford* (2003)). It is a local model for the near-inertial velocity in the mixed layer (u, v) featuring the Coriolis force $f(-v, u)$, the wind stress $\vec{\tau} = (\tau^x, \tau^y)$, a linear damping term with the coefficient ϵ, the mixed-layer depth H (assumed to be time-independent), and the reference density ρ_0:

$$u_t - fv = \frac{\tau^x}{\rho_0 H} - \epsilon u \tag{2.5}$$

$$v_t + fu = \frac{\tau^y}{\rho_0 H} - \epsilon v \tag{2.6}$$

The time-evolution of kinetic energy, $E = \vec{u} \cdot \vec{u}/2$, in PM70 is governed by

$$E_t = uu_t + vv_t = \frac{1}{\rho_0 H}(\tau^x u + \tau^y v) - \epsilon(u^2 + v^2) \tag{2.7}$$

To numerically integrate the slab model, we chose to discretize the Coriolis term with centered differences, and the explicit linear damping, as well as the wind-stress term using a backward scheme. For the surface-velocity-dependent case, the wind-forcing term includes a damping component that can become unstable if it is discretized with centered differences.

The model is started from rest. We prescribe a spatially varying mixed-layer depth that has been diagnosed from the initial 36.5 days of the experiment CONTROL-GCM as described in Appendix 2.A, and use the same 6-hourly-wind fields used to drive the primitive-equation model in the initial 36.5 days of the experiments CONTROL-GCM and SVD-GCM. We call the experiments CONTROL-SLAB (with conventional wind stress) and SVD-SLAB (with surface-velocity-dependent wind stress). The only free parameter of the model is then the explicit linear-damping time scale $1/\epsilon$ which we set to 4.5 days for both the experiments CONTROL-SLAB and SVD-SLAB. For details on the tuning of ϵ, we refer to Appendix 2.C. The velocity fields from the PM70 experiments are filtered using the same filter as for the SPFLAME data (see Appendix 2.B).

2.3 Near-Inertial Energy in an Eddying Model of the Southern Ocean

Figures 2.1 a,b and 2.2 a,b show NIE in the mixed layer for the primitive-equation-model experiments CONTROL-GCM and SVD-GCM time-averaged for January 2001 and for the whole year 2001. North of approximately $55°S$, high levels of mixed-layer NIE (200 $\mathrm{J/m^2}$ and more) are concentrated in patches of a few degrees in diameter. South of approximately $55°S$ low levels of mixed-layer NIE (100 $\mathrm{J/m^2}$ and less) prevail and spots of high NIE are completely absent. Figures 2.3 a,b and 2.4 a,b show near-inertial WPI for CONTROL-GCM and SVD-GCM time-averaged for January 2001 and for the whole year 2001. As for NIE, high levels of near-inertial WPI (above $1\mathrm{mWm^{-2}}$) occur in relatively small patches. For a detailed examination of the spatial and temporal distribution of NIE and near-inertial WPI in the

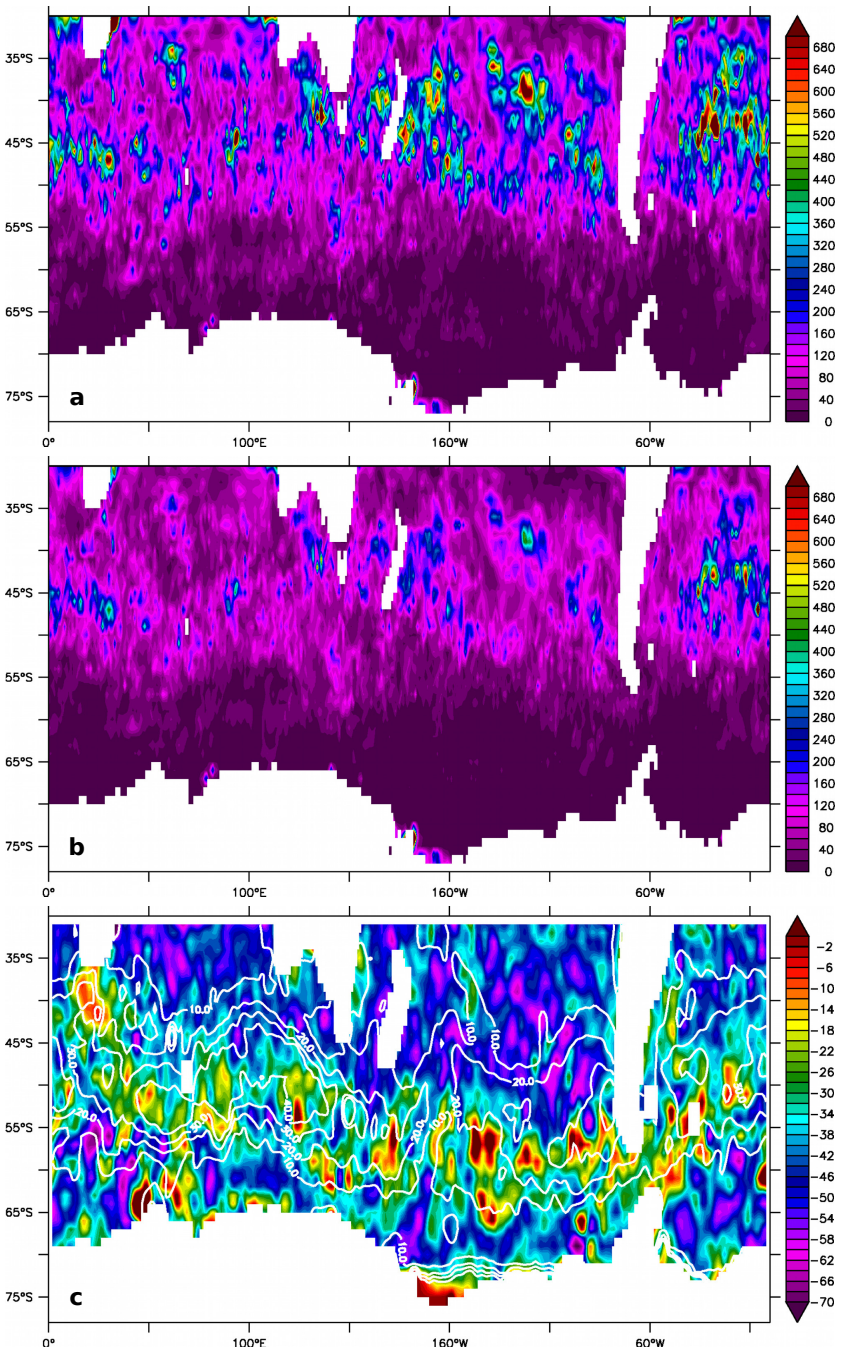

Figure 2.1: *(a) CONTROL-GCM and (b) SVD-GCM time-averaged NIE integrated over the mixed layer (in* Jm^{-2}*) for January 2001. (c) Relative difference of the two (in %), as defined in (2.8), together with the* 10, 20, 30, *and* 40 m *contour lines of time-averaged mixed-layer depth.*

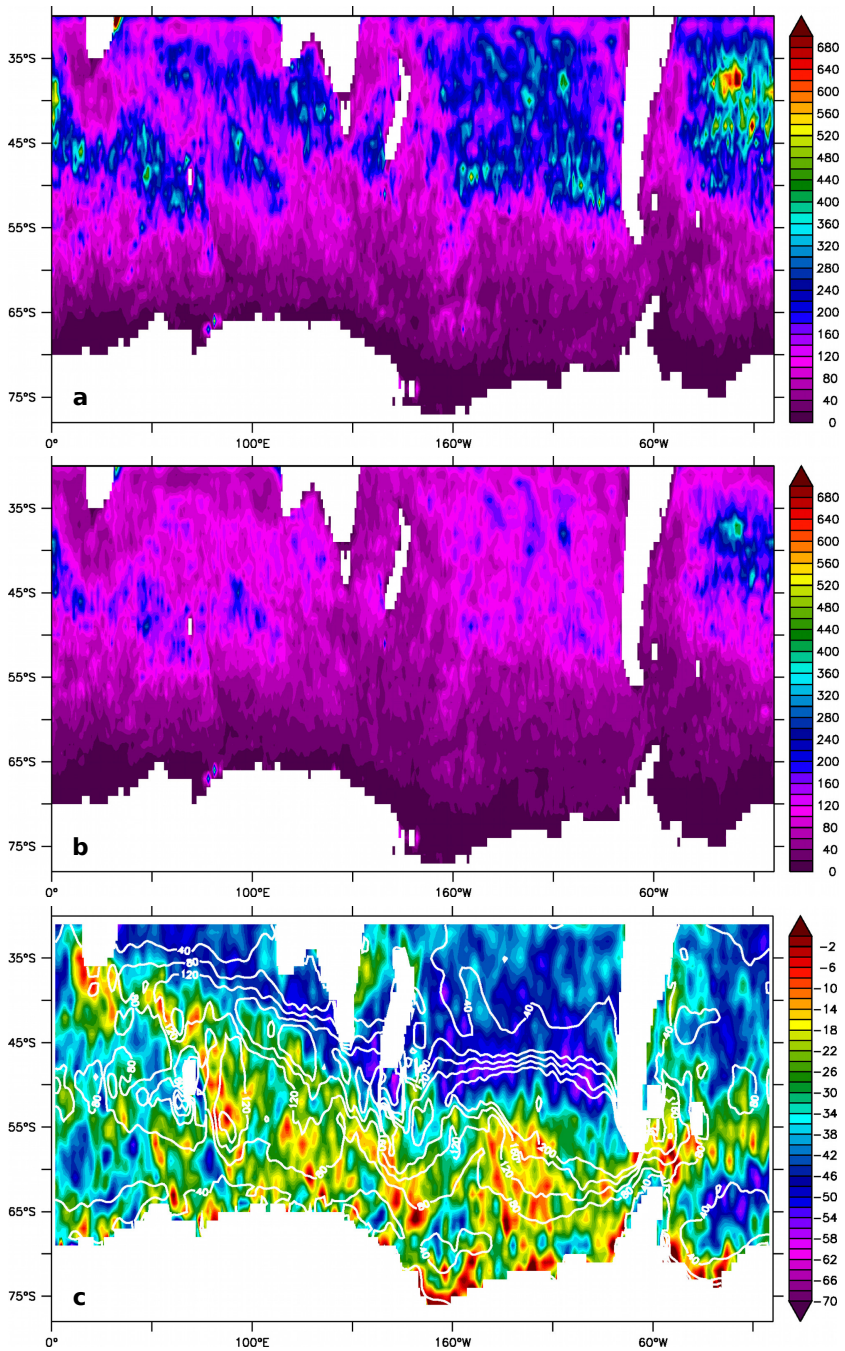

Figure 2.2: *(a) CONTROL-GCM and (b) SVD-GCM time-averaged NIE integrated over the mixed layer (in* Jm^{-2}*) for the whole year 2001. (c) Relative difference of the two (in %), as defined in (2.8), together with the time-averaged mixed-layer depth as contour lines (contour interval* 40 m*).*

Southern Ocean, we refer to the companion paper *Rath et al.* (2013b). *Rath et al.* (2013b) explain the concentration of high NIE and near-inertial WPI at latitudes that are most of the time significantly north of the Southern Hemisphere storm track by the joint effect of a shallow mixed-layer depth north of the Antarctic Circumpolar Current (ACC), and a reduced near-inertial variability of the wind stress at high latitudes due to the increase in the magnitude of the Coriolis parameter at high latitudes.

Figure 2.5 a shows temporally and horizontally averaged NIE from the experiments CONTROL-GCM and SVD-GCM for January 2001 and for the whole year 2001. NIE is concentrated at the surface. In January, when the mixed-layer depth is close to its annual minimum, high NIE is confined to depths less than 100 m. In the whole-year average, high horizontally averaged NIE reaches down to approximately 200 m.

2.4 Influence of the Ocean-Surface-Velocity Dependence of the Wind-Stress on the Near-Inertial Frequency Band

In this section, we first report a large reduction of temporally averaged mixed-layer NIE and near-inertial WPI due to SVD in the primitive-equation-model experiments CONTROL-GCM and SVD-GCM. We then propose a simple mechanism by which the leading-order correction to the wind-stress leads to a reduction of NIE and near-inertial WPI approximately proportional to the inverse of the mixed-layer depth. We test this mechanism by showing that the PM70 slab-ocean model largely captures the reduction of mixed-layer NIE, and by showing that the annual cycle of the reduction is closely tied to the annual cycle of the inverse of the mixed-layer depth.

2.4.1 SPFLAME

When comparing the levels of mixed-layer NIE and of near-inertial WPI in the experiments CONTROL-GCM (See Figure 2.1 a and Figure 2.2 a, and

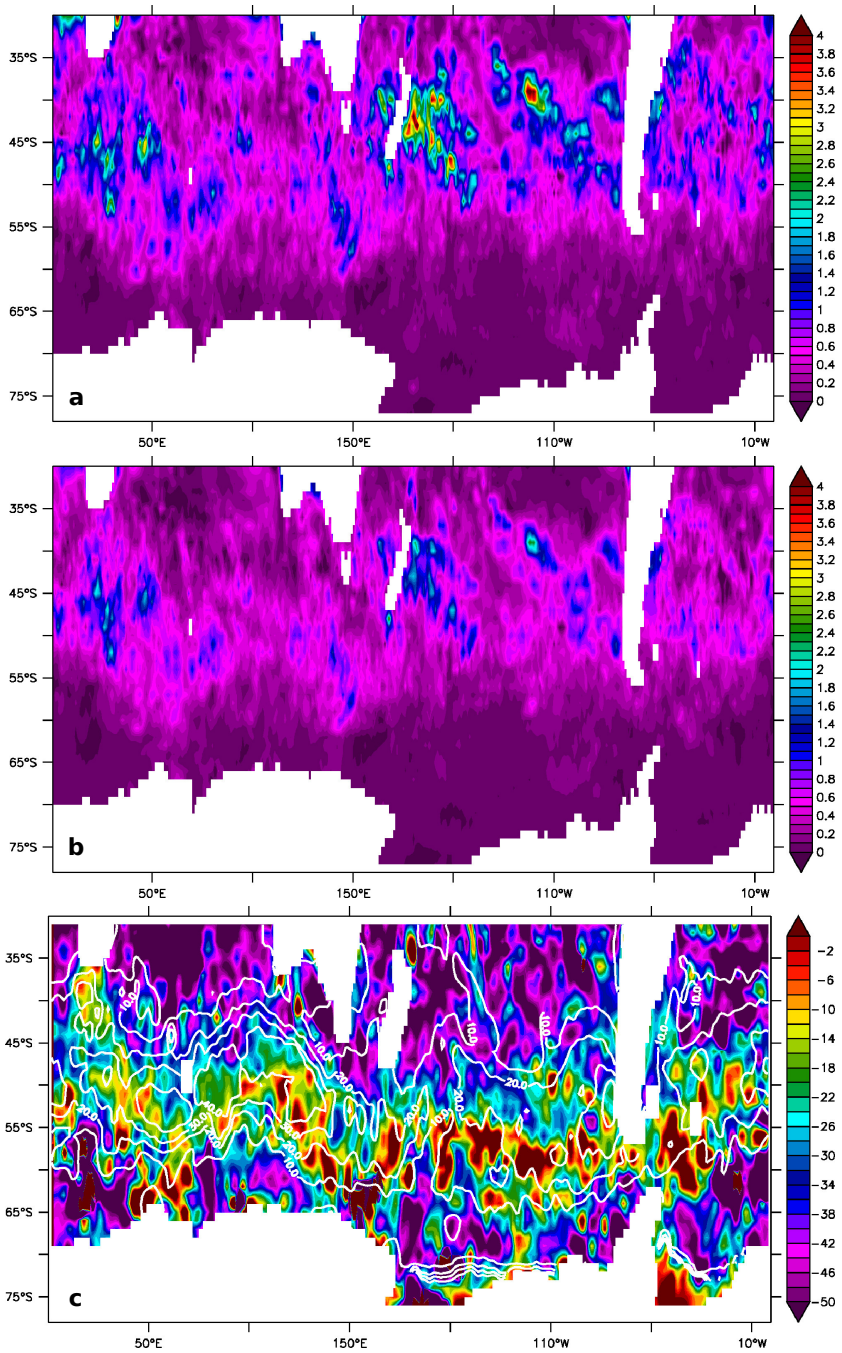

Figure 2.3: *(a) CONTROL-GCM and (b) SVD-GCM time-averaged WPI into the near-inertial frequency band (in* $\mathrm{mWm^{-2}}$*) for January 2001. (c) Relative difference of the two (in %), as defined in (2.9), together with the* 10, 20, 30, *and* 40 m *contour lines of time-averaged mixed-layer depth.*

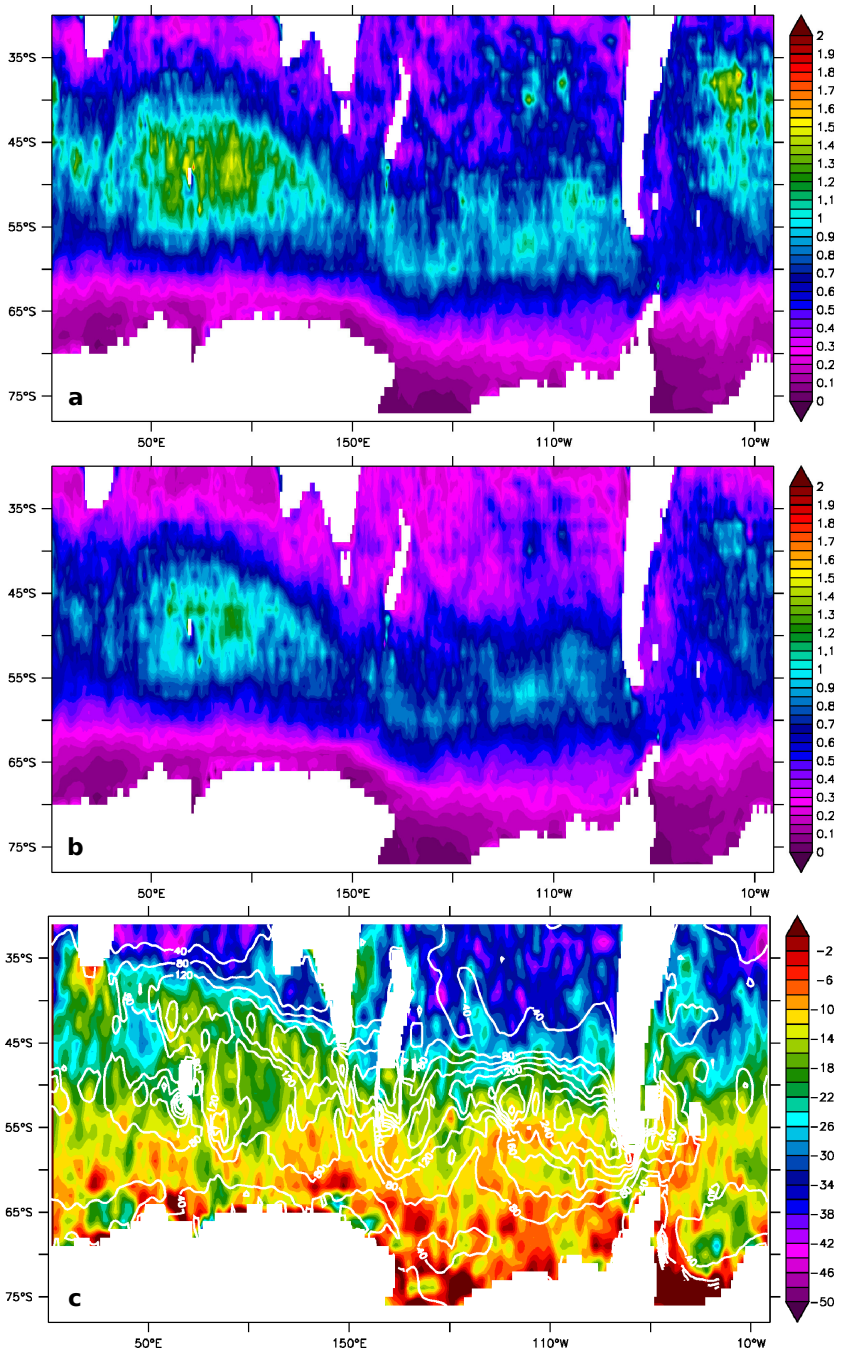

Figure 2.4: *(a) CONTROL-GCM and (b) SVD-GCM time-averaged WPI into the near-inertial frequency band (in* mWm^{-2}*) for the whole year 2001. (c) Relative difference of the two (in %), as defined in (2.8), together with the mixed-layer depth as contour lines (contour interval* 40 m*).*

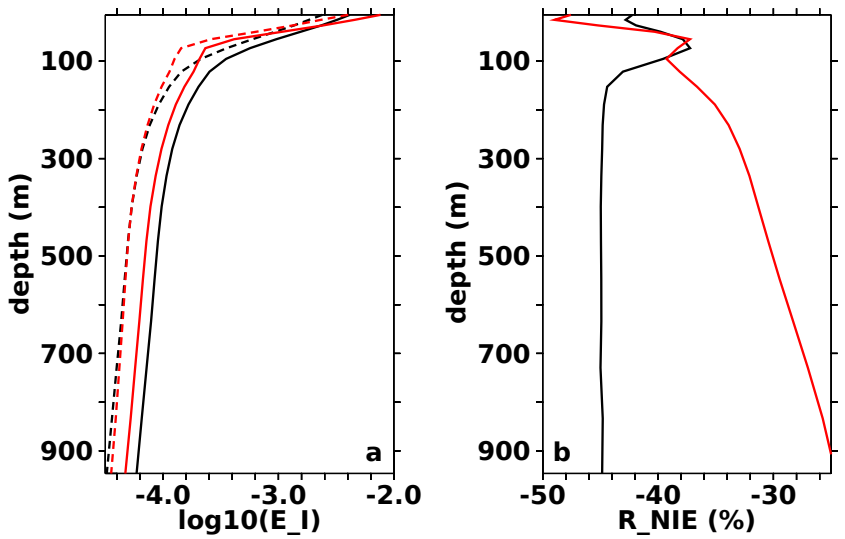

Figure 2.5: *(a)* $\log_{10}$ *of horizontally and temporally averaged NIE (whole model domain) for January 2001 (red) and for the whole year 2001 (black). The solid lines show NIE for the run CONTROL-GCM and the dashed lines show NIE for the run SVD-GCM. (b) Relative difference of horizontally and temporally averaged NIE for January 2001 (red) and for the whole year 2001 (black).*

Figure 2.3 a and Figure 2.4 a respectively.) and in the experiment SVD-GCM (See Figure 2.1 b and Figure 2.2 b, and Figure 2.3 b and Figure 2.4 b respectively.), the most striking difference is the large reduction if the surface-velocity-dependent wind stress is used. To quantify the reduction, we define the relative differences of NIE, R_{NIE}, and of near-inertial WPI, R_{WPI}, as

$$R_{NIE} \equiv \frac{E_I|_{SVD} - E_I|_{CTL}}{E_I|_{CTL}} \tag{2.8}$$

$$R_{WPI} \equiv \frac{WPI_I|_{SVD} - WPI_I|_{CTL}}{WPI_I|_{CTL}} \, . \tag{2.9}$$

Figure 2.1 c and Figure 2.2 c show the relative reduction of time-averaged mixed-layer NIE for January 2001 and for the whole year 2001 together with isolines of the time-averaged mixed-layer depth. The largest reduction (more than 60% in the South Pacific) occurs in January where the mixed layer is shallow. The relative reduction of near-inertial WPI is shown in Figure 2.3 c

and Figure 2.4 c. Again, the largest reduction occurs north of the ACC, when the mixed-layer is shallow. Along the ACC, where the mixed layer is deep, and where a vigorous mesoscale-eddy field is present, the relative reduction of NIE and near-inertial WPI are much smaller.

Table 2.1 lists temporally and horizontally averaged mixed-layer NIE, temporally averaged and horizontally integrated near-inertial WPI, and the relative differences thereof, R_{NIE} and R_{WPI}, for January 2001 and for the whole year 2001. Mixed-layer NIE is reduced by 43.1 % in January 2001 (39.9 % for the whole year), and near-inertial WPI is reduced by 34.5 % in January 2001 (22.1 % for the whole year).

The horizontally averaged view presented in Figure 2.5 shows a large reduction of NIE, which extends to all depths. For January 2001, the relative reduction of NIE is biggest close to the surface and then decays to lower values for greater depths. If the averaging period is extended to the whole year 2001, the reduction of temporally and horizontally averaged NIE is largely uniform throughout the water column. The difference between the average over the whole year, and over only January, indicates that NIE at depth is fed from the NIE that the wind injects at the surface and which in turn spreads to depth from above, as discussed further below.

SVD-GCM is subject to an adjustment to the new wind-stress parameterization. We expect, that in January 2001, when the information about the reduction of NIE at the surface has not yet been transferred to all depths, that the reduction of NIE in the deep ocean is underestimated. Figure 2.7 a, to be discussed in detail later, shows that the mixed-layer NIE is adjusting relatively quickly, while it takes approximately a month before the information about the reduction of the NIE that is injected at the surface reaches the deep ocean. Note that the temporal evolution of horizontally averaged NIE is an integral over many bursts of NIOs in different locations with different mixed-layer depths and hence does not necessarily allow for an estimate of the rate at which NIE is transferred to the deep ocean locally.

2.4.2 Mechanism for Reducing Near-Inertial Energy by Surface-Velocity-Dependent Wind Stress

In the framework of the simple slab-ocean model PM70 (see Section 2.2 for details), the difference of the PM70 wind-stress terms leads to a difference of the wind-power-input term of the energy equation (2.4) that is proportional to the wind speed $|\vec{U}_{10}|$ and to the energy:

$$\frac{\Delta WPI}{\rho_0 H} = -\frac{\rho_a c_d}{\rho_0 H}[1 + (\hat{\vec{u}}_o \cdot \hat{\vec{U}}_{10})^2]|\vec{U}_{10}||\vec{u}_o|^2 = -\epsilon_{SVD}|\vec{u}_o|^2 \tag{2.10}$$

where

$$\epsilon_{SVD} \equiv \frac{\rho_a c_d}{\rho_0 H}[1 + (\hat{\vec{u}}_o \cdot \hat{\vec{U}}_{10})^2]|\vec{U}_{10}| \tag{2.11}$$

with $\hat{\vec{u}}_o = \vec{u}_o/|\vec{u}_o|$. To leading order, the difference of WPI acts like an extra linear-damping term with the damping time scale $1/\epsilon_{SVD}$. It should be noted that the derivation of (2.10) and (2.11) includes two strong assumptions: The mixed-layer depth, H, has been assumed to be time-independent and also the same, irrespective of whether the wind stress contains the SVD or not.

Consider a freely decaying near-inertial oscillation that is only subject to linear damping. The time-integral of NIE is then proportional to the inverse of the linear-damping coefficient. Let $\tilde{\epsilon} = \epsilon + \epsilon_{SVD}$. Then, for the same initial conditions, the relative difference, R_{NIE}, of NIE subject to damping with ϵ alone, compared to damping with $\tilde{\epsilon}$, is $\epsilon_{SVD}/(\epsilon + \epsilon_{SVD})$. If the linear damping due to SVD is of the same size as the linear damping modelling all other processes that remove NIE from the mixed layer, NIE is reduced by 50 %.

The term $(\hat{\vec{u}}_o \cdot \hat{\vec{U}}_{10})^2$ vanishes if the wind vector is orthogonal to the ocean-velocity vector and is one if the wind vector and the ocean-velocity vector are exactly (anti-)parallel. If the relative direction of the wind vector and the ocean-velocity vector is completely random, $(\hat{\vec{u}}_o \cdot \hat{\vec{U}}_{10})^2$ is a Monte-Carlo estimator for $\int_0^{2\pi} \mathrm{d}x \cos^2 x = 0.5$. With $\rho_a = 1.22\,\mathrm{kgm}^{-3}$, $\rho_0 = 1035\,\mathrm{kgm}^{-3}$, $c_d \approx 1.2 \cdot 10^{-3}$, and $(\hat{\vec{u}}_o \cdot \hat{\vec{U}}_{10})^2 \approx 0.5$, the linear-damping due to SVD acts on time scales similar to

$$\frac{1}{\epsilon_{SVD}} \approx 5\,\text{days}\,\frac{H}{|\vec{U}_{10}|}\text{s}^{-1}\ . \tag{2.12}$$

For typical wind speeds around $10\,\text{ms}^{-1}$ the extra damping associated with surface-velocity dependence of the wind stress acts on a timescale of approximately 25 days for $H \approx 50\,\text{m}$ and on a time scale of approximately 5 days for $H \approx 10\,\text{m}$. Earlier studies using PM70 such as that by *D'Asaro* (1985) or *Pollard and Millard* (1970) found a linear-damping time scale, $1/\epsilon$, of 1 to 10 days to be appropriate for modelling observed time series of near-inertial velocity. Hence, with a shallow mixed layer, or with strong winds, ϵ_{SVD} may compete with the other processes that remove NIE from the mixed layer (and, indeed, may be included in the estimate for ϵ given by the above authors).

Plueddemann and Farrar (2006) found that shear instability at the base of the mixed layer is an important sink for NIE in the mixed layer. In SVD-GCM, the reduction in NIE compared to CONTROL-GCM, leads to less vertical shear across the base of the surface-mixed layer and hence less turbulent entrainment there. This rules out the possibility that the reduction of NIE in SVD-GCM is partly due to an increased efficiency of shear instability at the mixed-layer base.

2.4.3 Testing of the Proposed Mechanism for the Reduction of Near-Inertial Energy using PM70 – Summer Conditions

To test the hypothesis that the large reduction of near-inertial energy seen in the primitive-equation experiments can be explained by the direct effect of the changed wind stress, we use the PM70 slab-ocean model. We assume that there is a spatially and temporally universal linear-damping parameter, ϵ, (see equations (2.5) and (2.6)) that can be used to model the distribution of NIE in the Southern Ocean. This is a strong constraint, and, as pointed out by *Plueddemann and Farrar* (2006), a universal damping parameter is not sufficient for accurately modelling the time evolution of near-inertial currents

for long time series. Note also that the choice of the spatial dependence of the linear damping parameter in PM70-like experiments is not agreed upon in the literature. *Alford* (2003) uses a damping coefficient which is proportional to f, while *Watanabe and Hibiya* (2002) use spatially uniform damping coefficients. Hence, we cannot expect the PM70 slab model to account for the spatial distribution of near-inertial energy and its reduction in detail. However, we will show that the broad spatial distribution as well as the magnitude of NIE and its reduction for surface-velocity-dependent wind stress can be captured by PM70.

In the following, we present the results from the experiments CONTROL-SLAB and SVD-SLAB and compare them to those of the experiments CONTROL-GCM and SVD-GCM. In order to isolate the effect of the wind stress parameterization, both PM70 experiments use an explicit damping $\epsilon = 1/4.5\,days$ everywhere. The tuning of the damping parameter is described in Appendix 2.C. In order to test the effect of the change in the wind-stress parameterization, we also use a time-independent mixed-layer depth, H, although, importantly, H varies spatially and is the monthly mean for January diagnosed from CONTROL-GCM as described in Appendix A.

Figure 2.6 a and b show time-averaged mixed-layer NIE for the slab-model experiments. The spatial pattern of NIE in the SPFLAME runs (Figure 2.1) is largely reproduced. However the slab model fails to capture the much finer spatial structure seen in the primitive-equation-model output pointing to the relevance of the mesoscale-eddy field (see, e.g., *Zhai et al.* (2005), *Zhai et al.* (2007), and *Chavanne et al.* (2012)), which is neglected in the PM70 experiments.

Figure 2.6 c shows the relative difference of NIE in the slab-model experiments. There is a broad agreement between PM70 and SPFLAME in showing a large reduction of NIE where the mixed layer is shallow and in showing a small or no reduction where the mixed layer is deep, consistent with expectations from the mixed layer depth dependence in (2.12). It should be noted that there is disagreement in the spatial distribution of the relative reduction of NIE in the South Pacific between $65°S$ and $50°S$. In this region, the NIE reduction modelled by PM70 closely follows the mixed-layer depth,

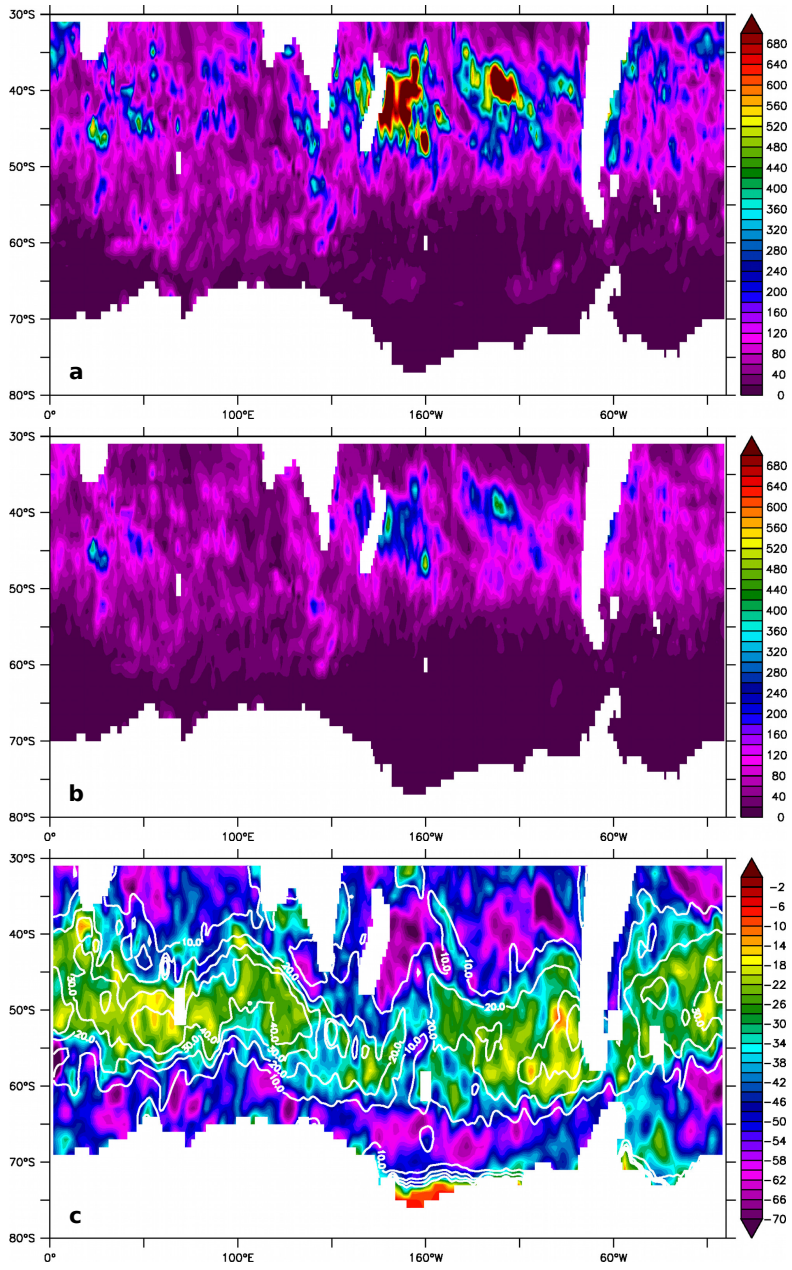

Figure 2.6: *(a) CONTROL-SLAB and (b) SVD-SLAB time-averaged NIE integrated over the mixed layer (in* Jm^{-2}*) for January 2001. (c) Relative difference of the two (in %), as defined in (2.8), together with the* 10, 20, 30, *and* 40 m *contour lines of time-averaged mixed-layer depth.*

as expected, while the NIE reduction as measured from CONTROL-GCM and SVD-GCM is bigger than 65 % even where the mixed layer is relatively deep.

The simple slab-ocean model PM70 confirmed that including the ocean-surface velocity in the parameterization of the wind-stress can directly reduce NIE in the mixed layer by a large amount. Further, despite its simplicity, it is notable that PM70 even largely captured the spatial distribution of the reduction, which, in turn, is controlled primarily by the mixed layer depth.

2.4.4 The Annual Cycle

The mixed-layer depth is subject to a significant annual cycle. At the same location, the mixed-layer depth can vary by an order of magnitude (see, e.g., Figure 5 in *de Boyer Montegut et al.* (2004)). From (2.12), we can expect the reduction of NIE and near-inertial WPI associated with SVD to be tightly related to the annual cycle of the mixed-layer depth.

Figure 2.7 a shows the relative difference of horizontally averaged NIE, R_{NIE}, for the upper 900 m of the water column. The reduction of NIE in the mixed layer is changing from more than 50 % in austral summer, when the mixed-layer is shallow, to approximately 15 % in austral winter, when the mixed layer is deep. Figure 2.7 a also reveals that the reduction of NIE injected at the surface causes a reduction of the levels of NIE in the deep ocean as well. At the beginning of the time series, the adjustment of the experiment SVD-GCM following the change in the wind-stress parameterization is clearly visible. For horizontally averaged NIE, it takes approximately a month until the information about the significant reduction of NIE injected at the surface is transferred to the deep ocean.

Figure 2.7 b and c show the zonally averaged reduction of mixed-layer NIE, R_{NIE}, and of zonally averaged near-inertial WPI, R_{WPI}, together with the zonally averaged mixed-layer depth. In austral summer, the large reduction reaches south to approximately $50°S$, south of which the mixed-layer depth is considerably deeper than in the northern part of the model domain. In fall, the deep mixed-layer expands towards the north and the region of

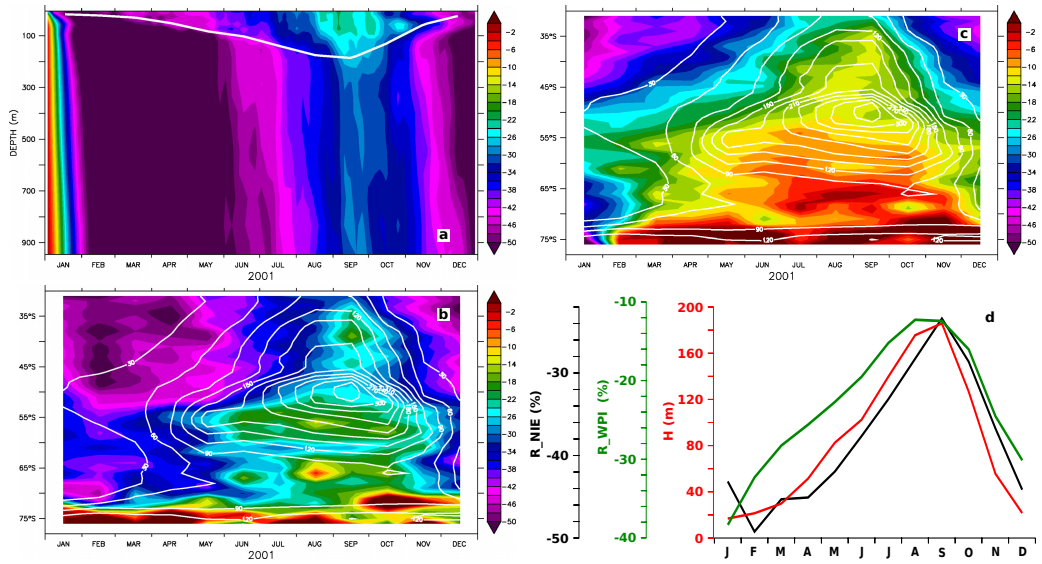

Figure 2.7: *(a) Relative difference of horizontally averaged NIE in the mixed layer (colors) together with the horizontally averaged mixed-layer depth (white contour). (b) Relative reduction of zonally averaged NIE in the mixed layer (colors) together with the zonally averaged mixed-layer depth (contours every* $30\,\mathrm{m}$*). (c) Relative reduction of zonally averaged near-inertial* WPI *(colors) together with the zonally averaged mixed-layer depth (contours every* $30\,\mathrm{m}$*). (d) Relative reduction of horizontally averaged NIE in the mixed layer (black line) and relative reduction of horizontally averaged near-inertial* WPI *(green line) together with the horizontally averaged mixed-layer depth (red line). Relative differences are all given as defined in (2.8) and (2.9) in percent.*

the large reduction retreats accordingly, until in winter the reduction has reduced to its annual minimum. As the mixed-layer gets shallower in spring, the reduction recovers its largest extent again.

Figure 2.7 d summarizes Figure 2.7 a,b,c by showing that both, the reduction of horizontally averaged mixed-layer NIE, R_{NIE}, and the reduction of horizontally averaged near-inertial WPI closely follow the horizontally averaged mixed-layer depth, and that the annual minima and maxima of both almost exactly coincide with the annual maxima and minima of the mixed-layer depth.

2.5 Summary and Conclusion

We have used an eddying realistic primitive-equation model of the Southern Ocean to examine the relevance of the ocean-surface-velocity-dependence of the wind stress for determining NIE and for WPI into the near-inertial frequency band. We found a large reduction of both NIE and WPI into the near-inertial frequency band if the wind-stress parameterization accounts for the ocean-surface velocity. Averaged over the whole year, 2001, horizontally averaged mixed-layer NIE is reduced by 39.9 % and horizontally averaged WPI is reduced by 22.1 %. Locally, much larger reductions are found especially in the South Pacific. As NIE at depth in our model mainly feeds from NIE injected into the surface-mixed layer, there is a reduction of NIE all throughout the water column.

The reduction of NIE is due to the fact that including ocean-surface-velocity in the wind stress amounts, to leading order, to adding a linear-damping term to the momentum equation for the surface-mixed layer. This linear-damping term is proportional to the inverse of the mixed-layer depth. Using the slab-ocean model first described by *Pollard and Millard* (1970), we confirmed that a large part of the observed reduction of near-inertial WPI and NIE can be explained by the direct effect of the changed wind-stress parameterization. By examining the annual cycle of NIE and the mixed-layer depth, we confirmed that it is in fact the inverse mixed-layer depth which mainly determines the strength of the reduction of NIE.

Our findings show that ocean-surface-velocity dependence of the wind stress has a big effect on wind-induced near-inertial oscillations and hence should be taken into account when WPI into the near-inertial frequency band is estimated.

2.A The Mixed-Layer Depth

The mixed-layer depth used in this paper is defined as the depth at which the modulus of the deviation of the primitive-equation-model potential temperature to the surface temperature equals $\Delta T = 0.3\,\mathrm{K}$. ΔT has been chosen so that the mixed-layer depth approximately matches the depth at which the ratio $E_I(z)/E_I(0) \approx 1/e$ in regions with strong NIE, where $E_I(z)$ is the energy in the inertial frequency band at depth z. In the PM70 experiments, the mixed-layer depth, H, is taken to be the mean mixed-layer depth at each horizontal grid point over the month of January 2001. We compared different definitions for the mixed-layer depth and found that the results of this study are not significantly changed.

2.B Time Filtering

The model output from the experiments CONTROL-GCM and SVD-GCM and from the corresponding PM70 experiments was filtered using a fifth-order Butterworth filter similar to the one used by *Zhai et al.* (2009). We chose the cutoff frequencies to match the Coriolis parameter f at the latitudes $28°S$ and $80°S$ which are just north and south of the boundaries of the model domain. Using the filter, the velocity was split into sub-inertial (S), near-inertial (I), and super-inertial (T) components

$$\vec{u} \equiv \vec{u}_S + \vec{u}_I + \vec{u}_T \ . \tag{2.13}$$

Kinetic energy for each frequency band is then defined as

$$E_{S,I,T} \equiv \frac{u_{S,I,T}^2 + v_{S,I,T}^2}{2} \tag{2.14}$$

To avoid complications from the band-pass filter, which needs a couple of days data to be fully defined, we chose to neglect the first five and the last five days of the filtered data.

2.C Tuning of the PM70 Experiment CONTROL-SLAB

Figure 2.8 compares the mixed-layer-averaged zonal near-inertial velocity from the experiment CONTROL-GCM and the zonal near-inertial velocity from PM70 at $100°E$ and $45°S$. PM70 is forced by the same wind-forcing as CONTROL-GCM, and is the same as used in CONTROL-SLAB. The mixed-layer depth from the experiment CONTROL-GCM $H = 36.1\,\mathrm{m}$ was used. The linear-damping parameter $\epsilon = 1/4.5\,\mathrm{days}$ was chosen by comparing PM70 output for different ϵ, and primitive-equation-model output from the experiment CONTROL-GCM. There are six to seven separate bursts of inertial oscillations and it is evident that PM70 does not capture the magnitude and shape of all of them.

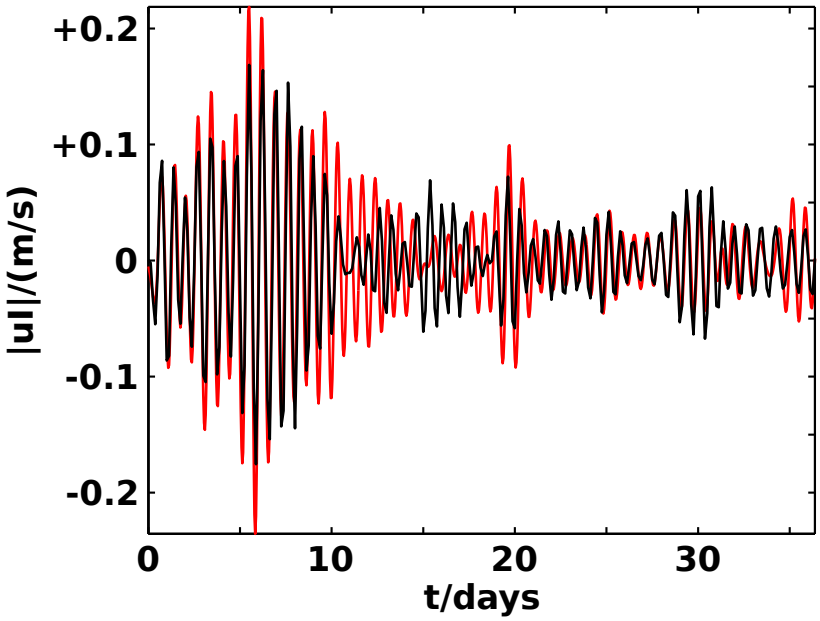

Figure 2.8: *Zonal near-inertial velocity at* $100°E$ *and* $45°S$*. The black line shows* u_I *averaged over the mixed layer for the first* $36.5\,\text{days}$ *of the experiment CONTROL-GCM and the red line shows* u_I *as modeled by PM70 using the same wind forcing, mixed-layer depth* $H = 36.1\,\text{m}$ *and* $\epsilon = 4.5\,\text{days}$*.*

Chapter 3

Sub-Inertial Response to Ocean-Surface-Velocity Dependence of the Wind Stress in a Model of the Southern Ocean

Willi Rath, Richard J. Greatbatch[1]

Abstract: We seek to understand the influence of including or neglecting the surface-velocity of the ocean in the wind-stress parameterization on the dynamics of the Southern Ocean. We do so by comparing model output from a regional realistic primitive-equation model of the Southern Ocean driven by different wind-stress parameterizations. The influence of surface-velocity dependence of the wind-stress on wind power input, eddy kinetic energy (EKE), and depth-integrated transport are examined with respect to the time-mean circulation, and the monthly and inter-annual variability. We confirm, that surface-velocity-dependent wind stress leads to a reduction of wind power input and EKE as found by earlier studies. We do, however, find

[1]This chapter will be submitted to *Ocean Dynamics*.

that surface-velocity-dependent wind stress only leads to a minor increase in eastward transport of the Antarctic Circumpolar Current, which contradicts earlier findings based on idealized models.

3.1 Introduction

Since the ocean-surface velocity is typically smaller than the wind velocity by one to two orders of magnitude, it is often neglected when parameterizing the wind stress (*Duhaut and Straub*, 2006). The wind stress is then calculated from the 10-m-wind-velocity vector $\vec{U}_{wind}$ alone[2]

$$\vec{\tau}_{ctrl} \equiv \rho_a c_d(|\vec{U}_{wind}|)|\vec{U}_{wind}|\vec{U}_{wind} \ . \tag{3.1}$$

Alternatively, the wind stress can be parameterized in terms of the difference between the wind-velocity vector and the ocean-surface-velocity vector $\vec{u}_{oecan}$

$$\vec{\tau}_{svd} \equiv \rho_a c_d(|\vec{U}_{wind} - \vec{u}_{oecan}|)|\vec{U}_{wind} - \vec{u}_{oecan}|(\vec{U}_{wind} - \vec{u}_{oecan}) \tag{3.2}$$

The effect of surface-velocity dependence (SVD) of the wind stress has been examined both using model-based and observational approaches. *Pacanowski* (1987) compares simulations of the tropical Atlantic using a regional primitive equation model driven by both $\vec{\tau}_{ctrl}$ and $\vec{\tau}_{svd}$. He finds, that SVD reduces the velocity of the equatorial current system and renders the modelled currents more realistic. He also finds that SVD reduces a model bias towards too cold sea-surface temperature (SST) at the equator. *Luo et al.* (2005) find that in a coupled ocean-atmosphere general-circulation model, the SST bias in the equatorial Pacific is reduced if the motion of the ocean is accounted for in the atmosphere-ocean momentum transfer. *Dewar and Flierl* (1987) examined air-sea interactions above Gulf-Stream rings and find that SVD leads to a general damping of the ocean currents. *Duhaut and Straub* (2006) show, using a quasi-geostrophic double-gyre ocean model, that SVD can lead to a reduction of wind power input (WPI) to the geostrophic flow

[2]See Section 3.2.1 for details on the wind-stress parameterization.

of up to 30 %, where the circulation is strong. *Hughes and Wilson* (2008) and *Xu and Scott* (2008) present observational support for the SVD-induced reduction of geostrophic WPI found by *Duhaut and Straub* (2006) based on scatterometer-wind data and ocean-surface currents derived from satellite altimetry. *Zhai and Greatbatch* (2007) find that mesoscale eddy kinetic energy (EKE) is reduced by about 10 % in a regional model of the Northwest Atlantic through SVD and note, that doing so leads to an additional sink for the kinetic energy of mesoscale eddies. Using a regional quasi-geostrophic model, *Hutchinson et al.* (2010) confirm both the SVD-induced reduction of geostrophic WPI found in earlier studies (*Duhaut and Straub*, 2006; *Hughes and Wilson*, 2008; *Xu and Scott*, 2008), and the SVD-induced damping of the EKE found by *Zhai and Greatbatch* (2007). *Rath et al.* (2013a) find that by a mechanism similar to the SVD-induced reduction of mesoscale EKE, using $\vec{\tau}_{svd}$ in a realistic primitive-equation model of the Southern Ocean leads to a reduction of WPI into the near-inertial frequency band by approximately 20 % and to a reduction of near-inertial energy by approximately 40 %.

To our knowledge, there is no study examining the effect of ocean-surface-velocity dependence of the wind stress using a realistic eddying model of the Southern Ocean. *Hutchinson et al.* (2010) use a quasi-geostrophic model to test the effect of SVD on the dynamics of the the Antarctic Circumpolar Current (ACC). They find the eastward transport associated with the ACC to increase by 25 % if SVD is used, and attribute this increase to a combination of a weakened eddy field and eddy-saturation (*Straub*, 1993). However, *Hutchinson et al.* (2010) note, that the absence of any thermodynamic effects and the absence of an overturning circulation in their quasi-geostrophic approach calls for a test of the effect of SVD in a realistic model.

In this study, we examine the effect of using the surface-velocity dependent $\vec{\tau}_{svd}$ instead of the simplified $\vec{\tau}_{ctrl}$ to drive a realistic eddying primitive-equation model of the Southern Ocean. Section 3.2 presents details on the different wind-stress parameterization and on the model used in this study. Section 3.3 covers the response of the modelled wind-forcing, of the modelled mean-state and of the modelled variability to SVD. In Section 3.4, we summarize and discuss the results.

3.2 Methods, Models, Data

3.2.1 Wind-Stress Parameterization

We examine the effect of changing the wind-stress parameterization from a formulation that neglects the surface currents of the ocean

$$\vec{\tau}_{ctrl} \equiv \rho_a c_d(|\vec{U}_{wind}|)|\vec{U}_{wind}|\vec{U}_{wind} \tag{3.3}$$

to a formulation which includes the ocean surface-velocity

$$\vec{\tau}_{svd} \equiv \rho_a c_d(|\vec{U}_{wind} - \vec{u}_{oecan}|)|\vec{U}_{wind} - \vec{u}_{oecan}|(\vec{U}_{wind} - \vec{u}_{oecan}) \tag{3.4}$$

In the above equations, $\vec{U}_{wind}$ is the 10-m-wind vector, $\vec{u}_{ocean}$ is the ocean-surface-velocity vector, ρ_a is the density of air at sea level, and $c_d(U)$ is the drag coefficient. We chose to parameterize c_d according to *Large and Pond* (1981) with a levelling off for high wind-speeds according to *Donelan et al.* (2004).

As *Duhaut and Straub* (2006) show, changing the wind-stress parameterization from (3.3) to (3.4), keeping the ocean-surface velocity unchanged, and approximating c_d by a constant, amounts, to leading order, to adding two sink terms to WPI. Let

$$WPI_{ctrl} \equiv \vec{\tau}_{ctrl} \cdot \vec{u}_{ocean} \tag{3.5}$$

and

$$WPI_{svd} \equiv \vec{\tau}_{svd} \cdot \vec{u}_{ocean} \ . \tag{3.6}$$

Then, the difference of WPI for the two wind-stress parameterizations is

$$\Delta WPI \equiv WPI_{svd} - WPI_{ctrl} \tag{3.7}$$

$$\Delta WPI = -\rho_a c_d|\vec{U}_{wind}|[|\vec{u}_{ocean}|^2 + (\vec{u}_{ocean} \cdot \hat{U}_{wind})^2] \tag{3.8}$$

$$\Delta WPI = -\rho_a c_d|\vec{U}_{wind}|[1 + (\hat{u}_{ocean} \cdot \hat{U}_{wind})^2]|\vec{u}_{ocean}|^2 \tag{3.9}$$

where the unit vectors $\hat{U}_{wind} = \vec{U}_{wind}/|\vec{U}_{wind}|$ and $\hat{u}_{ocean} = \vec{u}_{ocean}/|\vec{u}_{ocean}|$ have

been defined. The first term of (3.9) is proportional to $|\vec{u}_{ocean}|^2$ and acts irrespective of the wind-direction. The second term of (3.9) is proportional to $(\hat{u}_{ocean} \cdot \hat{U}_{wind})^2 |\vec{u}_{ocean}|^2$ and hence is biggest when $\vec{u}_{ocean}$ and $\vec{U}_{wind}$ are either parallel or anti-parallel.

3.2.2 Computing Wind-Power Input and Eddy Kinetic Energy

Wind-fluctuations at frequencies close to the local Coriolis frequency accelerate near-inertial waves (*D'Asaro*, 1985; *Alford*, 2003). *Rath et al.* (2013a) show that surface-velocity dependent wind stress significantly reduces near-inertial WPI and near-inertial energy. In this study, we want to highlight the oceanic response to SVD on monthly to inter-annual time scales. We hence chose to calculate these low-frequency parts of WPI from monthly-mean fields of the wind stress and ocean velocity. Likewise, we chose to neglect the high-frequency velocity fluctuations and calculate the mesoscale EKE from monthly averages of the velocity fields.

3.2.3 The Model and Experiments

We use a regional setup of the Southern Ocean of SPFLAME, which is described by *Eden* (2006). The model covers all ocean south of $30°S$ at eddying horizontal resolution of $(1/10)°$. It has 42 vertical levels with thicknesses ranging from 10 m near the surface to 250 m at 5500 m depth and a realistic topography (Figure 3.1a). In the north, an open boundary condition with prescribed barotropic in- and outflow and restoring to climatological values of potential temperature and salinity is used. The model is driven by climatological surface heat flux (*Barnier et al.*, 1995). Sea surface salinity is restored to climatological values with an e-folding scale of 15 days for the upper 10 m. Vertical mixing is parameterized using the TKE-scheme (*Gaspar et al.*, 1990; *Blanke and Delecluse*, 1993) and horizontal mixing is parameterized as a bi-harmonic diffusivity in both, the momentum and the tracer equation. The model is spun up from a state of rest and from a climatological hydrography

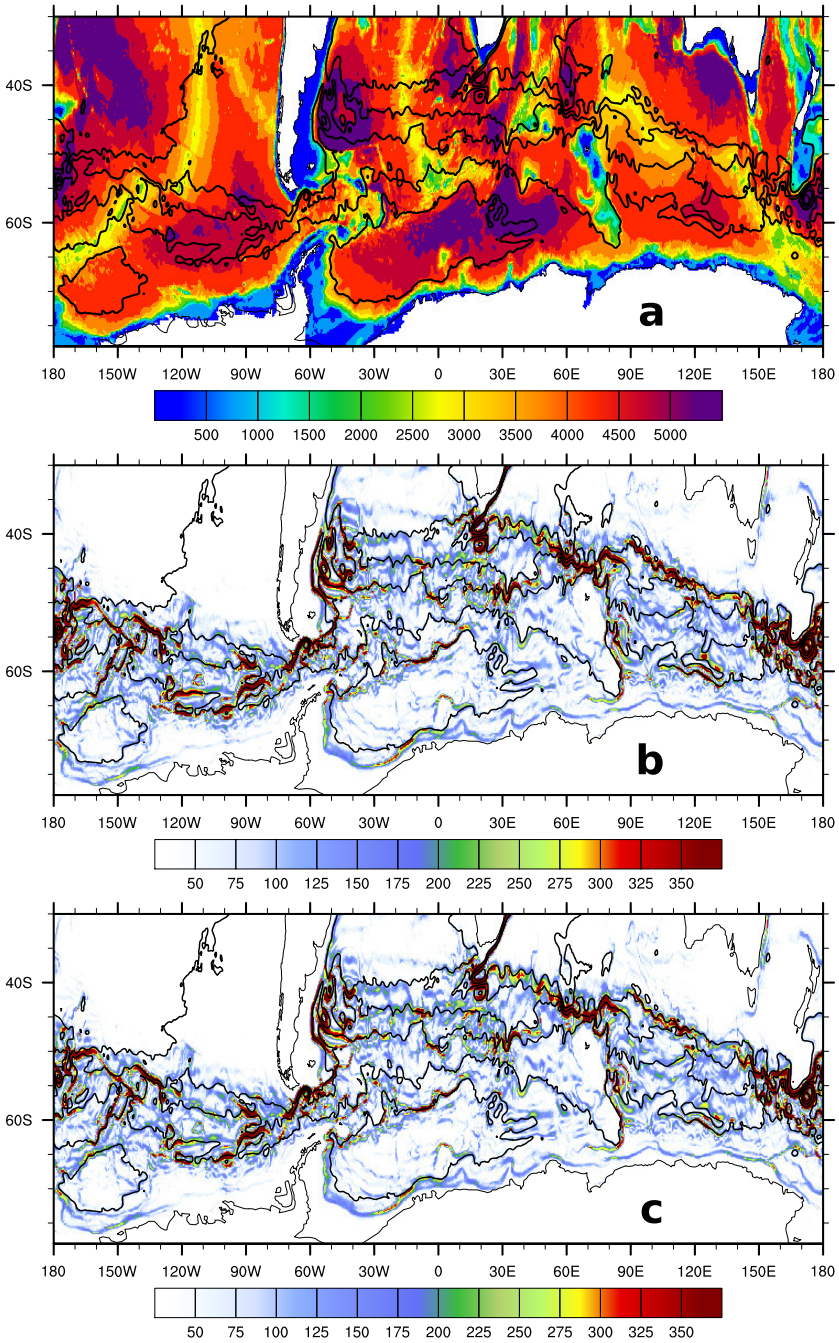

Figure 3.1: *(a) Colors show model bathimetry* (m)*. Contours show the time-averaged barotropic stream function for the experiment ERA40-CTRL using a* 40 Sv *interval. (b) Colors show the depth integrated flow* ($|\int \vec{u}\mathrm{d}z|$) *in* m^2/s *for the experiment ERA40-CTRL together with the contours from panel (a). (c) Colors show the depth integrated flow* ($|\int \vec{u}\mathrm{d}z|$) *in* m^2/s *for the experiment ERA40-SVD together with the contours of panel (a).*

(*Levitus et al.*, 1994; *Levitus and Boyer*, 1994) for 10 years using climatological wind stress parameterized by the conventional $\vec{\tau}_{ctrl}$ (*Barnier et al.*, 1995).

After the spin-up phase, we fork the model into four experiments which are all run for 22 years:

- **ERA40-CTRL** uses realistic wind stress derived from 6-hourly 10-m-wind fields from the years 1980 to 2001 ERA40 reanalysis (*Uppala et al.*, 2005) using the parameterization $\vec{\tau}_{ctrl}$.
- **ER40-SVD** is identical to ERA40-CTRL, but uses the wind-stress parameterization $\vec{\tau}_{svd}$.
- **CLIM-CTRL** uses climatological wind stress parameterized by $\vec{\tau}_{ctrl}$. It is essentially a continuation of the spin-up phase.
- **CLIM-SVD** is identical to CLIM-CTRL, but uses the wind-stress parameterization $\vec{\tau}_{svd}$.

3.3 Results

3.3.1 Response of the Mean Wind Forcing

Over the Southern Ocean, the wind-stress is dominated by a zonal band of westerly winds between approximately $65°S$ and $40°S$ (Figure 3.2a and b and Figure 3.3) which projects well onto the predominantly eastward surface flow associated with the ACC and leads to positive WPI along the path of the ACC (Figure 3.4a and b and Figure 3.5).

SVD reduces the horizontally and temporally averaged magnitude of the wind-stress vector experiments by 5.1 % for the ERA40 and by 2.9 % for the CLIM experiments (Table 3.1), but does not alter the large-scale spatial pattern of the wind stress (Figure 3.2a and b and Figure 3.3). The largest reduction of the wind stress is found between approximately $40°S$ and $60°S$ (Figure 3.2c, and Figure 3.3). An increase of the wind stress can be found

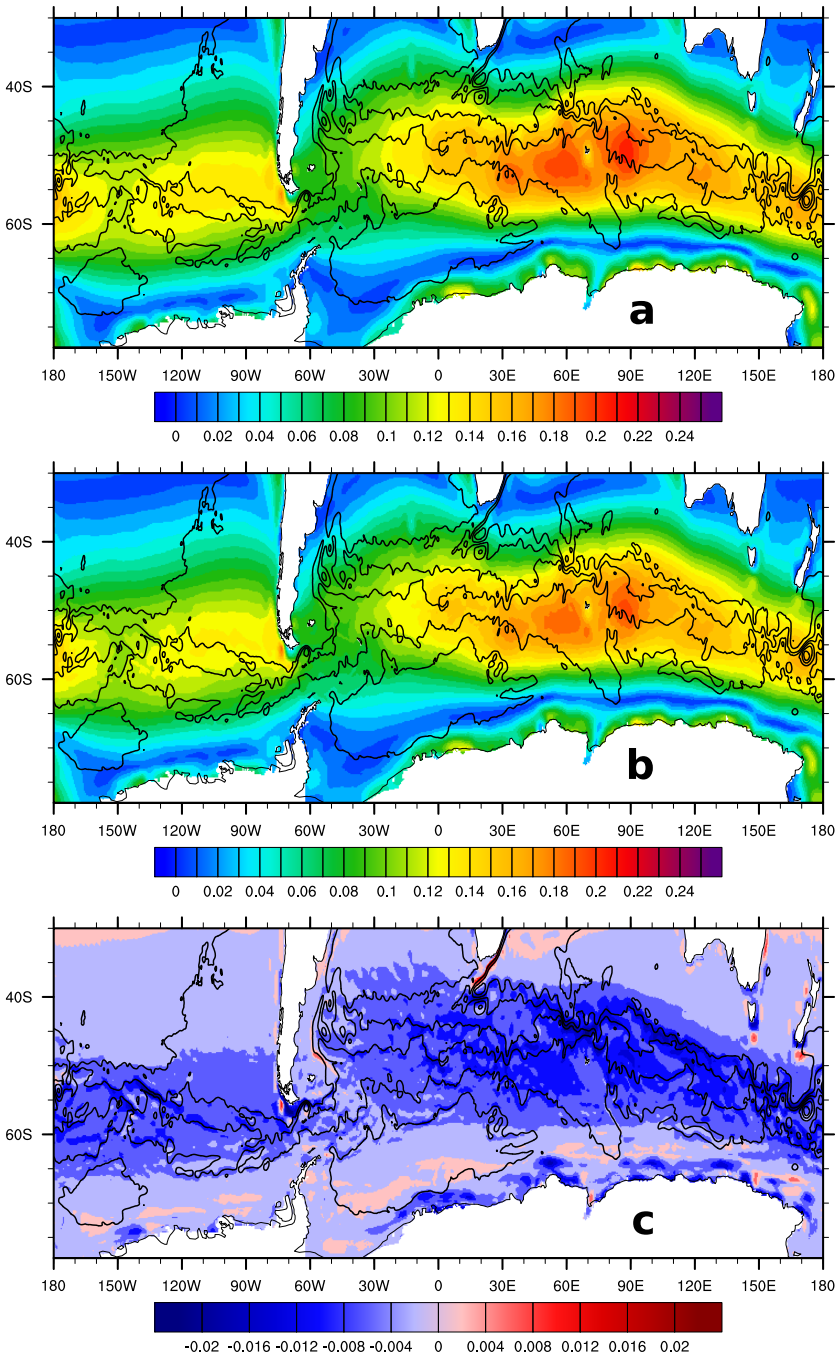

Figure 3.2: *(a) Time-averaged magnitude of the wind stress* $|\vec{\tau}|$ *in* $\mathrm{N/m^2}$ *for the experiment ERA40-CTRL. (b) Same as (a) for the experiment ERA40. (c) Difference (b) minus (a). Contours show the time-averaged barotropic stream function for the experiment ERA40-CTRL using a* 40 Sv*-interval.*

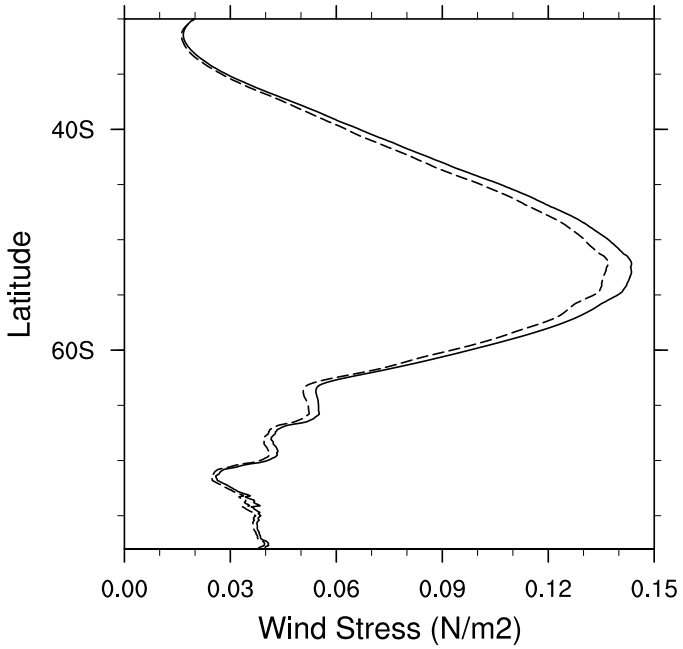

Figure 3.3: *Zonally averaged magnitude of the wind stress* $|\vec{\tau}|$ *calculated from time-averaged* τ^x *and* τ^y *in* $\mathrm{N/m^2}$ *for the experiments ERA40-CTRL (solid) and ERA40-SVD (dashed).*

south of South Africa, where the Agulhas Current flows against the prevailing wind direction, and east of Argentina, where the ACC flows north-westward.

Likewise, horizontally and temporally averaged WPI is reduced by 14.9 % or 9.4 % for the ERA40- and the CLIM-experiments respectively (Table 3.2) while the spatial pattern with strong positive WPI between approximately $65°S$ and $40°S$, where the ACC and the westerly winds align, is not affected (Figure 3.4). The largest positive contribution to WPI in the Southern Ocean is found along the path of the ACC, where the predominantly eastward wind-stress vector projects onto the eastward surface-velocity associated with the ACC (Figure 3.4a and b). The largest reduction of WPI induced by SVD is associated with the ACC (Figure 3.4c and Figure 3.5). This is predicted by (3.9), according to which the reduction of WPI is proportional to $|\vec{u}_{ocean}|^2$. It is furthermore consistent with the findings of *Hughes and Wilson* (2008) and *Xu and Scott* (2008), who show that estimating WPI into the geostrophic circulation from scatterometer winds and satellite altimetry leads to an over-

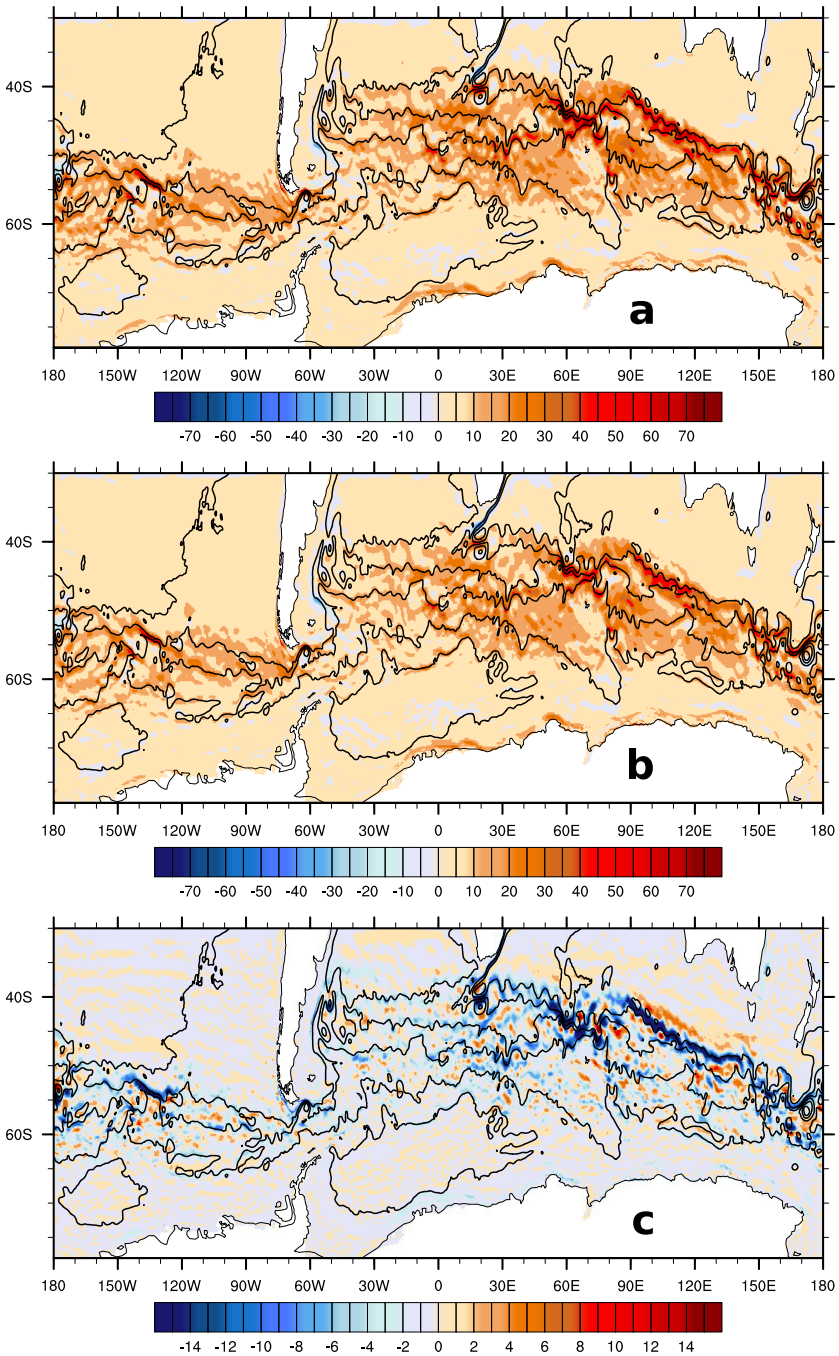

Figure 3.4: *(a) Time-averaged WPI in* $10^{-3}\mathrm{W/m^2}$ *for the experiment ERA40-CTRL. (b) Same as (a) for the experiment ERA40-SVD. (c) Difference (b) minus (a). Contours show the time-averaged barotropic stream function for the experiment ERA40-CTRL using a* 40 Sv*-interval.*

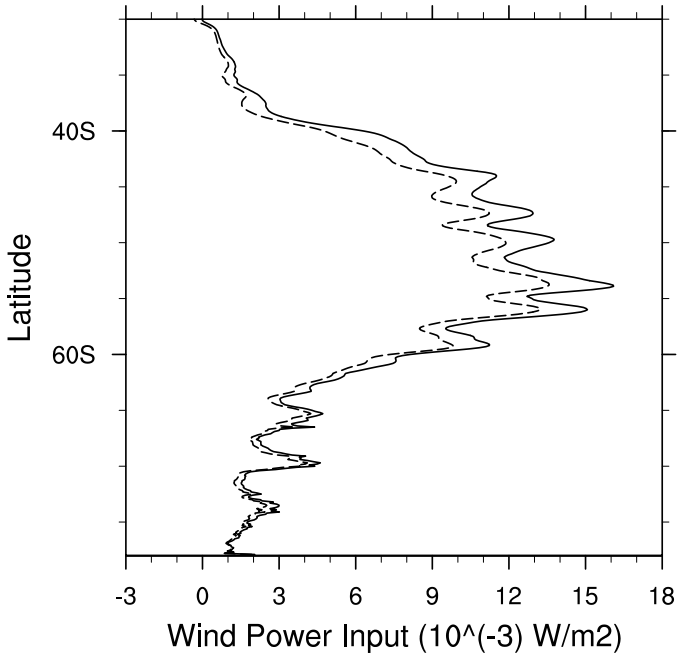

Figure 3.5: *Zonally and temporally averaged WPI ($10^{-3}\,\mathrm{W/m^2}$) for the experiments ERA40-CTRL (solid) and ERA40-SVD (dashed).*

Experiment	$\langle\overline{\lvert\vec{\tau}\rvert}\rangle$	$STD_{det,ann}$	$STD_{det,noac}$	STD_{ac}
ERA40-CTRL	80.90	3.43	5.91	10.91
ERA40-SVD	76.79	3.29	5.63	10.01
Δ_r	$-5.1\,\%$	$-4.2\,\%$	$-4.7\,\%$	$-8.2\,\%$
CLIM-CTRL	95.31	—	—	10.33
CLIM-SVD	92.56	0.011	0.011	10.04
Δ_r	$-2.9\,\%$	—	—	$-2.8\,\%$

Table 3.1: *$\langle\overline{\lvert\vec{\tau}\rvert}\rangle$ denotes the temporal and horizontal mean of $\lvert\vec{\tau}\rvert$. $STD_{det,ann}$ denotes the temporal standard deviation of the detrended and horizontally averaged annual-mean $\lvert\vec{\tau}\rvert$. $STD_{det,noac}$ denotes the temporal standard deviation of the detrended horizontally averaged monthly-mean $\lvert\vec{\tau}\rvert$ with the the annual cycle removed. STD_{ac} denotes the temporal standard deviation of the annual cycle of horizontally averaged $\lvert\vec{\tau}\rvert$. $\lvert\vec{\tau}\rvert$ is based on monthly-mean wind-stress components. Δ_r denotes the relative difference defined as (SVD-CTRL)/CTRL. All numbers except for Δ_r are given in $10^{-3}\mathrm{N/m^2}$.*

Experiment	$\langle\overline{WPI}\rangle$	$STD_{det,ann}$	$STD_{det,noac}$	STD_{ac}
ERA40-CTRL	7.12	0.3955	0.827	1.47
ERA40-SVD	6.06	0.3565	0.747	1.31
Δ_r	$-14.9\,\%$	$-10.8\,\%$	$-9.7\,\%$	$-10.9\,\%$
CLIM-CTRL	8.52	0.0106	0.046	1.56
CLIM-SVD	7.72	0.0149	0.035	1.46
Δ_r	$-9.4\,\%$	$+40.6\,\%$	$-24\,\%$	$-7.1\,\%$

Table 3.2: *$\langle\overline{WPI}\rangle$ denotes the temporal and horizontal mean of WPI. $STD_{det,ann}$ denotes the temporal standard deviation of horizontally averaged detrended annual-mean WPI. $STD_{det,noac}$ denotes the temporal standard deviation of horizontally averaged detrended monthly-mean WPI with the annual cycle removed. STD_{ac} denotes the temporal standard deviation of the annual cycle of horizontally averaged WPI. WPI is based on monthly-mean surface velocity and monthly-mean wind stress. Δ_r denotes the relative difference defined as (SVD-CTRL)/CTRL. All numbers except for Δ_r are given in* $10^{-3}\mathrm{W/m^2}$.

estimated WPI if $\vec{\tau}_{ctrl}$ is used, and who find the effect to be particularly large along the path of the ACC.

Note that the modelled reduction of WPI shown in Figures 3.4c shows many small scale features which we attribute to the different realizations of the mesoscale-eddy field of the experiments shown here. Note that there are no such small-scale features in the estimates of ΔWPI presented by *Hughes and Wilson* (2008) and *Xu and Scott* (2008). This is due to the fact, that these studies base their calculations on a single realization of the mesoscale-eddy field (the real world).

In summary, we can confirm that including SVD in the wind-stress parameterization leads to a strong reduction of the modelled wind stress and of the modelled WPI.

3.3.2 Response of the Circulation

The transport of the ACC is concentrated in fronts (*Orsi et al.*, 1995), that are often no wider than a degree (Figure 3.1a). The flow is obviously steered by topography (see also *Orsi et al.* (1995) and *Hughes and Ash* (2001)).

Experiment	$\overline{D}$	$STD_{det,ann}$	$STD_{det,noac}$	STD_{ac}
ERA40-CTRL	121.8	2.33	4.53	1.73
ERA40-SVD	124.0	2.01	4.20	1.53
Δ_r	+1.8 %	−13.6 %	−7.3 %	−11.6 %
CLIM-CTRL	119.7	1.12	2.57	2.10
CLIM-SVD	121.9	1.20	2.57	1.81
Δ_r	+1.8 %	+7.0 %	0 %	−13.8 %

Table 3.3: *$\overline{D}$ denotes the temporal mean of DPT. $STD_{det,ann}$ denotes the temporal standard deviation of detrended annual-mean DPT. $STD_{det,noac}$ denotes the temporal standard deviation of the detrended monthly-mean DPT with the annual cycle removed. STD_{ac} denotes the temporal standard deviation of the annual cycle of DPT. Δ_r denotes the relative difference defined as (SVD-CTRL)/CTRL. All numbers except for Δ_r are given in* Sv.

Changing the wind-stress parameterization shows almost no effect on the location and width of the ACC fronts (compare Figures 3.1b and c). We find a small but significant increase of depth-integrated transport through Drake Passage (DPT), which is the canonical metric for the strength of the ACC (*Cunningham et al.*, 2003), of 1.8 % for both the ERA40- and the CLIM-experiments (Table 3.3 and Figure 3.9 which is discussed in detail in Section 3.3.3). This is in contrast to *Hutchinson et al.* (2010), who find that using $\vec{\tau}_{svd}$ in an idealized quasi-geostrophic regional model of the Southern Ocean leads to an increase of eastward transport associated with the ACC of approximately 25%.

Horizontally and temporally averaged mesoscale EKE at the surface is reduced by 17.0 % or 24.5 % for the CLIM- and ERA40-experiments respectively (Table 3.4). The strongest EKE is found along the path of the ACC, in the Agulhas retroflection zone south of South Africa, and in the Malvinas Confluence Zone east of South America (Figure 3.6a and b). The largest SVD induced reduction of EKE is associated with strong EKE along the path of the ACC (Figure 3.6c).

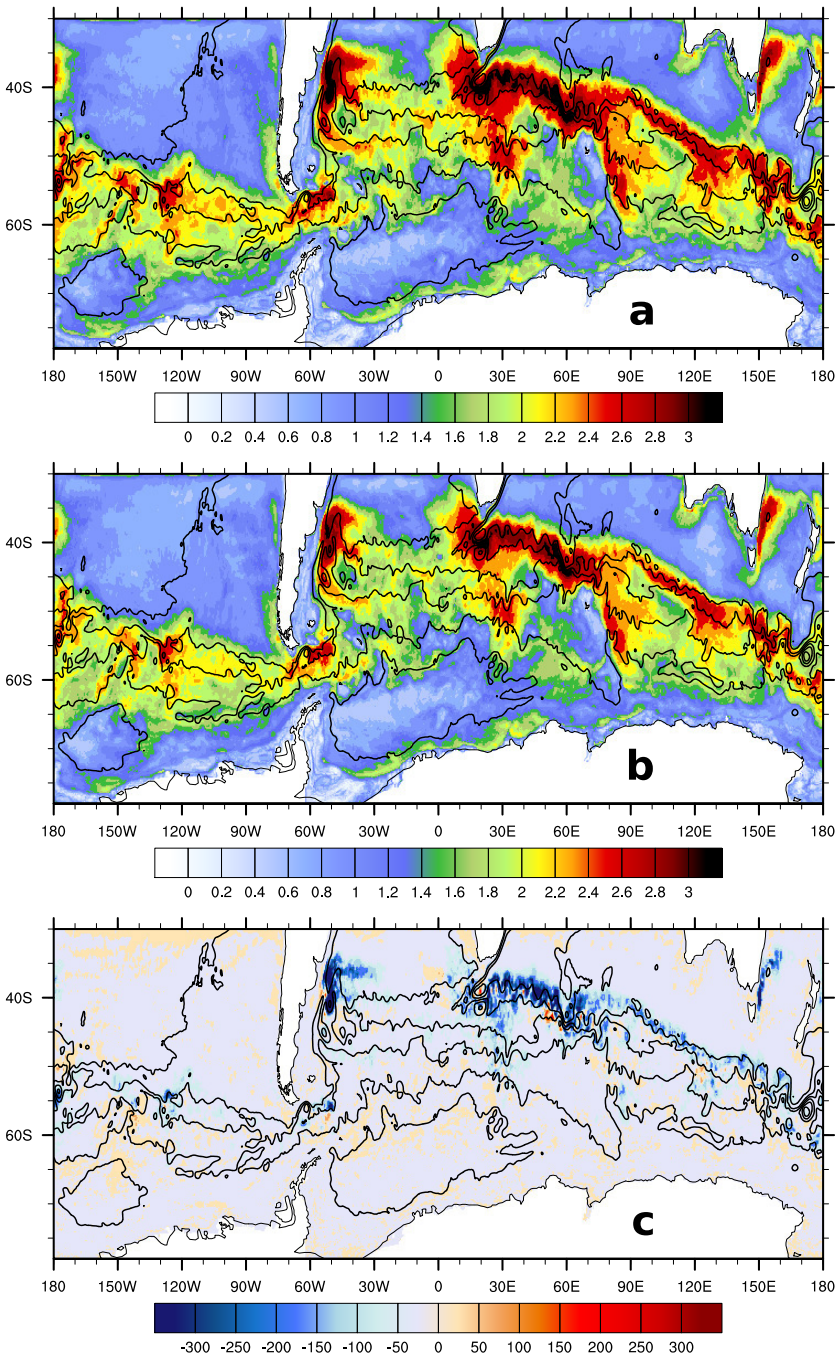

Figure 3.6: *(a)* $\log_{10}$ *of time-averaged monthly-mean based surface EKE in* $\mathrm{cm}^2/\mathrm{s}^2$ *for the experiment ERA40-CTRL. (b) Same as (a) for the experiment ERA40-SVD. (c) Difference (b) minus (a) on a linear scale in* $\mathrm{cm}^2/\mathrm{s}^2$*. Contours show the time-averaged barotropic stream function for the experiment ERA40-CTRL using a* 40 Sv *interval.*

Experiment	$\langle\overline{EKE}\rangle$	$STD_{det,ann}$	STD_{det}
ERA40-CTRL	95.1	1.88	4.06
ERA40-SVD	71.8	1.40	2.97
Δ_r	$-24.5\,\%$	$-25.4\,\%$	$-26.8\,\%$
CLIM-CTRL	101.4	1.51	4.16
CLIM-SVD	84.1	1.45	3.00
Δ_r	$-17.0\,\%$	$-3.5\,\%$	$-27.9\,\%$

Table 3.4: *$\langle\overline{EKE}\rangle$ denotes the temporal mean of the monthly-mean-based EKE at the surface. $STD_{det,ann}$ denotes the temporal standard deviation of the detrended annual-mean EKE at the surface. STD_{det} denotes the temporal standard deviation of detrended monthly-mean EKE at the surface. Δ_r denotes the relative difference defined as (SVD-CTRL)/CTRL. All numbers except for Δ_r are given in* $\mathrm{cm}^2/\mathrm{s}^2$*. All temporal means are taken for the years 1982 to 2001 and hence neglect the adjustment to the surface-velocity-dependent wind stress in the first two years of the model runs.*

3.3.3 Response of the Variability

The annual cycle of the wind stress and WPI is characterized by a broad maximum in austral winter (Figure 3.7a and b). Inter-annually, the signature of the Southern Annular Mode (SAM) (*Thompson and Wallace*, 2000; *Visbeck*, 2009) dominates the variability (Figure 3.7c to e). Using $\vec{\tau}_{svd}$ does not alter the time-dependence of the wind-forcing. The basin-averaged annual-mean wind stress and WPI of the experiments ERA40-CTRL and ERA40-SVD are highly correlated (Figure 3.7a and b).

Using $\vec{\tau}_{svd}$ damps the variability of horizontally averaged wind-stress on all time scales. The amplitude of the seasonal cycle, the amplitude of the monthly anomalies, and the amplitude of annual averages of the wind stress are all reduced (Table 3.1 and Figure 3.8a and b). The same is true for monthly-mean based WPI (Table 3.2 and Figure 3.8c and d). We find the reduction of the wind-stress variance and of the WPI variance to be biggest between approximately $65°S$ and $35°S$ (Figure 3.8).

DPT is subject to drift (Figure 3.9a, b,e and f) which is due to the lack of proper formation of Antarctic Bottom Water in the model (*Treguier et al.*, 2010). The drift causes DPT to decrease by approximately 2.7 Sv per

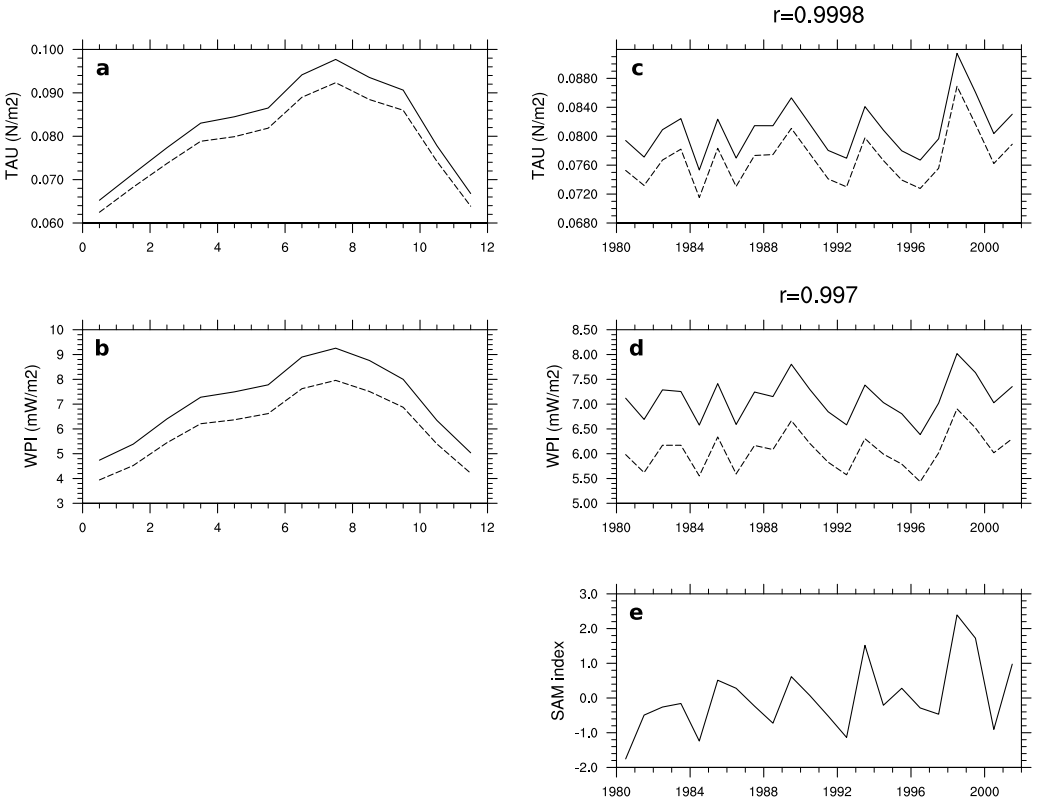

Figure 3.7: *(a) Horizontally averaged annual cycle of $|\vec{\tau}|$ for the experiment ERA40-CTRL (solid) and ERA40-SVD (dashed). (b) Horizontally averaged annual cycle of monthly-mean-based WPI for the experiment ERA40-CTRL (solid) and ERA40-SVD (dashed). (c) Annually and horizontally averaged $|\vec{\tau}|$ for the experiment ERA40-CTRL (solid) and ERA40-SVD (dashed). The correlation coefficient is $r = 1.0$. (d) Annually and horizontally averaged monthly-mean-based WPI for the experiment ERA40-CTRL (solid) and ERA40-SVD (dashed). The correlation coefficient is $r = 1.0$. (e) Annual mean SAM index from Visbeck (2009). The correlation coefficient between the SAM index shown in (e) and the time-series of basin-averaged wind stress shown in (c) is $r = 0.8$. The correlation coefficient between the SAM index shown in (e) and the time-series of basin-averaged WPI shown in (d) is $r = 0.7$. The SAM index has been normalized to mean 0 and standard deviation 1 for the years 1980 to 2001.*

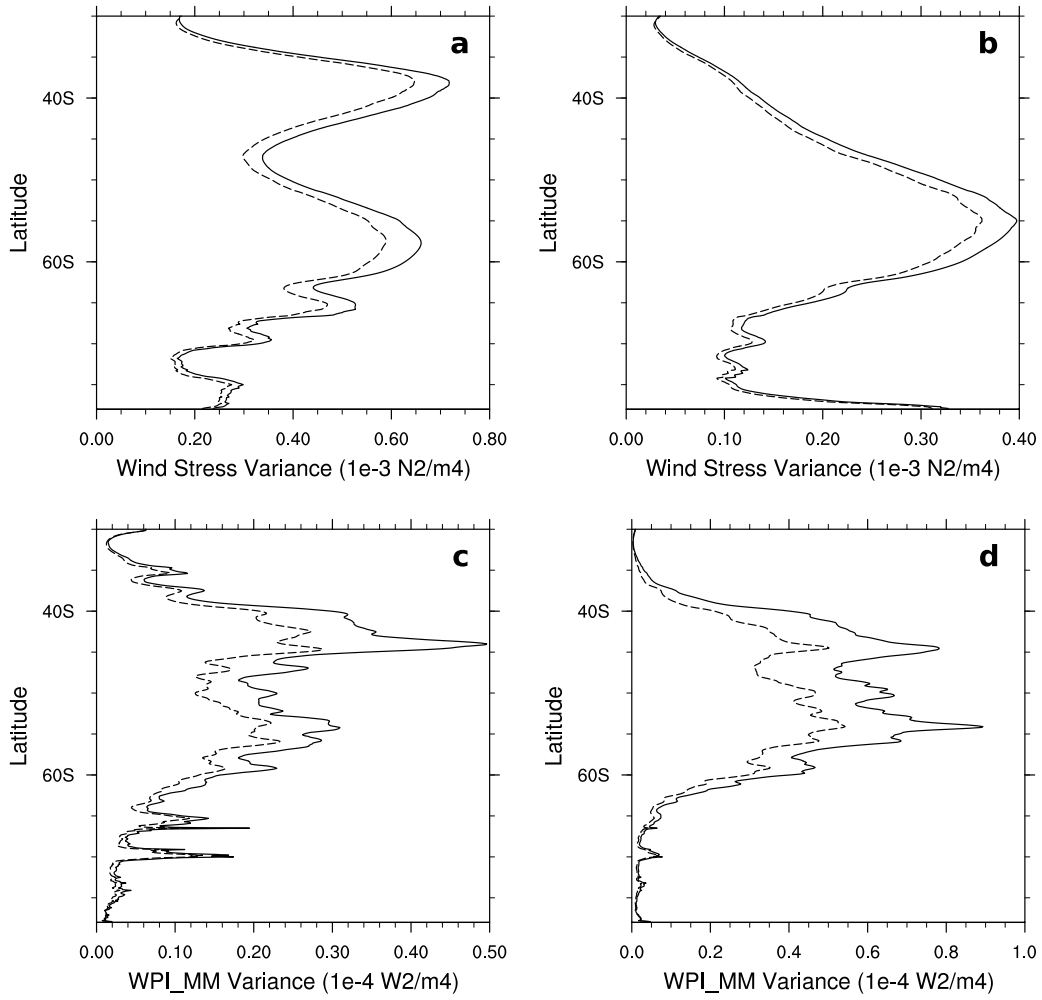

Figure 3.8: *(a) Zonally averaged variance of the wind stress magnitude* $|\vec{\tau}|$ *(in* $10^{-3}\mathrm{N}^2/\mathrm{m}^4$*) for the annual cycle. (b) Same as (a) for the annual means. (c) Zonally averaged variance of WPI (in* $10^{-4}\mathrm{W}^2/\mathrm{m}^4$*) for the annual cycle. (d) Same as (c) for the annual means. Solid lines represent the experiment ERA40-CTRL and dashed lines represent the experiment ERA40-SVD.*

decade (for ERA40-CTRL). Earlier studies noted that there is significant inter-annual variability of DPT in eddying models of the Southern Ocean even if there is no inter-annual variability in the forcing that drives the model (*Treguier et al.*, 2010; *Munday et al.*, 2013). We also find that in the CLIM-experiments, which are driven by repeated-year forcing, there is significant variability of DPT, both on inter-annual and on monthly time-scales (Table 3.3 and Figure 3.9c and g). The DPT time series from CLIM-CTRL and CLIM-SVD, however, are not significantly correlated (Figure 3.9c and g). This indicates importance of chaotic internal ocean dynamics (eddies) that drive the variability.

Nevertheless, the wind-forcing has been shown to determine a significant part of the interannual variability of DPT (*Hughes et al.*, 1999; *Treguier et al.*, 2010; *Zika et al.*, 2013) as can be seen by noting the larger amplitude of variability in those experiments that include variable wind forcing other than the seasonal cycle (Table 3.3). Furthermore, the DPT time series from the ERA40-experiments are highly correlated on monthly (correlation coefficient $r = 0.68$) and inter-annual ($r = 0.80$) time scales (Figure 3.9d and h). When the wind stress is parameterized using $\vec{\tau}_{svd}$, the amplitudes of monthly and inter-annual variability of DPT from the ERA40-experiments are reduced by 7.3 % and 13.5 % respectively (Table 3.3). The amplitudes of the monthly and inter-annual variability of DPT from the climatologically forced experiments are not reduced.

EKE shows a marked downward trend (Figure 3.10), which is consistent with the downward trend of DPT (*Treguier et al.*, 2010). All four experiments start from the same initial condition on 1980-01-01. After switching to SVD, EKE of the experiments CLIM-SVD and ERA40-SVD adjusts to lower values within two years and then follows a largely linear trend (Figure 3.10). We do not find a significant correlation between the EKE time series of the realistically forced experiments ERA40-CTRL and ERA40-SVD. This is consistent with *Treguier et al.* (2010) who find that EKE across model runs with identical forcing fields but different initial conditions was uncorrelated, and who concluded that on monthly and interannual timescales EKE is not deterministic. Using SVD damps the amplitude of horizontally averaged EKE

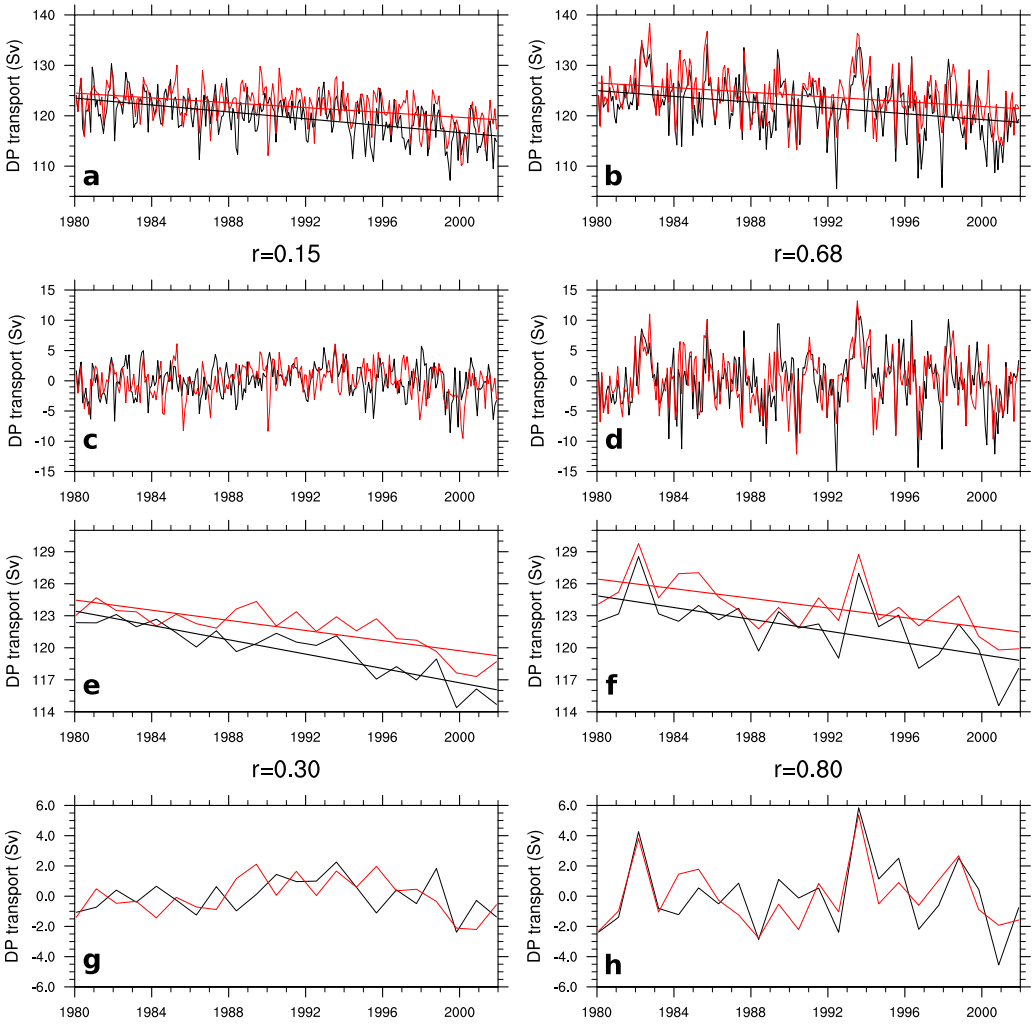

Figure 3.9: *(a) Monthly mean DPT (Sv) for CLIM-CTRL (black) and CLIM-SVD (red). The straight lines show the linear trends. (b) Same as (a) for the ERA40 experiments. (c) Monthly mean DPT (Sv), detrended and with the annual cycle removed, for CLIM-CTRL (black) and for CLIM-SVD (red). The correlation coefficient is* $r = 0.15$. *(d) Same as (c) for the ERA40 experiments. The correlation coefficient is* $r = 0.68$. *(e) Annual mean DPT (Sv) for CLIM-CTRL (black) and CLIM-SVD (red). The straight lines show the linear trends. (f) Same as (e) for the ERA40 experiments. The correlation coefficient is* $r = 0.68$. *(g) Annual mean DPT (Sv), detrended, for CLIM-CTRL (black) and for CLIM-SVD (red). The correlation coefficient is* $r = 0.30$. *(h) Same as (g) for the ERA40 experiments. The correlation coefficient is* $r = 0.80$.

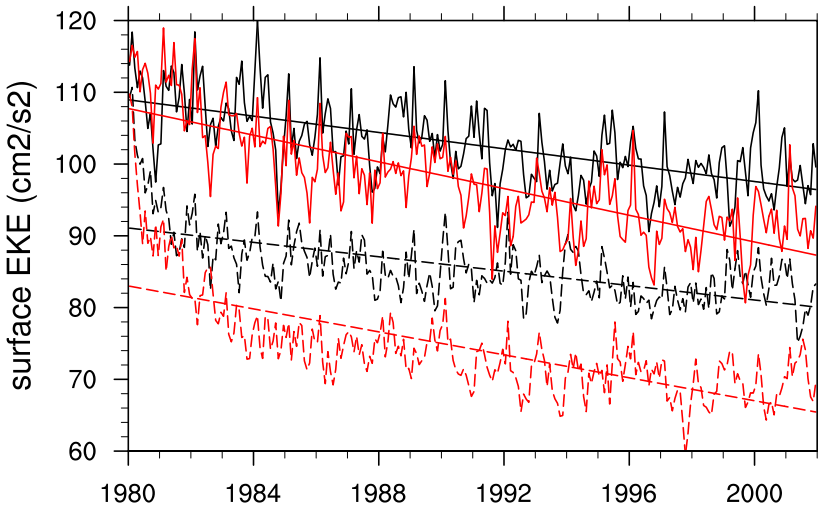

Figure 3.10: *Horizontally averaged surface EKE in* $\mathrm{cm}^2/\mathrm{s}^2$ *for the experiment CLIM-CTRL (black solid), CLIM-SVD (black dashed), ERA40-CTRL (red solid), and ERA40-SVD (red dashed) together with the respective linear trends calculated for the years 1982 to 2001.*

on monthly and on inter-annual time scales (Table 3.4).

3.4 Summary and Discussion

Including the ocean-surface velocity into the parameterization of the wind stress has been shown to substantially reduce WPI into the geostrophic circulation (*Duhaut and Straub*, 2006; *Hughes and Wilson*, 2008; *Xu and Scott*, 2008), and to substantially reduce mesoscale EKE (*Zhai and Greatbatch*, 2007). Using a realistic primitive equation model, we have confirmed, that SVD leads to a reduction of time-averaged WPI by up to 14.9 %, and of time-averaged mesoscale EKE by up to 25.5 %. The largest reduction of WPI is found where the westerly winds align with the eastward surface flow associated to the ACC. The largest reduction of EKE is associated with the strong mesoscale eddy field along the path of the ACC.

Compared to the large effect of SVD on WPI and EKE, we find that the response of the ACC to SVD is relatively weak. SVD does not alter the position of the ACC fronts, which carry the bulk of the eastward transport,

and which are thought to be controlled by topography (*Orsi et al.*, 1995; *Hughes and Ash*, 2001). DPT is increased by 1.8 % if SVD is used. This contradicts the findings of *Hutchinson et al.* (2010), who find that SVD in an idealized quasi-geostrophic model, leads to an increase in eastward transport as big as 25 %.

SVD is found to reduce the inter-annual variability of the wind-forcing, of EKE, and of DPT. At the same time, the time-dependence of basin-averaged wind stress, WPI, and of DPT with SVD were found to be highly correlated to those without SVD.

Chapter 4

On the Spatial and Temporal Distribution of Near-Inertial Energy in the Southern Ocean

Willi Rath, Richard J. Greatbatch, Xiaoming Zhai[1]

Abstract: We use an eddying realistic primitive equation model of the Southern Ocean to examine the spatial and temporal distribution of near-inertial wind power input (WPI) and near-inertial energy (NIE) in the Southern Ocean. We show that near-inertial WPI is almost proportional to inertial wind-stress variance (IWSV), while NIE is modulated by the inverse of the mixed-layer depth. We use this close relationship to asses recent decadal trends of near-inertial WPI from trends of IWSV based on reanalysis wind-stress. Averaged over the Southern Ocean, annual-mean IWSV is found to have increased by 16 percent over the years 1979 through 2011. Part of the increase of IWSV is found to be related to a positive trend of the Southern Annular Mode in the same period. Furthermore, we show that there are horizontal local maxima of NIE at depth that are almost exclusively associated with anticyclonic eddies.

[1]This chapter is under review for the *Journal of Geophysical Research - Oceans*.

4.1 Introduction

Near-inertial waves (NIW) play a key role in the global climate system. By deepening the oceanic mixed layer (*Pollard et al.*, 1972), they influence the global sea-surface temperature (SST) and especially in the tropics, by teleconnections, potentially have a global impact on the atmospheric circulation (*Jochum et al.*, 2013). The contribution of wind-generated NIWs to the energy available for mixing at depth, which is thought to drive the global overturning circulation (*Munk and Wunsch*, 1998), is a matter of debate. Model-based estimates of global near-inertial wind power input (WPI) are of the order of 0.5 TW (*Watanabe and Hibiya*, 2002; *Alford*, 2003; *Furuichi et al.*, 2008) with large uncertainties stemming from a high sensitivity to the spatial and temporal resolution of the wind stress used to force the model (*Jiang et al.*, 2005), from missing physics in the simple models (*Plueddemann and Farrar*, 2006) and from the wind-stress parameterization (*Rath et al.*, 2013a). Direct global observational estimates of NIWs are restricted to the surface (*Chaigneau et al.*, 2008; *Elipot and Lumpkin*, 2008), and observations of NIWs at depth are only available at a limited number of locations (*Pollard and Millard*, 1970; *D'Asaro*, 1985; *Alford*, 2003; *Plueddemann and Farrar*, 2006).

Recent modelling studies show that the majority of the wind-induced near-inertial energy (NIE) is dissipated within the surface mixed layer, and estimate only approximately 20 % of the NIE injected at the surface is able to escape the mixed layer and contribute to mixing in the ocean interior (*Furuichi et al.*, 2008; *Zhai et al.*, 2009). Anticyclonic eddies are known to trap NIWs (*Kunze*, 1985; *Zhai et al.*, 2005), and provide a possible pathway to the interior ocean (*Zhai et al.*, 2007; *Jing et al.*, 2011). However, the relevance of anticyclonic eddies for determining the fraction of NIE available for mixing at depth, has yet to be quantified.

In this study, we use a realistic primitive equation model at eddying spatial resolution to examine the spatial and temporal distribution of near-inertial WPI and NIE in the Southern Ocean. After describing details on the model and the data in Section 4.2, we present our results for the large-scale

spatial and vertical distribution of near-inertial WPI and NIE, and assess the relevance of enhanced NIE in anticyclonic eddies in Section 4.3. We proceed to the annual cycle in Section 4.4. Section 4.5 highlights the relation of inertial wind-stress variance (IWSV) to near-inertial WPI and NIE in the mixed-layer. In Section 4.6, we assess recent decadal trends of IWSV and use the relationship to near-inertial WPI to assess the implications for NIWs in the ocean. We close with a summary in Section 4.7.

4.2 Methods, Models and Data

4.2.1 Primitive-Equation Model

We use an eddying $(1/10)^\circ$ primitive-equation ocean model with realistic topography which is identical to the one described in *Rath et al.* (2013a). It covers all the Southern Ocean south of $30^\circ S$. The model is driven by realistic wind stress derived from six-hourly wind fields using the surface-velocity-dependent parameterization described by *Duhaut and Straub* (2006) and *Rath et al.* (2013a)

$$\vec{\tau}_{SVD} \equiv \rho_a c_d(|\vec{U}_{10} - \vec{u}_o|)|\vec{U}_{10} - \vec{u}_o|(\vec{U}_{10} - \vec{u}_o) \ , \tag{4.1}$$

where ρ_a is the density of air close to the sea surface, $c_d(U)$ is the drag-coefficient that depends on the relative speed of the wind and the ocean-surface velocity, $\vec{u}_o$ is the surface velocity, and $\vec{U}_{10}$ is 10-meter wind from the ERA40 reanalysis (*Uppala et al.*, 2005). Surface-heat flux is prescribed using a climatology (*Barnier et al.*, 1995). Surface salinity is restored to climatological values with a time scale of 15 days for the upper level of thickness $10\,m$. Vertical mixing is parameterized using the TKE-mixing scheme as described by *Gaspar et al.* (1990) and *Blanke and Delecluse* (1993), and horizontal mixing is parameterized in both the momentum and tracer equation using a biharmonic diffusivity.

The model is spun up for 31 years from a state of rest and hydrography specified from climatology. The first 10 years of the spin-up are driven by

climatological wind stress that depends on the 10-meter wind alone

$$\vec{\tau}_{CTL} \equiv \rho_a c_d(|\vec{U}_{10}|)|\vec{U}_{10}|\vec{U}_{10} \tag{4.2}$$

and the following 21 years of the spin-up are driven by 6-hourly ERA40-based wind stress parameterized according to (4.2). The model shows a realistic Antarctic Circumpolar Current (ACC), and a realistic mesoscale eddy field (see *Rath et al.* (2013a) for details).

After the spin-up, and starting on January 1, 2001, the wind-stress parameterization is changed to include the ocean-surface velocity according to (4.1). Note that we start the analysis of the model output immediately after changing the wind-stress parameterization to surface-velocity dependent and that, consequently, the adjustment of the model to the new wind-stress parameterization is contained in the data we present here. *Rath et al.* (2013a) showed that surface-velocity-dependent wind stress acts to significantly reduce NIE in the mixed layer as well as at depth and that this reduction spreads from the surface to depth within approximately a month. Hence, we expect that during the first month of the model output presented here, NIE especially at depth is overestimated. The focus of this study, however, is on near-inertial WPI and on mixed-layer NIE, which adjust to surface-velocity-dependent wind stress on timescales much shorter than a month.

The first 36.5 days of the model output for the year 2001 are available at the full spatial resolution of the model ($1/10^\circ \times 1/10^\circ$) and at a temporal resolution of 3 hours. For the rest of the year 2001, the spatial resolution of the model output was reduced to $1^\circ \times 1^\circ$ without changing the temporal resolution. By comparing the full-resolution output for the first 36.5 days to the reduced-resolution output over the same period, it was confirmed that near-inertial WPI and NIE at the reduced spatial resolution contains all the information that is relevant for this study. Apart from the discussion of the effect of anticyclonic eddies in Section 4.3.1, all the analysis presented here is based on the reduced-resolution output.

4.2.2 Near-Inertial Quantities

We separate the velocity field into the sub-inertial, the near-inertial, and the super-inertial frequency band. The subscript I indicates near-inertial quantities, and the subscripts S and T indicate sub-inertial and super-inertial quantities respectively. In the actual calculations, the separation into the three frequency bands was realized using a fifth-order Butterworth filter as described in *Rath et al.* (2013a).

We define near-inertial energy (NIE) as

$$E_I \equiv \rho_0 \frac{\vec{u}_I \cdot \vec{u}_I}{2} \ , \tag{4.3}$$

the mixed-layer NIE as the integral

$$\int_0^H E_I(z)\,\mathrm{d}z \tag{4.4}$$

where H is the mixed-layer depth (see Section 4.2.5), and near-inertial WPI

$$WPI_I \equiv \vec{\tau} \cdot \vec{u}_I(z=0) \ . \tag{4.5}$$

4.2.3 Simplified Models for Near-Inertial Wind Power Input and Near-Inertial Energy

Pollard and Millard (1970) proposed a local linear slab-ocean model for near-inertial oscillations (PM70) which has since been widely used to assess the input of near-inertial energy into the surface-mixed layer of the ocean (see, e.g., *Alford* (2003)). It is a local model for the near-inertial velocity in the mixed layer (u, v), which is assumed to be vertically uniform. It features the Coriolis force $f(-v, u)$, the wind stress $\vec{\tau} = (\tau^x, \tau^y)$, a linear damping term with the coefficient ϵ, the mixed-layer depth H (assumed to be time-

independent), and the reference density ρ_0:

$$u_t - fv = \frac{\tau^x}{\rho_0 H} - \epsilon u \tag{4.6}$$

$$v_t + fu = \frac{\tau^y}{\rho_0 H} - \epsilon v \tag{4.7}$$

The time-evolution of kinetic energy, $E = \vec{u} \cdot \vec{u}/2$, in PM70 is governed by

$$E_t = uu_t + vv_t = \frac{1}{\rho_0 H}(\tau^x u + \tau^y v) - \epsilon(u^2 + v^2) \tag{4.8}$$

With given mixed-layer depth H, ϵ is the only free parameter of the model. It is usually tuned to minimize the difference between modelled currents, the modelled near-inertial WPI or the modelled NIE and observations. Typically, tuned $1/\epsilon$ is found to be in the range of 2 to 10 days (see, e.g., *Pollard and Millard* (1970) or *D'Asaro* (1985)).

In Section 4.5.1, the ratio of time-averaged NIE and near-inertial WPI will be examined. In PM70, a relation between time-averaged NIE and near-inertial WPI can be obtained by setting E_t to zero in (4.8) and by using (4.5). This leads to

$$\frac{E_I}{WPI_I} = \frac{1}{2\rho_0 \epsilon H} \propto \frac{1}{H} \tag{4.9}$$

and to

$$\frac{E_I \cdot H}{WPI_I} = \frac{1}{2\rho_0 \epsilon} \ . \tag{4.10}$$

Plueddemann and Farrar (2006) examine the performance of PM70 and of a mixed-layer model (PWP) similar to the one described by *Price et al.* (1986) that features a vertically uniform slab on top of a transition zone where free convective mixing, mixed-layer entrainment and shear-instability can alter the mixed-layer depth. *Plueddemann and Farrar* (2006) added a linear damping term mimicking the radiation of NIWs away from the mixed-layer which acts on similar timescales as the linear-damping term of PM70. In PWP, mixed-layer entrainment and mixing driven by shear-instability is parameterized using two different Richardson number criteria, both relating stratification to velocity shear at the base of the mixed layer. Compar-

ing PM70 and PWP model results to observed near-inertial currents from mooring sites, *Plueddemann and Farrar* (2006) found PM70 to be unable to reproduce the observed near-inertial WPI and NIE at the same time, because it lacked an energy sink acting on time scales shorter than those associated to ϵ. PWP, on the other hand, correctly captured the observed energy balance on all time scales.

4.2.4 Regions and Seasons

We separate the model domain into four regions shown, e.g., as white boxes in Figures 4.1.

- **R01:** $x \in (190°E, 270°E)$ and $y \in (50°S, 35°S)$
- **R02:** $x \in (190°E, 270°E)$ and $y \in (65°S, 50°S)$
- **R03:** $x \in (315°E, 010°E)$ and $y \in (50°S, 35°S)$
- **R04:** $x \in (010°E, 145°E)$ and $y \in (60°S, 40°S)$

The regions were chosen to take account of the large spatial differences of the mixed-layer depth (see Figure 4.2d and Figure 4.3).

For the seasons, we use the oceanographic convention with boreal winter / austral summer comprising the months January to March (JFM), boreal spring / austral fall comprising April to June (AMJ), boreal summer / austral winter comprising the months July to September (JAS), and boreal fall / austral spring comprising the months October to December (OND).

4.2.5 Mixed-Layer Depth

The vertical distribution of NIE is separated into high levels of NIE that are confined to a surface layer and into lower levels of NIE below. The depth of this surface layer is often approximated by the mixed-layer depth derived from hydrographic criteria (*de Boyer Montegut et al.* (2004) list various criteria used in the literature). If not stated otherwise, we will use the depth

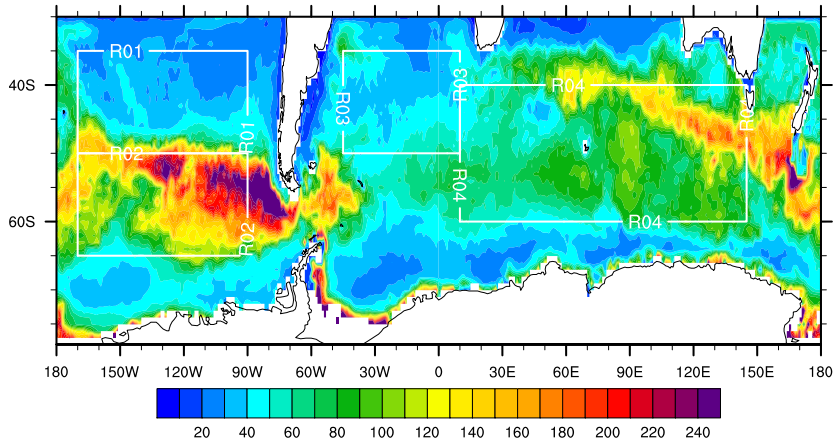

Figure 4.1: *2001 time-averaged mixed-layer depth H (*m*) diagnosed from the primitive-equation-model potential density σ_0 as discussed in the text. Also shown are the regions R01, R02, R03 and R04 referred to in the text.*

H at which the monthly mean potential density σ_0 first exceeds the value at the surface by $0.03\,\mathrm{kg/m^3}$.

In the Southern Ocean, a deep mixed-layer along the path of the ACC (reaching more than 300 m in the annual average) is flanked by a shallower mixed-layer (up to 50 m in the north and up to 100 m in the south). The modelled annual mean mixed-layer depth shown in Figure 4.1 broadly agrees with the climatological estimate provided by *de Boyer Montegut et al.* (2004) (not shown). Depending on the region, the austral winter mixed-layer depth can be more than ten times deeper than the austral summer mixed-layer depth (see Figure 4.2d which is discussed later).

4.2.6 Inertial Wind-Stress Variance – IWSV

We define the inertial wind-stress variance

$$IWSV \equiv |(\tilde{\tau}_I^x)^2 + (\tilde{\tau}_I^y)^2| \tag{4.11}$$

where $\tilde{\tau}_I^x$ and $\tilde{\tau}_I^y$ are the Fourier transforms of the wind-stress components τ^x and τ^y at the (latitude-dependent) inertial frequency. We calculate monthly values for IWSV by calculating the Fourier transforms $\tilde{\tau}_I^x$ and $\tilde{\tau}_I^y$ based on

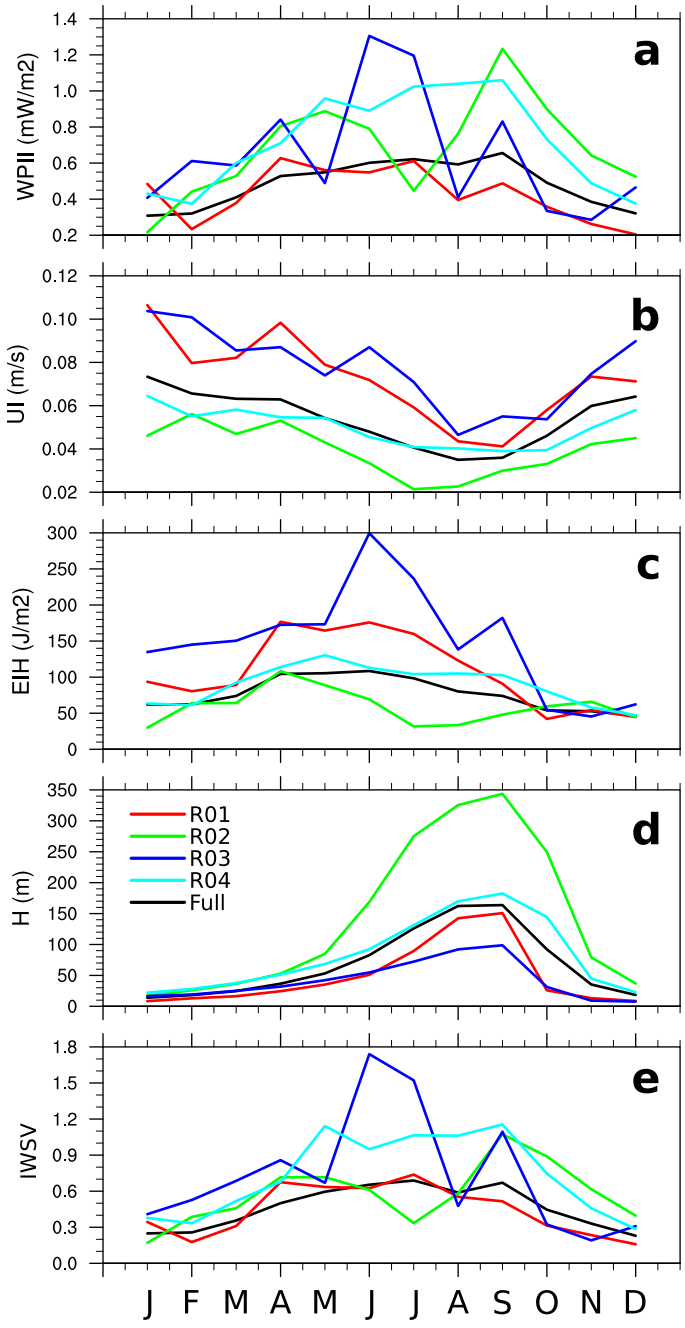

Figure 4.2: *Monthly means of horizontal averages of, (a), near-inertial WPI* (mW/m2)*, (b), amplitude of the near-inertial velocity at the surface* (m/s)*, (c), mixed-layer NIE* (J/m^2)*, (d), the mixed-layer depth* (m)*, and, (e), the inertial wind-stress variance, IWSV, for the regions R01 (red lines), R02 (green lines), R03 (blue lines), R04 (cyan lines), and for the full model domain (black lines).*

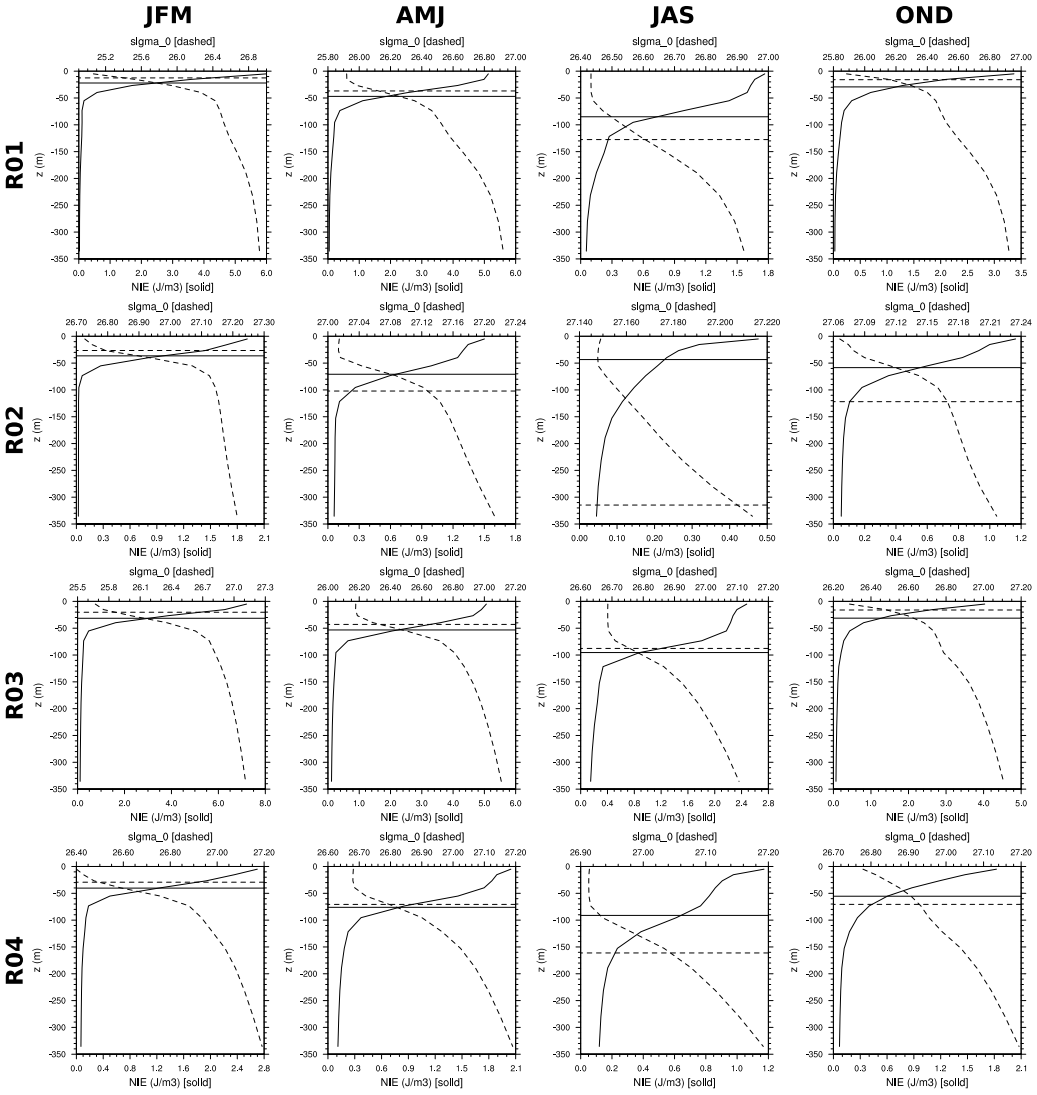

Figure 4.3: *Horizontal averages of NIE (solid lines), and potential density referenced to the surface σ_0 (dashed lines) over the top* 350 m *of the water column together with horizontal averages of the penetration depth of NIE, $H_{E_{0.5}}$, (horizontal solid lines), and of the mixed-layer depth, H, (horizontal dashed lines). The horizontal averages have been calculated for the regions R01 to R04 (from top to bottom) and for the seasons JFM to OND (from left to right). Note that the scales differ for each panel.*

6-hourly wind stress separately for each month. We tried different proxies for the wind-stress variability on inertial time-scales and found the results of this study to be hardly affected. We will give IWSV in arbitrary units that are, however, consistent throughout this study.

4.2.7 Choosing the Wind-Product

Figure 4.4 compares the annually and zonally averaged variances of zonal 10-m wind on time scales shorter than five days (UVAR5) for ERA40 and for ERA-Interim. UVAR5 for the pre-satellite era (before 1979) is significantly lower than UVAR5 later on. There is a notable decrease of UVAR5 for the years 1973 to 1978 of ERA40. UVAR5 from ERA-Interim is higher than UVAR5 from ERA40 in the years present in both products. The spatial and temporal variability of UVAR5 in ERA-Interim and ERA40, however, broadly agrees. The spatial resolution of the ERA-Interim fields is approximately $0.7^\circ \times 0.7^\circ$ and the spatial resolution of the ERA-40 fields is approximately $1.2^\circ \times 1.2^\circ$. We attribute the higher UVAR5 of ERA-Interim to the higher spatial resolution of the ERA-Interim wind fields (see also *Jiang et al.* (2005)).

4.2.8 Southern-Annular Mode

We calculate the Southern-Annular-Mode index (SAM) using an ad-hoc definition (*Gong and Wang*, 1999) based on the difference of monthly-mean zonally averaged sea-level pressure (SLP) at $65^\circ S$ and at $40^\circ S$. The annual-mean SAM index is obtained by annually averaging the monthly SAM index. There is broad agreement with the station-based SAM index presented by *Visbeck* (2009) (Figure 4.5a). The regression of the zonal 10-m-wind anomalies onto the annual-mean SAM index (Figure 4.5b) is dominated by a largely zonal pattern of positive wind anomalies between $65^\circ S$ and $45^\circ S$.

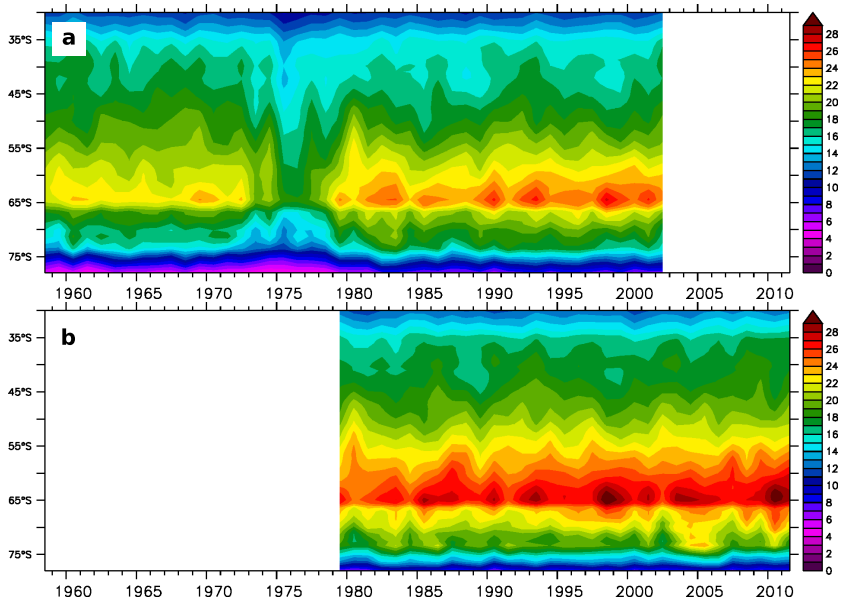

Figure 4.4: *Annual and zonal averages of UVAR5 in* m^2/s^2 *(see text) for (a) ERA40 and (b) ERA-Interim.*

4.3 Spatial Distribution of Near-Inertial Wind Power Input and Near-Inertial Energy

4.3.1 Horizontal Distribution

The large-scale spatial patterns of time-averaged near-inertial WPI and of mixed-layer NIE for the whole year 2001 are generally different (Figure 4.6). While near-inertial WPI is dominated by a largely zonal structure with meridional maxima between $65°S$ and $40°S$, high levels of mixed-layer NIE are mainly found north of $55°S$. Figure 4.7 shows the 2001 seasonal averages (JFM etc.) of near-inertial WPI and mixed-layer NIE. As for the whole-year average, seasonally averaged near-inertial WPI shows a banded structure following the southern hemisphere storm track with smaller local maxima that are often less than 5° in diameter. The spatial distribution of seasonally averaged mixed-layer NIE, on the other hand, is more obviously characterized by structures less than 5° in diameter. Again, the zonal structure of near-

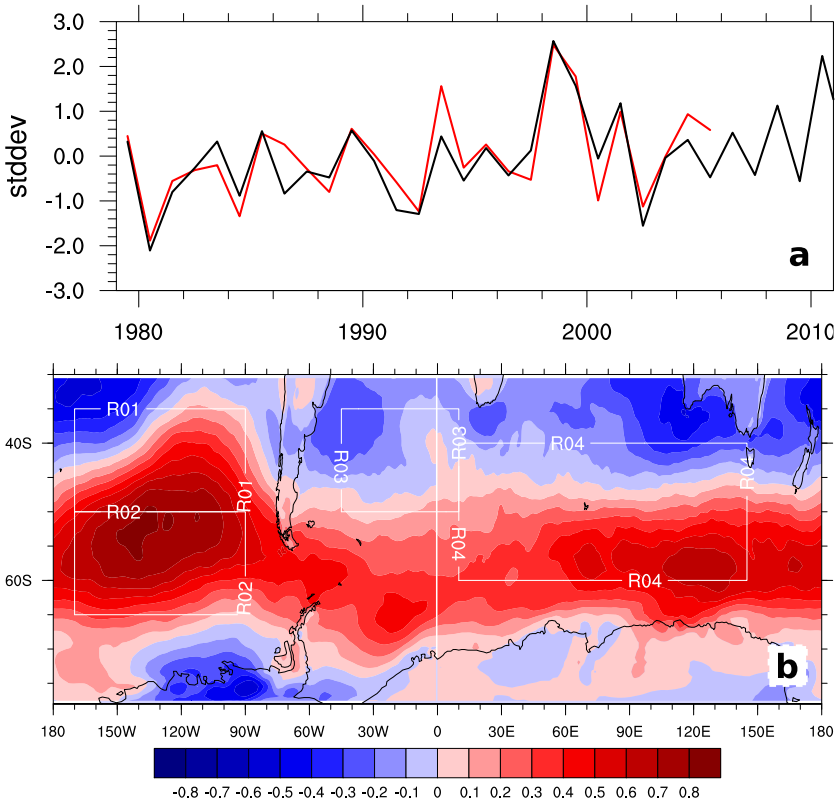

Figure 4.5: *(a) Annual-mean SAM index calculated from ERA-Interim (black line) and from Visbeck (2009) (red line). (b) SAM-related annual-mean zonal wind pattern* (m/s).

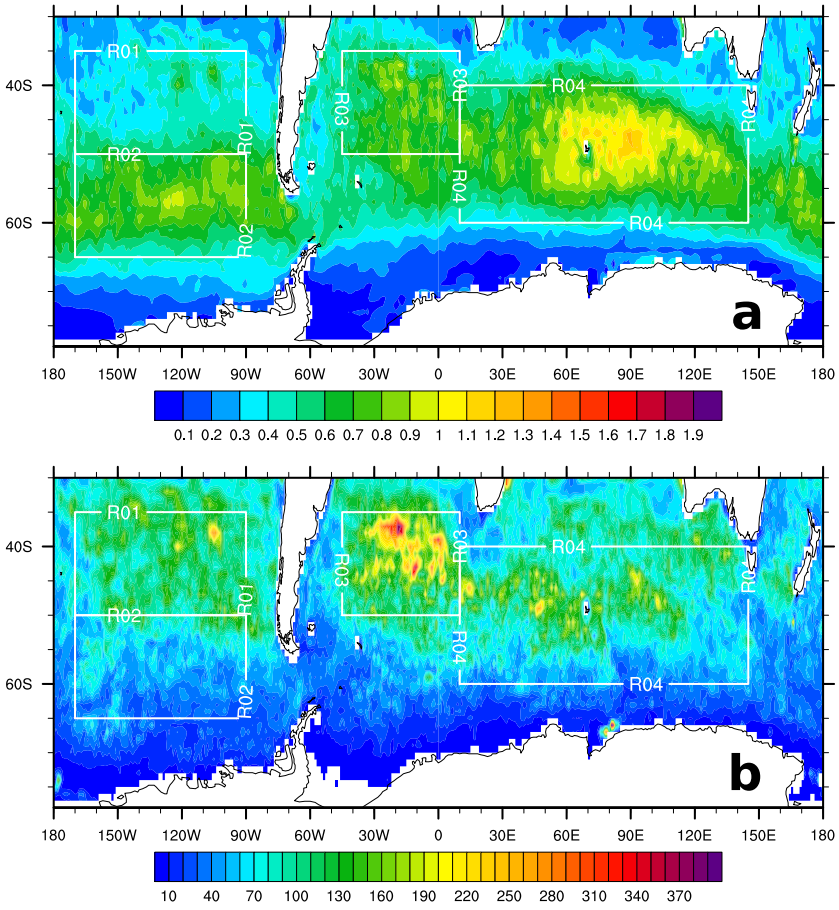

Figure 4.6: *Year 2001 time averages of (a) near-inertial WPI* (mW/m^2) *and (b) mixed-layer NIE* (J/m^2).

inertial WPI is not reflected by the mixed-layer NIE, but on spatial scales of a few degrees, local maxima of mixed-layer NIE often agree with local maxima of near-inertial WPI. However, there are strong maxima in near-inertial WPI that are not associated with high mixed-layer NIE.

While in region R01, R03, and R04 (see Section 4.2.4 and Figure 4.1) high near-inertial WPI leads to high levels of mixed-layer NIE, there is a discrepancy between near-inertial WPI and mixed-layer NIE in R02 which covers the Pacific sector of the ACC. In R02, even when near-inertial WPI is large compared to the spatial average over the whole model domain, mixed-layer NIE levels remain low. This difference is most pronounced in austral winter (JAS), when the high near-inertial WPI in the Pacific sector of the

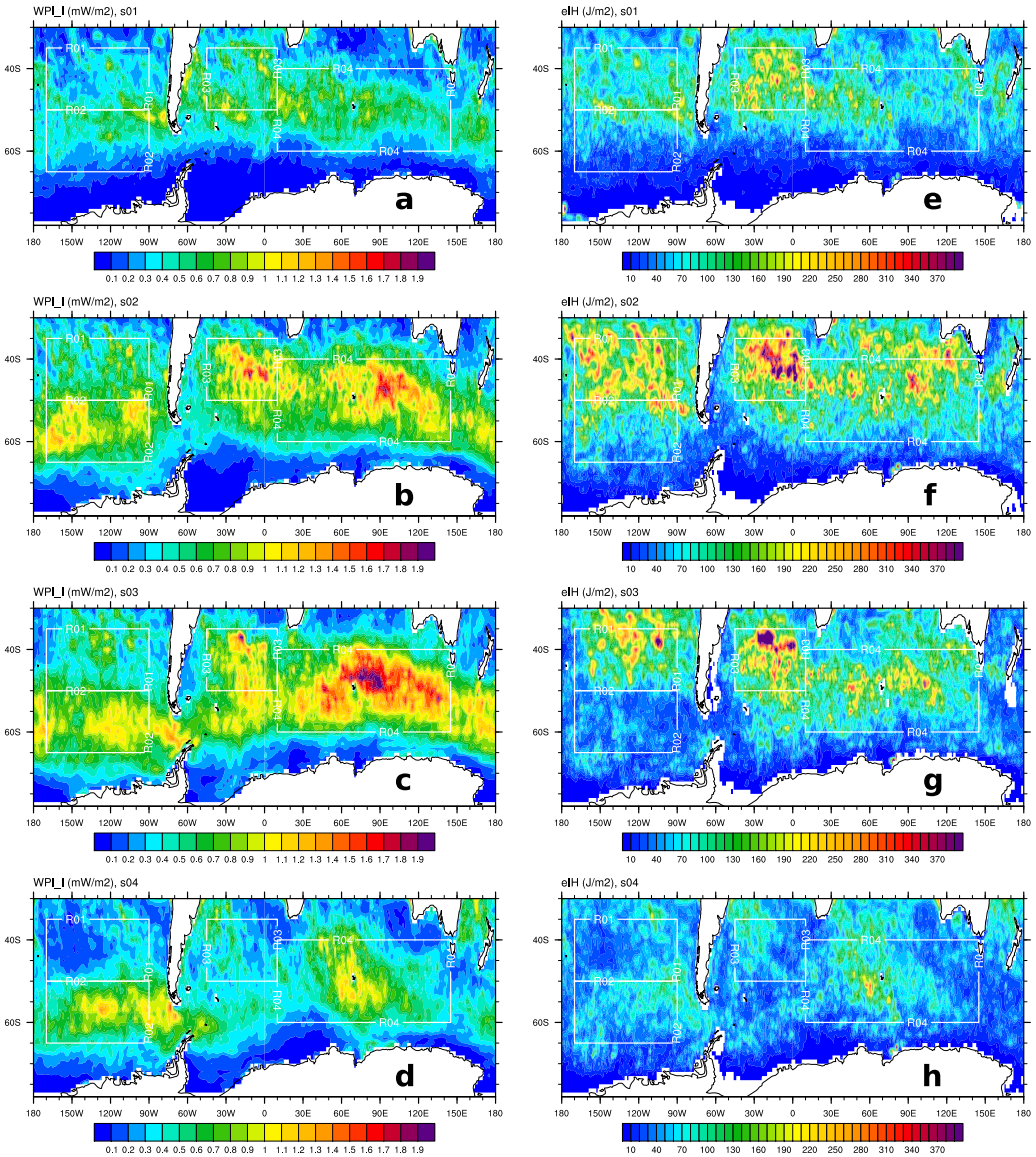

Figure 4.7: *Seasonal averages of near-inertial WPI* ($\mathrm{mW/m^2}$) *and mixed-layer NIE* ($\mathrm{J/m^2}$). *(a-d) Near-inertial WPI* ($\mathrm{mW/m^2}$) *for JFM, AMJ, JAS, OND from 2001. (e-h) Mixed-layer NIE* ($\mathrm{J/m^2}$) *for JFM, AMJ, JAS, OND from 2001.*

ACC (R02) is not reflected by the mixed-layer NIE.

4.3.2 Vertical Distribution

In the simple linear slab-ocean model of PM70 (see Section 4.2.3), the wind-stress acts as a bulk force over a surface layer that is often associated with the mixed-layer. In the surface layer, near-inertial velocities are assumed to be vertically uniform. Figure 4.3 shows the horizontal and seasonal averages of NIE, of potential density referenced to the surface (σ_0), of the mixed-layer depth defined as in Section 4.2.2, and of the penetration depth of NIE, defined as the depth at which NIE has decayed to 50 % of its value at the surface, for each of the four regions. The assumption of PM70, that NIE is concentrated in a layer close to the surface, generally holds and in fact, the values of NIE in the mixed-layer are often higher than the values of NIE below by several orders of magnitude. However, the amplitude of the near-inertial velocities within the mixed layer is not vertically uniform. On the contrary, most of the NIE in the mixed layer is concentrated near the surface and there is a decay of NIE towards the base of the mixed layer. In austral winter (JAS), NIE is concentrated much closer to the surface than the mixed-layer depth would indicate. In R02, the austral-winter NIE even penetrates less deep than in autumn and in spring.

4.3.3 Trapping in Anticyclonic Eddies

The vertical profiles of NIE shown in Figure 4.3 indicate that high levels of NIE are confined to a surface layer which often coincides with the surface mixed-layer. However, among many others, *Kunze* (1985), *Zhai et al.* (2005), and *Zhai et al.* (2007) showed that in anticyclonic eddies, there can be enhanced downward propagation of NIE. They argue that it is the effective Coriolis parameter $f + \zeta/2$, where ζ is the relative vorticity, rather than the Coriolis parameter f alone that sets the frequency at which NIWs are excited. NIWs generated inside an anticyclonic (positive ζ in the southern hemisphere) eddy are then trapped inside of the eddy because they cannot propagate into the surrounding regions where the modulus of the effective

Coriolis parameter is larger. Recent observations show further observational evidence for the trapping of NIE in anticyclonic eddies (*Jing et al.*, 2011; *Joyce et al.*, 2013).

We use the high-resolution model output from the primitive-equation model that is available for the first 36.5 days of 2001 to show that there are strong local maxima of NIE at depth associated with strong anticyclonic eddies. Local maxima of NIE at depth are scattered all over the model domain. As an example, we examine the vertical distribution of NIE along a section in the South Atlantic. Figure 4.8a shows near-inertial energy E_I, sub-inertial relative vorticity $\zeta_S = (v_S)_x - (u_S)_y$, and $E_{rel} \equiv E_I / E_{I,smoothed}$ for a section at $49.9°S$ ranging from $30°W$ to $15°W$. $E_{I,smoothed}$ denotes NIE that has been horizontally filtered with a $\pm 1^o \times \pm 2^o$ (lat×lon) Hanning window. We use E_{rel} as a measure for the ratio of local NIE to the ambient NIE and hence as a measure for the strength of local maxima of NIE. From Figure 4.8a, it is evident that regions of high NIE coincide with regions of positive ζ_S at depth. To further confirm this, Figure 4.8b shows a scatter plot of E_{rel} and ζ_S for the section shown in Figure 4.8a covering all depths up to 1000 m, and Figure 4.8d shows the same scatter plot for the whole model domain and restricted to $1000\,m$ depth. Local maxima of NIE ($E_{rel} > 1$) are almost exclusively associated with positive relative vorticity. Figure 4.8c compares horizontally and temporally averaged NIE for the whole model domain to horizontally and temporally averaged NIE for grid points where time averaged surface relative vorticity ζ_S exceeds $0.5{\cdot}10^{-5}/s$. There is a clear enhancement of NIE inside anticyclonic eddies for depths around $200\,m$ and, again, around $700\,m$ depth. The area of the surface with $\zeta_S \geq 0.5 \cdot 10^{-5}/s$ is about 9.8 % of the whole (water covered) model domain. The contribution of NIE from the same part of the model domain at depths between $300\,m$ and $1000\,m$ is about 21.3 %. We conclude that the enhancement of deep NIE in anticyclonic regions may play a significant role in providing energy that is available for mixing in the deep ocean. However, it should be remembered that the bulk of the wind induced NIE in the ocean is, nevertheless, used to increase potential energy (by deepening the mixed-layer depth) or to produce heat (by dissipation within the mixed layer) and hence is unavailable for

mixing at depth (*Furuichi et al.*, 2008; *Zhai et al.*, 2009).

4.4 Temporal Distribution of Near-Inertial Wind Power Input and Near-Inertial Energy

Figure 4.2 shows, for the year 2001, monthly-mean time series of near-inertial WPI, the amplitude of the near-inertial velocity at the surface, mixed-layer NIE, the mixed-layer depth, and the amplitude of the inertial wind-stress variance, IWSV (see Section 4.2.6), of the wind-stress averaged over the whole model domain and averaged over the regions R01 to R04 (see Section 4.2.4). Near-inertial WPI shows a broad maximum during austral fall (AMJ) and winter (JAS) which is largely reflected by the mixed-layer NIE. Despite the stronger wind-forcing in austral winter (JAS), the near-inertial amplitudes at the surface are maximal in austral summer (JFM) and minimal in austral winter (JAS) when near-inertial WPI is spread over a deeper mixed-layer. This agrees with the findings of *Chaigneau et al.* (2008) who present direct observational estimates for the annual cycles of near-inertial amplitudes at the surface. In our model experiment, the mixed-layer NIE peaks in austral spring (AMJ). This is contrary to the indirect estimate of *Chaigneau et al.* (2008) who, due to the lack of direct global-scale estimates of NIE at depth, assume the near-inertial amplitudes to be vertically uniform throughout the mixed-layer. They therefore estimate mixed-layer NIE as the product of the surface NIE and the mixed-layer depth and hence find that mixed-layer NIE to peak in austral winter (JAS) when the mixed layer is deep. The remarkable similarity of the time series of IWSV and near-inertial WPI is discussed in detail in Section 4.5

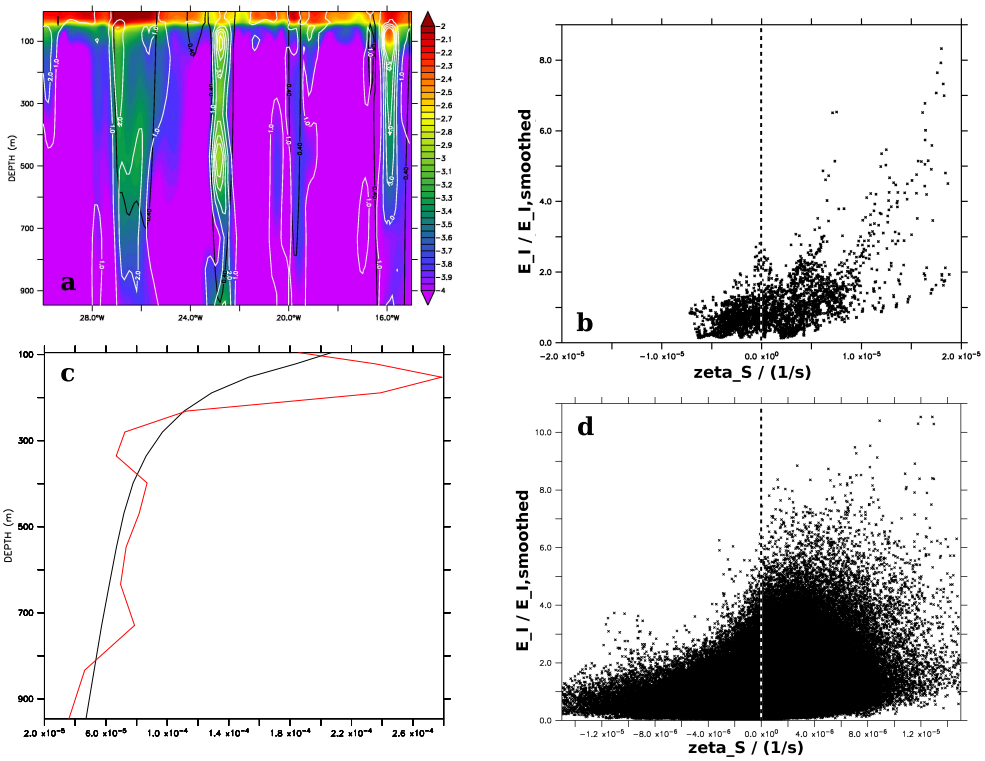

Figure 4.8: *(a) Zonal section at* $49.9°S$*. Colors show* $\log_{10}(E_I)$*, black contours show the* $0.4 \cdot 10^{-5}/s$ *isoline of* $\zeta_S \equiv (v_S)_x - (u_S)_y$*, and white contours show* E_{rel} *which is a measure for the strength of local maxima (see text). High* E_{rel} *coincides with positive* ζ_S *at depth. (b) Scatter plot of* E_{rel} *versus* ζ_S *for the data shown in (a). The dashed line indicates zero relative vorticity. (c) Horizontal (whole model domain) average of NIE* (m^2/s^2) *using all grid points (black line) and using only grid points (red line) where* ζ_S *at the surface exceeds the value of* $0.5 \cdot 10^{-5}/s$*. (d) Same as (b) but for the whole model domain and restricted to* $1000\,m$ *depth. All data show time averages for the first 36.5 days of the year 2001.*

4.5 The Relationship Between Near-Inertial Wind Power Input, Near-Inertial Energy and the Wind Forcing

We seek to explain the relationship between the wind-forcing at inertial timescales, IWSV, near-inertial WPI, and the amplitude of NIWs measured by the amplitude of the near-inertial velocity at the surface and the mixed-layer NIE.

4.5.1 Insensitivity of Near-Inertial Wind-Power Input to the Mixed-Layer Depth

As pointed out above, horizontal averages of monthly-mean IWSV and monthly-mean near-inertial WPI shown in Figure 4.2a and e follow each other closely.

Figure 4.9a shows a scatter plot of monthly-mean IWSV and near-inertial WPI averaged over bins of size $6^\circ \times 10^\circ$ (latitude×longitude). Near-inertial WPI is almost proportional to IWSV with a slight damping for very high values of IWSV. On the other hand, Figure 4.9b shows that near-inertial WPI divided by IWSV is largely independent of the mixed-layer depth.

As, for example, pointed out by *Plueddemann and Farrar* (2006), NIE is injected into the ocean mainly during strong events which often last for only a fraction of one inertial cycle, while the NIWs generated by such an event then decay on time scales typically of $O(5\,\text{days})$. Figure 4.10 shows near-inertial WPI and the amplitude of near-inertial velocity $|\vec{u}_I|$ for the top 150 m for a typical storm event. Near-inertial WPI is large for only a few hours and small during the subsequent decay phase. The initial response of $|\vec{u}_I|$ is constrained to the upper 10 m and then spreads to depths larger than 100 m within approximately 24 hours. The time-average of the near-inertial WPI time series shown in Figure 4.10 is dominated by the strong positive contribution on September 20, and this, in turn, is determined by the initial increase of $|\vec{u}_I|$ before NIE is spread to depth at a rate of approximately

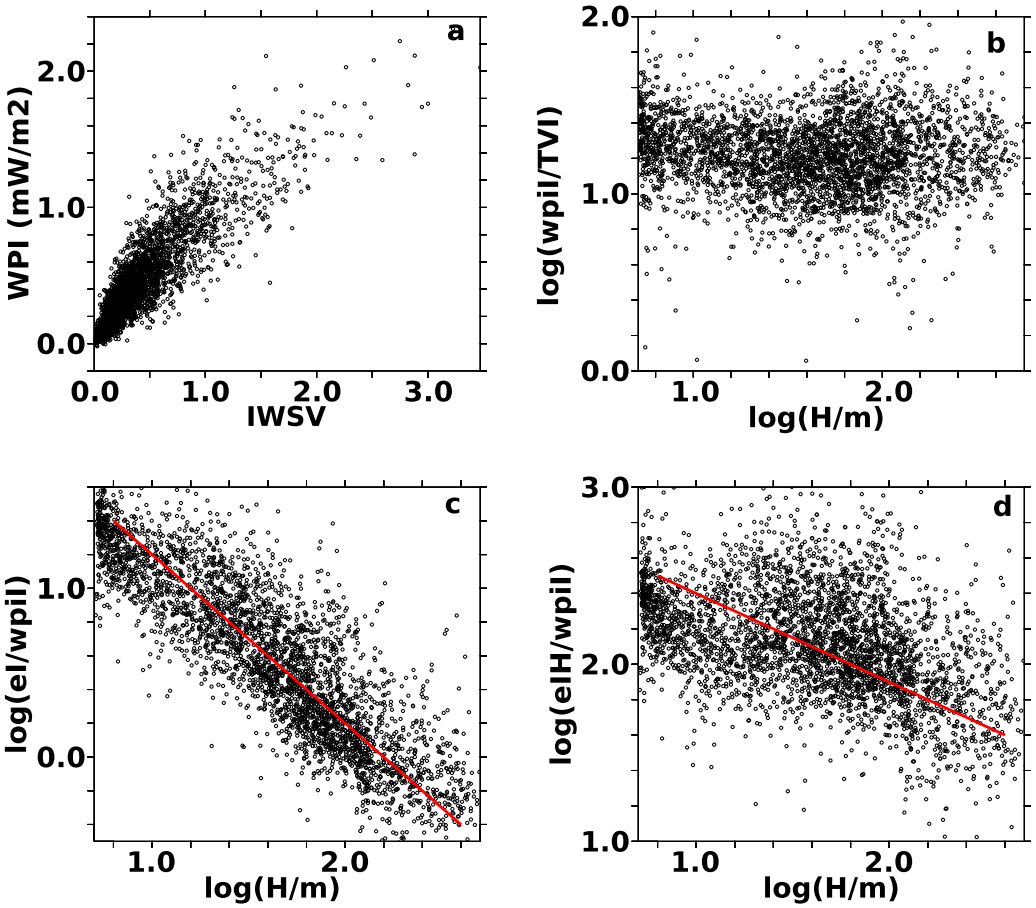

Figure 4.9: *(a) Inertial wind-stress variance, IWSV, (in arbitrary units) versus near-inertial WPI (in* $\mathrm{mW/m^2}$*). (b)* $\log_{10}$ *of the mixed-layer depth,* H*, versus* $\log_{10}$ *of the ratio of IWSV and near-inertial WPI. (c)* $\log_{10}$ *of the mixed-layer depth,* H*, versus* $\log_{10}$ *of surface NIE divided by near-inertial WPI. The slope of the red line is* -1*. Hence, the data are compatible with* $E_I(z=0) \propto WPI_I/H$*. (d)* $\log_{10}$ *of the mixed-layer depth,* H*, versus* $\log_{10}$ *of mixed-layer NIE divided by near-inertial WPI. The slope of the red line is* -0.5*. Each point represents a monthly and a horizontal mean over a* $6^\circ \times 10^\circ$ *(latitude*$\times$*longitude) bin.*

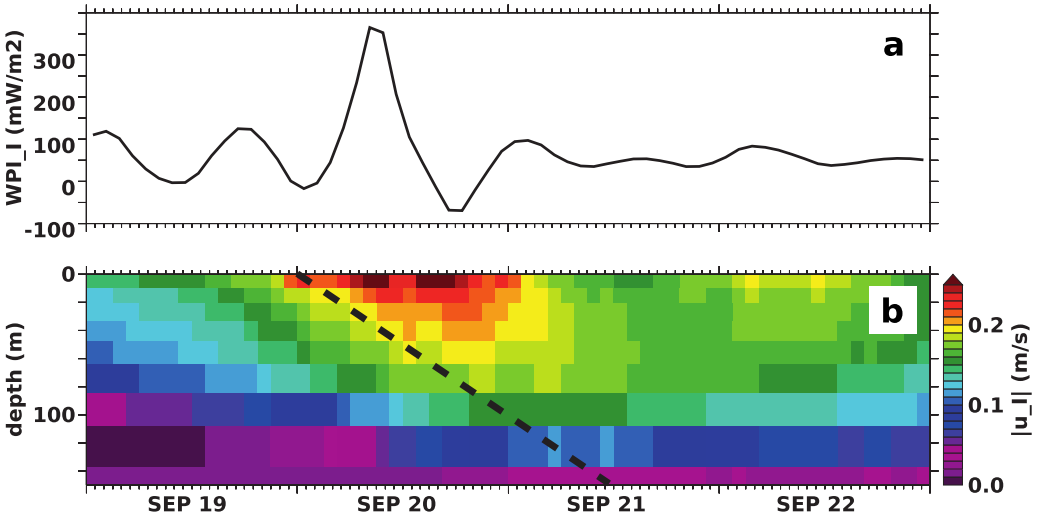

Figure 4.10: *Near-inertial WPI (a) and near-inertial amplitude* $|\vec{u}_I|$ *(b) at* $52°S$ *and* $136°E$ *from September 19, 2001 to September 22, 2001. The black dashed line has a slope of* $100\,\mathrm{m}/24\,\mathrm{hours} \approx 5\mathrm{m/h}$.

5 m/hour.

Note that the event shown in Figure 4.10 is chosen as a representative example for many similar events scattered all over the model domain and over the whole year 2001. The characteristics of all these events are similar: Strong positive near-inertial WPI for a short time, often less than an inertial cycle, spreading of $|\vec{u}_I|$ to depth at $O(5\,\mathrm{m/s})$, and subsequent decay of $|\vec{u}_I|$ that is largely vertically uniform over a surface layer that often coincides with the mixed-layer depth.

Hence, we conclude that the insensitivity of near-inertial WPI to the mixed-layer depth that we find in our model experiment can be explained by the fact that the vertical homogenization of $|\vec{u}_I|$ in the mixed layer happens on time scales larger than the duration of strong positive near-inertial WPI events. We note that in the slab-ocean model PM70, the vertical homogenization happens, by definition, instantaneously, and that hence PM70 is unable to capture the insensitivity of near-inertial WPI to the mixed-layer depth found here.

4.5.2 Meridional Distribution of Inertial Variability of the Wind Stress

Figure 4.11a shows the sum of the zonally averaged spectral densities of the wind stress $\tilde{\tau}^x(\omega)$ and $\tilde{\tau}^y(\omega)$, together with the inertial frequency f. The contribution of wind stress to near-inertial WPI is set by the spectral density close to the inertial frequency, f, that is indicated by the thick black line. It is immediately clear that the reduced near-inertial WPI for high latitudes is predominantly due to the fact that NIWs at the ocean surface "sample" the wind stress at frequencies with weaker and weaker variability the higher the latitude. Another notable feature of the spectral density of the wind stress is the enhanced variability at diurnal frequencies of 1 cpd (cycles per day), which we attribute to the land-sea breeze (see *Elipot and Lumpkin* (2008), *Gille et al.* (2003), and *Gille et al.* (2005)). At $30°S$, the inertial frequency and the diurnal cycle of the wind stress are in resonance and lead to enhanced IWSV.

Figure 4.11b shows the zonal averages of IWSV, of temporally averaged near-inertial WPI, of the variance of the wind-stress, and of the mean modulus of the wind-stress all based on the 6-hourly wind-stress driving the primitive-equation model during the year 2001. The meridional maximum of IWSV and near-inertial WPI is shifted to the north compared to both the maximum of wind-stress variance, and of the modulus of the wind-stress. North of their maxima, IWSV and near-inertial WPI are generally larger than south of their maxima, while the wind-stress variance and the modulus of the wind stress are largely symmetric about $55°S$. The resonance of the inertial frequency close to the northern boundary of the model domain at $30°S$ is clearly visible in zonally averaged IWSV. In temporally and zonally averaged near-inertial WPI, the enhancement at $30°S$ is less pronounced. Note, however, that especially during austral summer and fall, there is enhanced near-inertial WPI close to $30°S$ within approx $10°$ longitude from the continents (see Figure 4.7b and c).

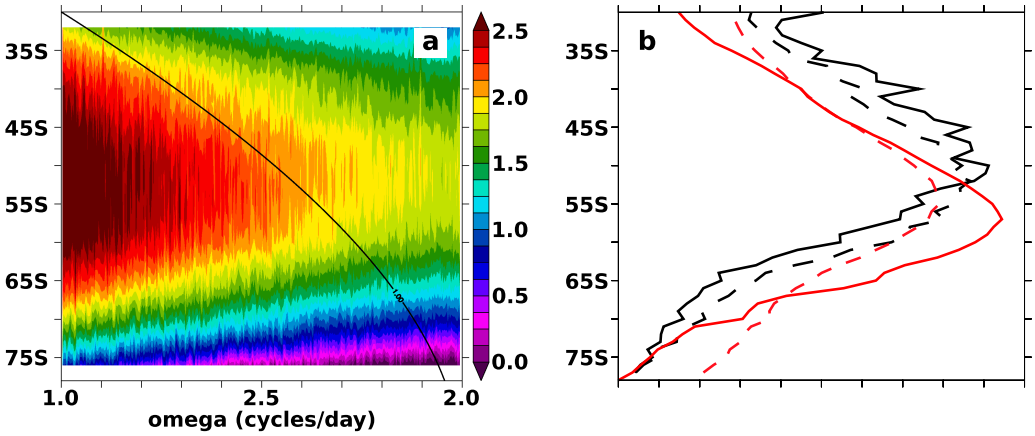

Figure 4.11: *(a) Colors show zonally averaged spectral density of the wind stress* $(\tilde{\tau}^x)^2+(\tilde{\tau}^y)^2$ *in arbitrary units. The black line indicates the dependence of the modulus of the inertial frequency,* f*, depending on the latitude. (b) Zonal averages of the spectral density of the wind-stress evaluated at the inertial frequency (solid black line), of time-averaged near-inertial WPI (dashed black line), of the variance of the wind-stress (solid red line), and of the time-average of the modulus of the wind-stress (dashed red line). The zonal averages have been normalized by their meridional averages. All data are derived from the 6-hourly wind-stress of the year 2001 that is used to drive the primitive-equation model.*

4.5.3 The Influence of the Mixed Layer Depth

In the PM70 slab model (see Section 4.2.3), the wind-power input term acts to accelerate currents that are uniformly distributed over the whole mixed-layer depth. Hence, NIE in the slab model is proportional to the inverse of the mixed-layer depth (see (4.9). We find that the assumption of vertically uniform near-inertial amplitudes throughout the mixed-layer does not hold (see Figure 4.3) while there is a clear separation between the mixed-layer, where strong near-inertial amplitudes are found, and the interior ocean, where near-inertial amplitudes are weaker by several orders of magnitude. For the near-surface NIE shown in Figure 4.9c, the relation $NIE \propto H^{-1}$ from (4.9) is satisfied almost exactly. NIE integrated over the whole mixed-layer depth is still sensitive to a monotonically rising function of the inverse of the mixed-layer depth (Figure 4.9d compares the model output to $H^{-0.5}$), and the simple PM70 scaling (4.10), which predicts mixed-layer NIE to be independent of the mixed-layer depth, no longer holds. The meridional maximum of the mixed-layer depth (see Figure 4.1) approximately coincides with the meridional maximum of near-inertial WPI (see Figure 4.6a). Hence, the effect of near-inertial WPI close to its meridional maximum is reduced and the meridional maximum of NIE at the surface and NIE integrated over the mixed layer (see Figure 4.6b) is found further north.

4.6 Recent Trends in the Wind Forcing and their Implications for Near-Inertial Energy and Near-Inertial Wind Power Input

In this section, we examine recent decadal trends of the inertial variability of the wind-forcing, as measured by IWSV defined in (4.11), to gain insight into decadal variability of near-inertial WPI and NIE in the Southern Ocean. As was shown in Section 4.4 and in Section 4.5, near-inertial WPI almost exactly follows IWSV, at least for the seasonal cycle, and we assume this

relationship continues to hold on longer time scales.

We diagnose monthly IWSV as described in Section 4.2.6 based on 6-hourly ERA-Interim winds covering the years 1979 to 2011. In Section 4.2.7, we show that ERA-40 winds from the pre-satellite era (before 1979) produce much weaker high-frequency wind variability than those post 1979, and hence should not be used to estimate high-frequency properties of the wind forcing.

Figure 4.12 shows the annual cycle of IWSV based on the first 16 years and the last 16 years of ERA-Interim. There is a general shift towards stronger IWSV in the second half of ERA-Interim. When averaged over the whole Southern Ocean south of $30°S$, the increase of IWSV is bigger than two temporal standard deviations (based on monthly means) of the horizontally and monthly averaged data throughout the year.

Figure 4.13 shows time-series of IWSV split into the four seasons JFM, AMJ, JAS, OND, and into the four regions R01 to R04 (see Section 4.2.4) for the years 1979 through 2011 together with estimates of linear trends. We assess the significance of the trends using a bootstrap approach (*Efron and Tibshirani*, 1986) which we outline in the following. From the full time series, we draw 10^3 random subsamples $\{t^n, IWSV(t^n)\}$, each of which has the same length as the full time series, but may have doublers. Then, for each sub-sample indicated by the superscript n, the linear trend S^n is estimated as

$$S^n = \frac{\overline{(t^n)' \, (IWSV(t^n))'}}{\overline{(t^n)'^2}} \tag{4.12}$$

where $\overline{(\ldots)}$ denotes a time-average and the prime denotes a deviation thereof. We estimate the trend of the full time series as the mean of all S^n and error of S as the standard deviation of all S^n.

Horizontally averaged IWSV based on ERA-Interim winds shows a significant upward trend for all four seasons if averaged over the whole Southern Ocean south of $30°S$. Split into different regions, the picture is more diverse, but upward trends of IWSV prevail. Table 4.1 lists relative increases of IWSV associated with the trend estimates for the 33 years covered by ERA-Interim. Averaged over the full model domain, annual mean IWSV increased by $(16.4 \pm 2.2)\%$. In R01 and R02, the increases of annual mean IWSV were

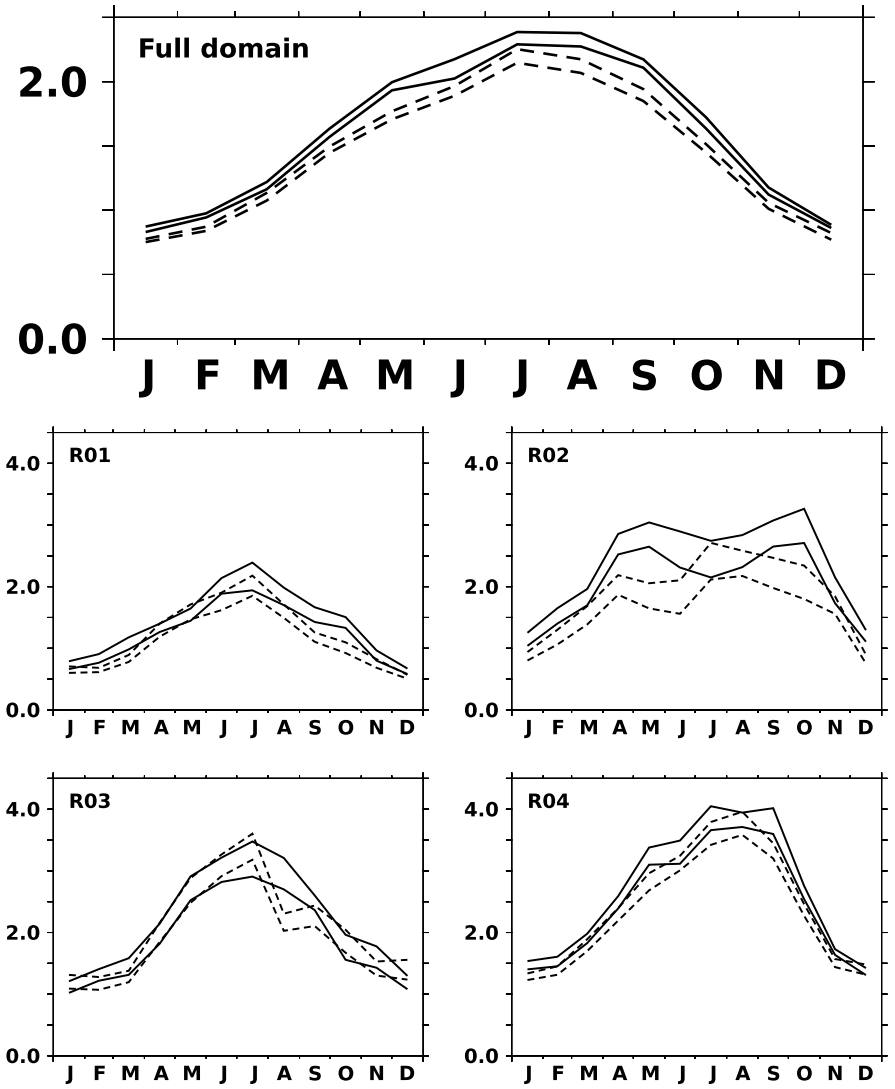

Figure 4.12: *Annual cycles of the horizontal averages of IWSV for the last 16 years of ERA-Interim (solid lines), and for the first 16 years of ERA-Interim (dashed lines). The upper and lower lines show the annual cycle ± one standard deviation (see text). From left to right, IWSV is averaged over the full domain, and over the regions R01, R02, R03, R04.*

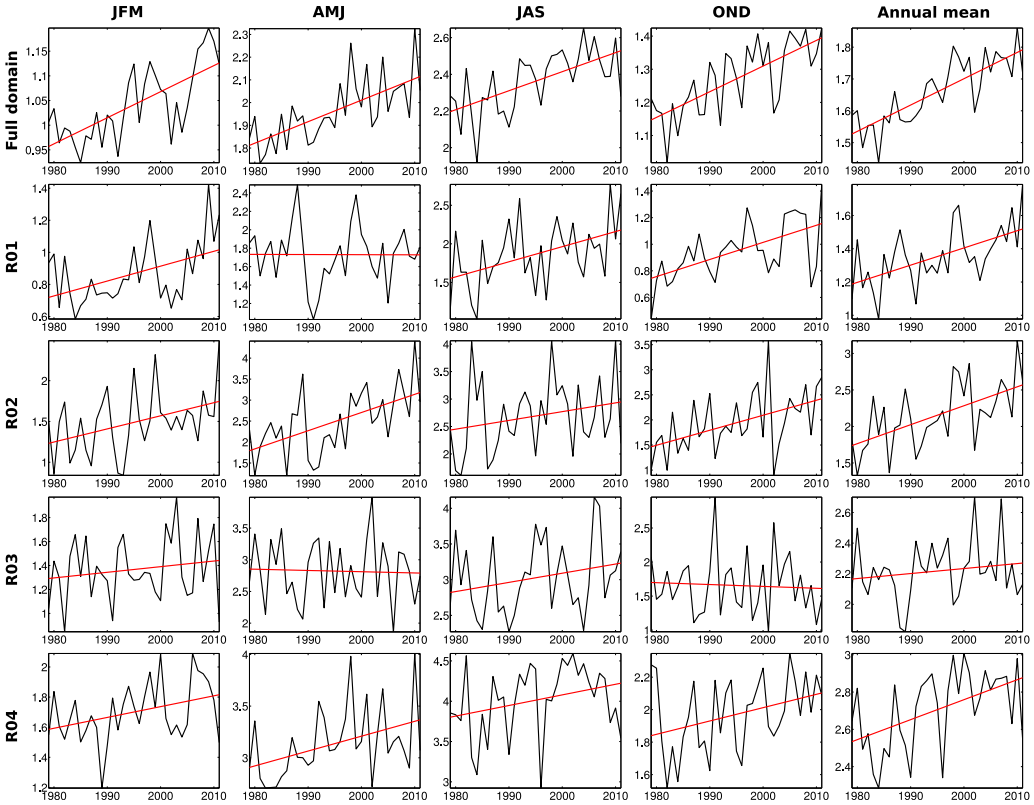

Figure 4.13: *Seasonal and horizontal averages of IWSV together with the linear trends measured as the mean of an $N = 1e3$ bootstrap ensemble (see text). Top to bottom: Full domain, R01, R02, R03, R04. Left to right: JFM, AMJ, JAS, OND, annual average.*

	JFM	AMJ	JAS	OND	Annual mean
Full	16.8 ± 2.8	15.7 ± 3.1	14.7 ± 3.8	20.1 ± 3.1	16.4 ± 2.2
R01	35.2 ± 13.3	-0.6 ± 8.0	35.1 ± 12.0	44.3 ± 13.5	25.2 ± 6.8
R02	34.7 ± 14.0	58.5 ± 13.8	19.5 ± 16.1	50.4 ± 14.4	39.8 ± 9.3
R03	11.6 ± 13.0	-0.9 ± 9.7	14.0 ± 9.7	-5.1 ± 12.4	4.8 ± 4.8
R04	14.3 ± 6.5	15.0 ± 6.0	10.8 ± 6.1	13.6 ± 6.8	13.1 ± 4.0

Table 4.1: *Slopes $S \pm \sigma_S$ of the linear fits shown in Figure 4.13. Shown is the ratio of the increase or decrease of IWSV associated with the slope acting for 33 years relative to the temporal mean over 33 years in percent.*

stronger (25.2% and 39.8%) than averaged over the whole domain, and in R04, the increases were lower (13.1%) than averaged over the whole domain. Annual mean IWSV in R03 does not show a significant trend.

Figure 4.14a shows the regression of annual-mean IWSV onto the annual-mean SAM index (see Section 4.2.8). A positive SAM-index is associated with enhanced IWSV south of approximately $50°S$ and reduced IWSV north of $50°S$. The strongest SAM-related increase of IWSV is found over the Pacific Sector of the ACC, which roughly corresponds to our region R02 and which also shows the strongest positive trend of annual-mean IWSV (Figure 4.14b). The modulus of the correlation of the annual-mean SAM index and the annual-mean IWSV can be understood as a measure of the fraction of interannual variability of IWSV associated with the SAM. Over the Pacific Sector of the ACC (R02), the strong positive trend of IWSV and a high correlation (between 0.5 and more than 0.8) of IWSV and the SAM index coincide. Over the other regions, the spatial distribution of the correlation between the SAM and IWSV is noisy. Comparison of basin-wide and regional averages of annual-mean IWSV (Figure 4.15) further support the picture that in R02, it is the gradual shift to a more positive SAM index during the last three decades that drives the stronger IWSV. In the other regions and in the whole model domain, only years of very strong positive or negative SAM index leave their signature in annual-mean IWSV (see, e.g., the years 1998 and 1999).

Given the fact that near-inertial WPI very closely follows IWSV on monthly to seasonal time scales, and given the insensitivity of near-inertial WPI to

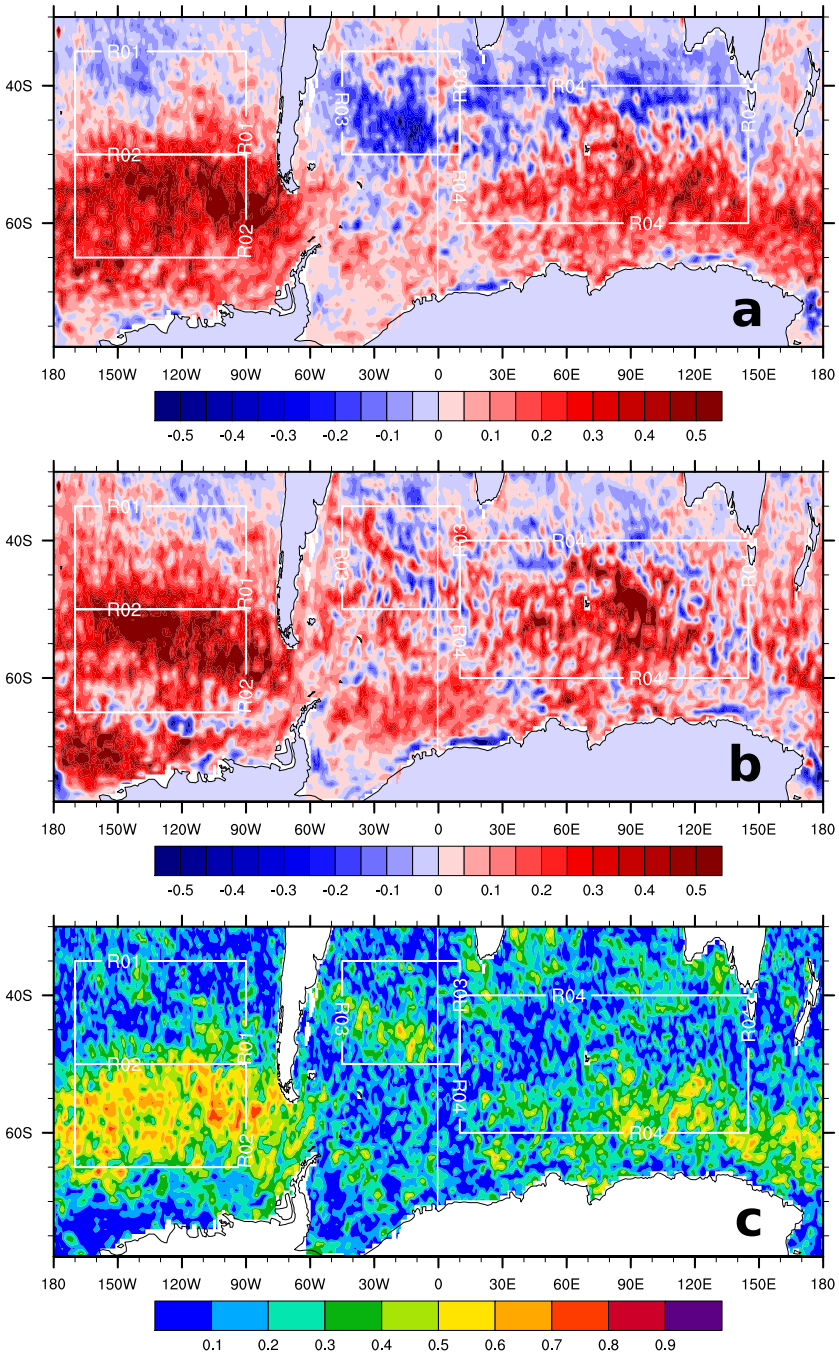

Figure 4.14: *(a) SAM-related IWSV pattern. (b) Trend of IWSV over the whole ERA-Interim record. (c) Modulus of the correlation of IWSV to the SAM index. Assuming that all years are independent, the critical correlation for* 95 % *confidence is* 0.34*. All data are based on the annual-mean SAM index and annual-mean IWSV.*

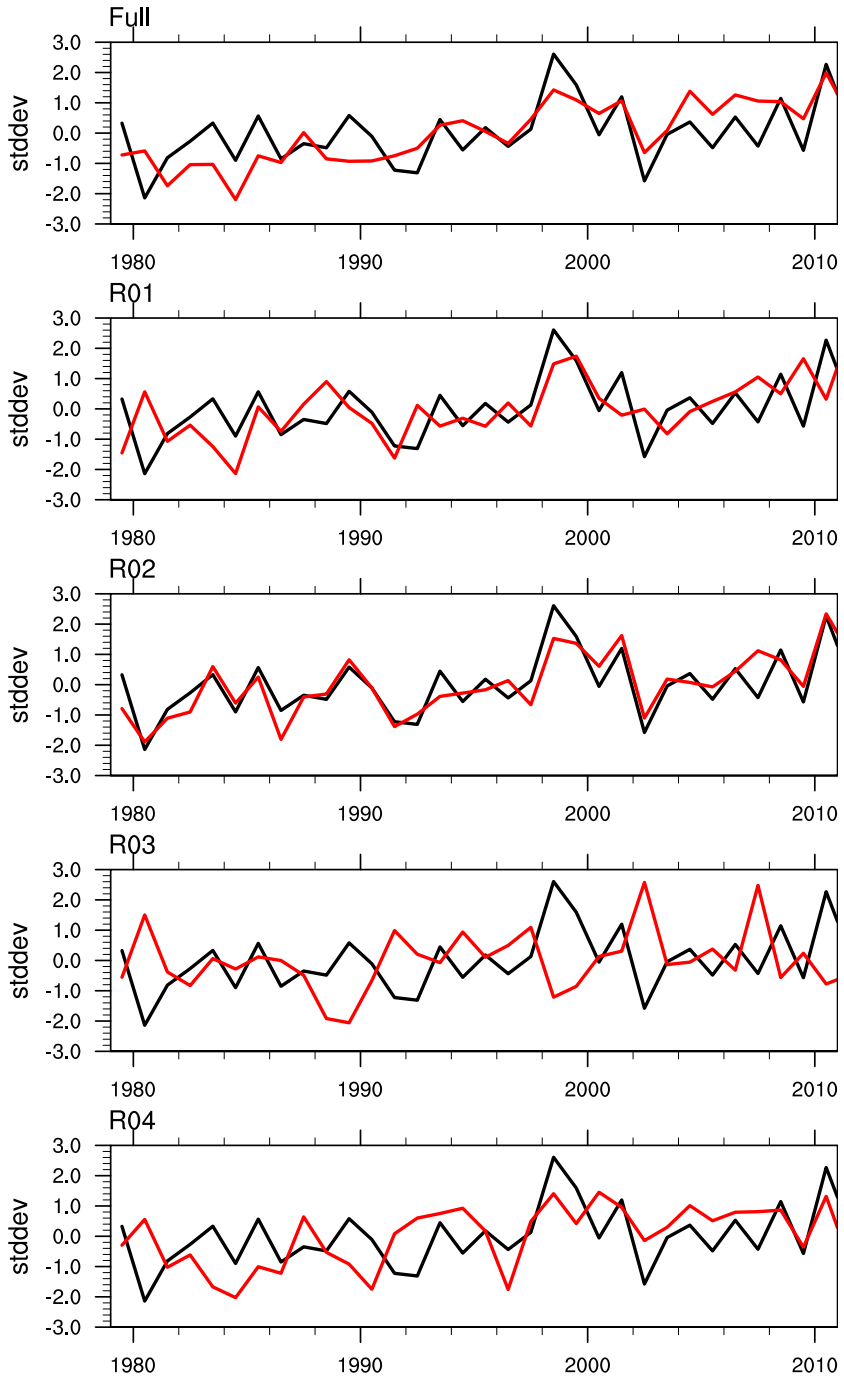

Figure 4.15: *Annual-mean SAM index (black lines) and horizontally averaged annual-mean IWSV (red lines) for the full model domain and for the regions R01 to R04. The time-series of horizontally averaged annual-mean IWSV has been normalized to yield zero mean and unit standard deviation.*

the mixed-layer depth (see Section 4.5.1), we conclude that near-inertial WPI over the Southern Ocean has undergone a significant upward trend during the last three decades.

Mixed-layer NIE and NIE at the surface, however, are sensitive to the mixed-layer depth. *Sallee et al.* (2010) present observational evidence, that the mixed-layer depth responds to changes in the SAM in a zonally asymmetric way. They find that the mixed-layer-depth anomaly associated to ± 1 standard deviation of the SAM index can be as big as $\pm 100\,\mathrm{m}$ in the eastern Indian Ocean and in the central Pacific Ocean which correspond to parts of our regions R04 and R02. Given the marked upward trend of the SAM index in recent decades (*Marshall*, 2003; *Swart and Fyfe*, 2012) that is also visible in Figure 4.15, the associated mixed-layer deepening may partly compensate the effect of increased IWSV on mixed-layer and near-surface NIE in these regions. In fact, one might hypothesize that at least part of the observed SAM-related mixed-layer deepening is due to the enhanced IWSV (*Pollard et al.*, 1972).

4.7 Summary and Conclusions

In Section 4.3, we highlighted the spatial distribution of time-averaged near-inertial WPI and NIE. While near-inertial WPI shows a large-scale zonal structure with meridional maxima between $65°S$ and $40°S$ that is superimposed by many smaller hot-spots, mixed-layer NIE does not reflect the largely zonal structure of near-inertial WPI, but agrees in the distribution of the smaller hot-spots. In the vertical, we found that there generally is a separation into a surface layer with high levels of NIE and the interior ocean with much lower NIE. However, the simple picture of vertically uniform near-inertial velocity throughout the surface mixed layer could not be verified. Furthermore, we showed that there is a clear enhancement of NIE at depth, which is almost exclusively associated to the presence of anticyclonic relative vorticity.

In Section 4.4, we examined horizontal averages of monthly-mean near-inertial WPI and NIE. While near-inertial WPI and mixed-layer NIE show

broad maxima during austral fall and winter, which largely follow the increased inertial wind-stress variability, IWSV, the near-surface near-inertial amplitudes are maximal in austral summer and spring when NIE injected at the surface spreads over a shallower mixed-layer.

We seeked to systematize the relation between wind-forcing at the inertial frequency, near-inertial WPI and NIE in Section 4.5. Near-inertial WPI was found to very closely follow IWSV and to be largely insensitive of the mixed-layer depth. This, we attributed to the fact that near-inertial WPI is injected into the ocean mainly by strong events which often last only for a few hours, while the vertical homogenization of NIE within the mixed layer is determined by longer time-scales. Hence, time-averaged near-inertial WPI is determined by the strong events and is insensitive to the mixed-layer depth. On the other hand, time-averaged NIE at the surface was shown to be sensitive to the mixed-layer depth with larger values of near-surface NIE for shallower mixed-layers. This is because after the short resonant events of strong near-inertial WPI, NIE decays on time-scales of several days and feels the influence of the mixed-layer depth. We found that both IWSV and the closely related near-inertial WPI are maximal north of the latitudes of the strongest mean wind-stress and of the strongest wind-stress variability integrated over the whole frequency domain. We explained this asymmetry by the fact that the inertial frequency depends on the latitude and that, hence, the wind-stress is sampled at frequencies with less and less variability the higher the latitude.

In Section 4.6, we examined trends of IWSV based on the ERA-Interim reanalysis, that covers the last three decades (1979 to 2011), and found annual-mean IWSV averaged over the whole model domain to increase by $(16.4 \pm 2.2)\,\%$. In the South Pacific and in the Pacific Sector of the ACC, annual-mean IWSV increased by $25.2\,\%$ and $39.8\,\%$ respectively. Furthermore, we showed that on inter-annual to decadal time scales, IWSV in the Pacific Sector of the ACC (region R02) is largely determined by the SAM index. Assuming that the close relationship between IWSV and near-inertial WPI, that was found for monthly to seasonal time scales, also holds on decadal time scales, we concluded that in the last three decades, near-inertial

WPI also significantly increased. The implications for NIE, however, depend on decadal variability of the mixed-layer depth. *Sallee et al.* (2010) present evidence for a recent zonally asymmetric change of the mixed-layer depth that is associated to the increase of the SAM index over the last three decades. They show that a positive SAM leads to a deepening of the mixed layer in the Pacific Sector of the ACC (our region R02), where we found the largest SAM-related and the largest overall increase of IWSV. Hence, in R02, the effect of increased mixed-layer depth and increased IWSV on NIE may at least partly compensate.

Our results highlight the importance of the knowledge about the time-dependence of the vertical distribution of NIE and about the vertical spreading of NIE, which directly affect the magnitude of near-inertial WPI, and hence are critical to the levels of NIE in the ocean. While there are global-scale observational estimates of near-inertial amplitudes at the surface (*Chaigneau et al.*, 2008; *Elipot and Lumpkin*, 2008), direct observations of near-inertial WPI and of the vertical distribution of NIE which could shed light on the relation of near-inertial WPI and IWSV are restricted to measurements in a few locations.

Chapter 5

Summary

This thesis aimed at understanding the influence of SVD on the dynamics of the Southern Ocean as represented by a realistic numerical ocean model covering all ocean south of $30°S$. It highlighted the response of the Southern Ocean at near-inertial frequencies (Chapter 2) and at sub-inertial frequencies (Chapter 3). Furthermore, it examined the spatial and temporal distribution of NIE in the Southern Ocean (Chapter 4).

The main results of Chapter 2, which highlights the impact of SVD on the near-inertial frequency band, are the following:

- SVD causes horizontally averaged NIE to be reduced by approximately 40 % and horizontally averaged near-inertial WPI to be reduced by approximately 20 %. Locally, the reduction can be much higher.
- The reduction of NIE is found throughout the water column. This indicates that NIE in the model mainly feeds from input at the surface.
- The observed reduction of NIE and near-inertial WPI can be explained by the fact that SVD, to leading order, adds a linear damping term to the momentum equation governing the temporal evolution of near-inertial oscillations in the mixed-layer. This damping term is found to be inversely proportional to the mixed-layer depth. Hence, the largest SVD-induced reduction of NIE and near-inertial WPI is found where the mixed-layer is shallow.

- Examination of the seasonal cycle shows that (in the Southern Ocean) the SVD-induced reduction of NIE and near-inertial WPI is biggest in austral summer, when the mixed-layer is shallower than in austral winter.

The main results of Chapter 3, which examines the response of the sub-inertial frequency band to SVD, are the following:

- Horizontally averaged sub-inertial WPI and mesoscale EKE are reduced by approximately 15 % and 26 % respectively, if SVD is used. Locally, the reduction can be much higher.

- The largest SVD-induced reduction of sub-inertial WPI is found where the ACC and the prevailing westerly winds align. The largest reduction of mesoscale EKE occurs along the ACC, where the most vigorous mesoscale-eddy field in the Southern Ocean is found.

- SVD acts to reduce the variance of monthly-mean and annual-mean wind stress, sub-inertial WPI, mesoscale EKE, and transport through Drake Passage. Otherwise, the time-dependence of the wind-stress, sub-inertial WPI, and transport through Drake Passage is not affected and the respective time-series remain highly correlated across model experiments which only differ in the way the wind stress is parameterized.

- The time-average of transport through Drake Passage is found to undergo a small increase (by 1.8 %) if surface-velocity-dependent wind stress is used.

The findings of Chapter 2 and 3 show that it is important to include the ocean-surface velocity into the wind-stress parameterization and that neglecting it can lead to significantly increase estimates of WPI on all time scales, of NIE, and of mesoscale EKE.

The main results of Chapter 4, which assesses the spatial and temporal distribution of NIE and of near-inertial WPI, are the following:

- Near-inertial WPI in the model is almost proportional to IWSV, while NIE is modulated by the inverse of the mixed-layer depth.
- The close relationship between near-inertial WPI and IWSV is used to indirectly assess decadal trends of near-inertial WPI based on a reanalysis wind product. From 1979 to 2011, IWSV averaged over the Southern Ocean increased by 16 %. In the South Pacific, IWSV increased by approximately 39 %, while in the South Atlantic, IWSV did not significantly increase or decrease.
- The decadal and inter-annual variability of IWSV (and hence near-inertial WPI) in the South Pacific is found to be governed by the SAM.
- There are horizontal maxima of NIE at depths much larger than the depth of the surface-mixed layer. The fact that these maxima are almost exclusively associated with anti-cyclonic eddies, points to the role of anti-cyclonic eddies in providing NIE with a pathway to the deep ocean.
- It is found, that before approximately 1979, the high-frequent variability of reanalysis winds shows large and likely unrealistic fluctuations. This renders model-based estimates of IWSV and near-inertial WPI based on reanalysis winds prior to 1979 highly uncertain.

Bibliography

Alford, M. (2003), Improved global maps and 54-year history of wind-work on ocean inertial motions, *Geophysical Research Letters*, *30*(8), doi: 10.1029/2002GL016614.

Barnier, B., L. Siefridt, and P. Marchesiello (1995), Thermal Forcing for a global ocean circulation model using a 3-year climatology of ECMWF analyses, *Journal of Marine Systems*, *6*(4), 363–380, doi: 10.1016/0924-7963(94)00034-9.

Blanke, B., and P. Delecluse (1993), Variability of the tropical Atlantic Ocean simulated by a general-circulation model with 2 different mixed-layer physics, *Journal of Physical Oceanography*, *23*(7), 1363–1388, doi: 10.1175/1520-0485(1993)023⟨1363:VOTTAO⟩2.0.CO;2.

Chaigneau, A., O. Pizarro, and W. Rojas (2008), Global climatology of near-inertial current characteristics from Lagrangian observations, *Geophysical Research Letters*, *35*(13), doi: 10.1029/2008GL034060.

Chavanne, C. P., E. Firing, and F. Ascani (2012), Inertial Oscillations in Geostrophic Flow: Is the Inertial Frequency Shifted by zeta/2 or by zeta?, *Journal of Physical Oceanography*, *42*(5), 884–888, doi: 10.1175/JPO-D-12-031.1.

Cunningham, S., S. Alderson, B. King, and M. Brandon (2003), Transport and variability of the Antarctic Circumpolar Current in Drake Passage, *Journal of Geophysical Research - Oceans*, *108*(C5), doi: 10.1029/2001JC001147.

D'Asaro, E. (1985), The energy flux from the wind to near-inertial motions in the surface mixed layer, *Journal of Physical Oceanography*, *15*(8), 1043–1059, doi: 10.1175/1520-0485(1985)015⟨1043:TEFFTW⟩2.0.CO;2.

de Boyer Montegut, C., G. Madec, A. Fischer, A. Lazar, and D. Iudicone (2004), Mixed layer depth over the global ocean: An examination of profile data and a profile-based climatology, *Journal of Geophysical Research - Oceans*, *109*(C12), doi: 10.1029/2004JC002378.

Dewar, W., and G. Flierl (1987), Some effects of the wind on rings, *Journal of Physical Oceanography*, *17*(10), 1653–1667, doi: 10.1175/1520-0485(1987)017⟨1653:SEOTWO⟩2.0.CO;2.

Donelan, M., B. Haus, N. Reul, W. Plant, M. Stiassnie, H. Graber, O. Brown, and E. Saltzman (2004), On the limiting aerodynamic roughness of the ocean in very strong winds, *Geophysical Research Letters*, *31*(18), doi: 10.1029/2004GL019460.

Duhaut, T., and D. Straub (2006), Wind stress dependence on ocean surface velocity: Implications for mechanical energy input to ocean circulation, *Journal of Physical Oceanography*, *36*(2), 202–211, doi: 10.1175/JPO2842.1.

Eden, C. (2006), Thickness diffusivity in the Southern Ocean, *Geophysical Research Letters*, *33*(11), doi: 10.1029/2006GL026157.

Efron, B., and R. Tibshirani (1986), Bootstrap Methods for Standard Errors, Confidence Intervals, and Other Measures of Statistical Accuracy, *Statistical Science*, *1*(1), 54–77.

Elipot, S., and R. Lumpkin (2008), Spectral description of oceanic near-surface variability, *Geophysical Research Letters*, *35*(5), doi: 10.1029/2007GL032874.

Furuichi, N., T. Hibiya, and Y. Niwa (2008), Model-predicted distribution of wind-induced internal wave energy in the world's oceans, *Journal of Geophysical Research - Oceans*, *113*(C9), doi: 10.1029/2008JC004768.

Gaspar, P., Y. Gregoris, and J. Lefevre (1990), A simple eddy kinetic-energy model for simulations of the oceanic vertical mixing - tests at Station Papa and Long-Term Upper Ocean Study Site, *Journal of Geophysical Research - Oceans*, *95*(C9), 16,179–16,193, doi: 10.1029/JC095iC09p16179.

Gill, A. (1984), On the behavior of internal waves in the wakes of storms, *Journal of Physical Oceanography*, *14*(7), 1129–1151.

Gill, A. E. (1982), *Atmosphere-Ocean Dynamics*, Academic Press.

Gille, S., S. Smith, and S. Lee (2003), Measuring the sea breeze from QuikSCAT scatterometry, *Geophysical Research Letters*, *30*(3), doi: 10.1029/2002GL016230.

Gille, S., S. Smith, and N. Statom (2005), Global observations of the land breeze, *Geophysical Research Letters*, *32*(5), doi: 10.1029/2004GL022139.

Gong, D., and S. Wang (1999), Definition of Antarctic Oscillation Index, *Geophysical Research Letters*, *26*(4), 459–462, doi: 10.1029/1999GL900003.

Hughes, C., and E. Ash (2001), Eddy forcing of the mean flow in the Southern Ocean, *Journal of Geophysical Research-Oceans*, *106*(C2), 2713–2722, doi: 10.1029/1999JC900332.

Hughes, C., M. Meredith, and K. Heywood (1999), Wind-driven transport fluctuations through drake passage: A southern mode, *Journal of Physical Oceanography*, *29*(8, 2), 1971–1992, doi: 10.1175/1520-0485(1999)029⟨1971:WDTFTD⟩2.0.CO;2.

Hughes, C. W., and C. Wilson (2008), Wind work on the geostrophic ocean circulation: An observational study of the effect of small scales in the wind stress, *Journal of Geophysical Research - Oceans*, *113*(C2), doi: 10.1029/2007JC004371.

Hutchinson, D. K., A. M. Hogg, and J. R. Blundell (2010), Southern Ocean Response to Relative Velocity Wind Stress Forcing, *Journal of Physical Oceanography*, *40*(2), 326–339, doi: 10.1175/2009JPO4240.1.

Jiang, J., Y. Lu, and W. Perrie (2005), Estimating the energy flux from the wind to ocean inertial motions: The sensitivity to surface wind fields, *Geophysical Research Letters*, *32*(15), doi: 10.1029/2005GL023289.

Jing, Z., L. Wu, L. Li, C. Liu, X. Liang, Z. Chen, D. Hu, and Q. Liu (2011), Turbulent diapycnal mixing in the subtropical northwestern Pacific: Spatial-seasonal variations and role of eddies, *Journal of Geophysical Research - Oceans*, *116*, doi: 10.1029/2011JC007142.

Jochum, M., B. P. Briegleb, G. Danabasoglu, W. G. Large, N. J. Norton, S. R. Jayne, M. H. Alford, and F. O. Bryan (2013), The Impact of Oceanic Near-Inertial Waves on Climate, *Journal of Climate*, *26*(9), 2833–2844, doi: 10.1175/JCLI-D-12-00181.1.

Joyce, T. M., J. M. Toole, P. Klein, and L. N. Thomas (2013), A near-inertial mode observed within a gulf stream warm-core ring, *Journal of Geophysical Research - Oceans*, *118*(4), 1797–1806, doi: 10.1002/jgrc.20141.

Kunze, E. (1985), Near-inertial wave-propagation in geostrophic shear, *Journal of Physical Oceanography*, *15*(5), 544–565, doi: 10.1175/1520-0485(1985)015⟨0544:NIWPIG⟩2.0.CO;2.

Large, W., and S. Pond (1981), Open Ocean Momentum Flux Measurements in Moderate to Strong Winds, *Journal of Physical Oceanography*, *11*(3), 324–336, doi: 10.1175/1520-0485(1981)011⟨0324:OOMFMI⟩2.0.CO;2.

Levitus, S., and T. Boyer (1994), World Ocean Atlas 1994. Volume 4: Temperature, *NOAA Atlas NEDSIS 4*, NOAA, Washington D.C.

Levitus, S., R. Burgett, and T. Boyer (1994), World Ocean Atlas 1994. Volume 3: Salinity, *NOAA Atlas NEDSIS 3*, NOAA, Washington D.C.

Luo, J., S. Masson, E. Roeckner, G. Madec, and T. Yamagata (2005), Reducing climatology bias in an ocean-atmosphere CGCM with improved coupling physics, *Journal of Climate*, *18*(13), 2344–2360, doi: 10.1175/JCLI3404.1.

Marshall, G. (2003), Trends in the southern annular mode from observations and reanalyses, *Journal of Climate*, *16*(24), 4134–4143.

Munday, D. R., H. L. Johnson, and D. P. Marshall (2013), Eddy Saturation of Equilibrated Circumpolar Currents, *Journal of Physical Oceanography*, *43*(3), 507–532, doi: 10.1175/JPO-D-12-095.1.

Munk, W., and C. Wunsch (1998), Abyssal recipes II: energetics of tidal and wind mixing, *Deep-Sea Research Part I-Oceanographic Research Papers*, *45*(12), 1977–2010, doi: 10.1016/S0967-0637(98)00070-3.

Orsi, A., T. Whitworth, and W. Nowlin (1995), On The Meridional Extent and Fronts of the Antarctic Circumpolar Current, *Deep-Sea Research Part I-Oceanographic Research Papers*, *42*(5), 641–673.

Pacanowski, R. (1987), Effect of equatorial currents on surface stress, *Journal of Physical Oceanography*, *17*(6), 833–838, doi: 10.1175/1520-0485(1987)017⟨0833:EOECOS⟩2.0.CO;2.

Plueddemann, A., and J. Farrar (2006), Observations and models of the energy flux from the wind to mixed-layer inertial currents, *Deep-Sea Research Part II-Topical Studies in Oceanography*, *53*(1-2), 5–30, doi: 10.1016/j.dsr2.2005.10.017, International Conference on Ocean Mixing, Victoria, CANADA, OCT 11-14, 2004.

Pollard, R., and R. Millard (1970), Comparison between observed and simulated wind-generated inertial oscillations, *Deep Sea Research and Oceanographic Abstracts*, *17*(4), 813 – 816, IN5, 817–821, doi: 10.1016/0011-7471(70)90043-4.

Pollard, R. T., P. B. Rhines, and R. O. R. Y. Thompson (1972), The deepening of the wind-mixed layer, *Geophysical Fluid Dynamics*, *4*(1), 381–404, doi: 10.1080/03091927208236105.

Price, J., R. Weller, and R. Pinkel (1986), Diurnal cycling - observations and models of the upper ocean response to diurnal heating, cooling, and wind

mixing, *Journal of Geophysical Research - Oceans*, *91*(C7), 8411–8427, doi: 10.1029/JC091iC07p08411.

Rath, W., R. J. Greatbatch, and X. Zhai (2013a), Reduction of Near-Inertial Energy Through the Dependence of Wind Stress on the Ocean-Surface Velocity, *Journal of Geophysical Research - Oceans*, *118*(6), 2761–2773, doi: 10.1002/jgrc.20198.

Rath, W., R. J. Greatbatch, and X. Zhai (2013b), On the Spatial and Temporal Distribution of Near-Inertial Energy in the Southern Ocean, *Journal of Geophysical Research - Oceans*, under review.

Sallee, J. B., K. G. Speer, and S. R. Rintoul (2010), Zonally asymmetric response of the Southern Ocean mixed-layer depth to the Southern Annular Mode, *Nature Geoscience*, *3*(4), 273–279, doi: 10.1038/NGEO812.

Scott, R. B., and Y. Xu (2009), An update on the wind power input to the surface geostrophic flow of the World Ocean, *Deep-Sea Research Part I - Oceanographic Research Papers*, *56*(3), 295–304, doi: 10.1016/j.dsr.2008.09.010.

Straub, D. (1993), On The Transport and Angular-Momentum Balance of Channel Models of the Antarctic Circumpolar Current, *Journal of Physical Oceanography*, *23*(4), 776–782.

Swart, N. C., and J. C. Fyfe (2012), Observed and simulated changes in the Southern Hemisphere surface westerly wind-stress, *Geophysical Research Letters*, *39*, doi: 10.1029/2012GL052810.

Thompson, D., and J. Wallace (2000), Annular modes in the extratropical circulation. Part I: Month-to-month variability, *Journal of Climate*, *13*(5), 1000–1016.

Treguier, A. M., J. Le Sommer, J. M. Molines, and B. de Cuevas (2010), Response of the Southern Ocean to the Southern Annular Mode: Interannual Variability and Multidecadal Trend, *Journal of Physical Oceanography*, *40*(7), 1659–1668, doi: 10.1175/2010JPO4364.1.

Uppala, S., P. Kallberg, A. Simmons, U. Andrae, V. Bechtold, M. Fiorino, J. Gibson, J. Haseler, A. Hernandez, G. Kelly, X. Li, K. Onogi, S. Saarinen, N. Sokka, R. Allan, E. Andersson, K. Arpe, M. Balmaseda, A. Beljaars, L. Van De Berg, J. Bidlot, N. Bormann, S. Caires, F. Chevallier, A. Dethof, M. Dragosavac, M. Fisher, M. Fuentes, S. Hagemann, E. Holm, B. Hoskins, L. Isaksen, P. Janssen, R. Jenne, A. McNally, J. Mahfouf, J. Morcrette, N. Rayner, R. Saunders, P. Simon, A. Sterl, K. Trenberth, A. Untch, D. Vasiljevic, P. Viterbo, and J. Woollen (2005), The ERA-40 re-analysis, *Quarterly Journal of the Royal Meteorological Society*, *131*(612, Part B), 2961–3012, doi: 10.1256/qj.04.176.

van Meurs, P. (1998), Interactions between near-inertial mixed layer currents and the mesoscale: The importance of spatial variabilities in the vorticity field, *Journal of Physical Oceanography*, *28*(7), 1363–1388, doi: 10.1175/1520-0485(1998)028⟨1363:IBNIML⟩2.0.CO;2.

Visbeck, M. (2009), A Station-Based Southern Annular Mode Index from 1884 to 2005, *Journal of Climate*, *22*(4), 940–950, doi: 10.1175/2008JCLI2260.1.

Watanabe, M., and T. Hibiya (2002), Global estimates of the wind-induced energy flux to inertial motions in the surface mixed layer, *Geophysical Research Letters*, *29*(8), doi: 10.1029/2001GL014422.

Xu, Y., and R. B. Scott (2008), Subtleties in forcing eddy resolving ocean models with satellite wind data, *Oecan Modelling*, *20*(3), 240–251, doi: 10.1016/j.ocemod.2007.09.003.

Zhai, X., and R. J. Greatbatch (2007), Wind work in a model of the northwest Atlantic Ocean, *Geophys. Res. Lett.*, *34*, doi: 10.1029/2006GL028907.

Zhai, X., R. J. Greatbatch, C. Eden, and T. Hibiya (2009), On the loss of wind-induced near-inertial energy to turbulent mixing in the upper ocean, *Journal of Physical Oceanography*, *39*, 3040–3045, doi: 10.1175/2009JPO4259.1.

Zhai, X., R. Greatbatch, and J. Zhao (2005), Enhanced vertical propagation of storm-induced near-inertial energy in an eddying ocean channel model, *Geophysical Research Letters*, *32*(18), doi: 10.1029/2005GL023643.

Zhai, X., R. J. Greatbatch, and C. Eden (2007), Spreading of near-inertial energy in a 1/12 degrees model of the North Atlantic Ocean, *Geophysical Research Letters*, *34*(10), doi: 10.1029/2007GL029895.

Zika, J. D., J. LeSommer, C. O. Dufour, A. Naveira-Garbato, and A. Blaker (2013), Acceleration of the Antarctic Circumpolar Current by Wind Stress Along the Coast of Antarctica, *Journal of Physical Oceanography*, doi: 10.1175/JPO-D-13-091.1, in press.

List of Acronyms

ACC Antarctic Circumpolar Current

DPT Drake-Passage Transport

EKE Eddy Kinetic Energy

IWSV Inertial Wind-Stress Variance

NIE Near-Inertial Energy

PM70 The slab-ocean model of *Pollard and Millard* (1970)

PWP The mixed-layer model described by *Plueddemann and Farrar* (2006) similar to the one described by *Price et al.* (1986)

SAM Southern Annular Mode

SLP Sea-Level Pressure

SST Sea-Surface Temperature

SVD Surface-Velocity Dependence (of the wind stress)

NIO Near-Inertial Oscillation

NIW Near-Inertial Wave

WPI Wind Power Input

Author Contributions

Willi Rath designed and performed all model experiments, did all the analysis, produced all the figures and wrote all three manuscripts presented in Chapters 2, 3, and 4.

Richard J. Greatbatch contributed ideas to the design of the experiments, the analysis, and commented on all three manuscripts presented in Chapters 2, 3, and 4.

Xiaoming Zhai contributed ideas to the design of the experiments, the analysis, and commented on the manuscripts presented in Chapters 2 and 4.

Acknowledgements

I want to thank Richard Greatbatch for constantly supporting me, for always having an idea, and for never discouraging me from pursuing my own ideas. I want to thank Peter Brandt for agreeing to read all this.

I want to thank Xiaoming Zhai for a couple of very fruitful discussions.

I want to thank Carsten Eden and Lars Czeschel for getting me started with the model.

I want to thank Jan Harlaß and Klaus Getzlaff for proof-reading parts of this thesis.

I want to thank the whole TM (especially Sabine Niewels and Annegret Schurbohm), and the people from Alte Botanik for making it a pleasure to work in this institute.

Finally, I want to thank [redacted], [redacted] and [redacted] for closing the balance.

Erklärung

Hiermit erkläre ich, dass ich die vorliegende Dissertation, abgesehen von der Beratung durch meinen Betreuer, selbstständig verfasst und keine anderen als die angegebenen Hilfsmittel verwendet habe. Beiträge anderer Wissenschaftler habe ich kenntlich gemacht. Ich erkläre, dass diese Arbeit noch nicht zur Erlangung eines Doktorgrades an anderer Stelle vorgelegen hat. Ich erkläre, dass die vorliegende Arbeit gemäß der Grundsätze zur Sicherung guter wissenschaftlicher Praxis der Deutschen Forschungsgemeinschaft erstellt wurde.

Kiel, Oktober 2013 (Willi Rath)